IEKP-KA/2004-20

Measurement of the hadronic cross section $\sigma(e^+e^- \to \pi^+\pi^-)$ with the KLOE detector using Radiative Return with tagged photons

Zur Erlangung des akademischen Grades eines
DOKTORS DER NATURWISSENSCHAFTEN
der Fakultät für Physik der Universität
Karlsruhe (TH) genehmigte

DISSERTATION

von

Dott.ssa Debora Leone (Laurea)
aus Rom (Italien)

Tag der mündlichen Prüfung: 11.05.2007
Referent: Prof. Dr. Wolfgang Kluge, Institut für Experimentelle Kernphysik
Korreferent: Prof. Dr. Thomas Müller, Institut für Experimentelle Kernphysik

Zusammenfassung

Das anomale magnetische Moment des Myons a_μ (definiert als $a_\mu = (g_\mu - 2)/2$) ist eine der am besten gemessenen Größen der Teilchenphysik. Es liefert somit einen sehr präzisen Test des Standardmodells. Eine Diskrepanz zwischen der theoretischen Vorhersage und der direkten Messung könnte einen Hinweis auf mögliche Beiträge neuer Physik geben. Die aktuellste Messung für a_μ wurde vom Brookhaven-Experiment durchgeführt, bei der eine extreme Präzision von 0.7 Millionstel erreicht wurde. Theoretische Berechnungen von mehreren Autoren erreichen eine ähnliche Präzision, die zentralen Werte weichen jedoch um bis zu drei Standardabweichungen vom experimentellen Wert ab. Die theoretischen Vorhersagen sind durch den hadronischen Beitrag zu a_μ limitiert, welcher nicht durch Störungs-QCD berechnet werden kann. Der hadronische Beitrag zum anomalen magnetischen Moment, a_μ^{hadr}, kann über ein Dispersionsintegral mit dem hadronischen Wirkungsquerschnitt verknüpft werden:

$$a_\mu^{\mathrm{hadr}} = \frac{1}{4\pi^3} \int_{4m_\pi^2}^{\infty} \sigma_{e^+e^- \to hadr}(s) K(s)\, ds \tag{1}$$

wobei das Integral über die quadrierte invariante Masse s des hadronischen Systems ausgeführt wird; der Kernel $K(s)$ ist eine monotone Funktion, die sich wie $1/s$ verhält. Niederenergetische hadronische Wirkungsquerschnitte sind deshalb in a_μ^{hadr} stark gewichtet, und speziell der Kanal $e^+e^- \to \pi^+\pi^-$ ist für ungefähr 70% des vollen Integrals für a_μ^{hadr} verantwortlich. Ein alternativer Ansatz mit Spektralfunktionen von hadronischen τ-Zerfällen (auf Isospin-verletzende Effekte hin korrigiert), die mit Hilfe des Theorems vom Erhaltenen Vektorstrom (CVC) mit $\sigma(e^+e^- \to \text{hadrons})$ verknüpft werde können, verringert die Diskrepanz mit der direkten Messung von a_μ. Der Grund für diese Inkonsistenz beim Vergleich von auf e^+e^- und τ-Daten basierender Vorhersagen ist unverstanden. Um die Natur dieser Differenz zu klären werden präzisere experimentelle Messungen des hadronischen Wirkungsquerschnitts benötigt, speziell bei niedrigen Energien.

KLOE hat in der Vergangenheit die Methode des *radiative return* erfolgreich zur Messung des hadronischen Wirkungsquerschnitts $\sigma(e^+e^- \to \pi^+\pi^-)$ in einer Analyse von $\sim 140 pb^{-1}$ von im Jahre 2001 genommenen Daten angewendet. Vom Elektron oder Positron abgestrahlte Photonen im Anfangszustand (Initial State Radiation, ISR) verringern die nominelle Energie des Speicherrings (1.02 GeV beim KLOE Experiment), und ermöglichen

dadurch einen *radiative return* zum ϱ- oder ω-Meson. Mit einem einzigen Datensatz ist es so möglich, den hadronischen Wirkungsquerschnitt als Funktion der Energie des zwei-Pion-Systems von der zwei-Pion-Schwelle bis zur Speicherringsenergie zu untersuchen. Der radiative Wirkungsquerschnitt und der $\pi^+\pi^-$-Wirkungsquerschnitt können über die Abstrahlfunktion H verknüpft werden:

$$s_\pi \frac{d\sigma(e^+e^- \to \pi^+\pi^-\gamma)}{ds_\pi} = H(s_\pi) \cdot \sigma(e^+e^- \to \pi^+\pi^-) \tag{2}$$

wobei s_π für die quadrierte invariante Masse der Pionen im Endzustand steht.
Beiträge von Photonen, die von einem der beiden Pionen im Endzustand abgestrahlt werden (Final State Radiation, FSR), stellen einen Untergrund dar und sind vom Signalprozess nicht unterscheidbar. Betrachtet man Photonen unter kleinen Polarwinkeln (*small angle analysis, Kleinwinkelanalyse*) um die Endzustandsstrahlung zu verringern, so ist die Messung auf den Bereich der quadrierten Energie von $0.35 < M^2_{\pi\pi} < 0.95$ GeV^2 beschränkt, da der Bereich unterhalb 0.35 GeV^2 aus kinematischen Gründen bei diesen Akzeptanzschnitten verboten ist. Das erzielte Resultat bestätigt die beobachtete Diskrepanz zwischen e^+e^-- und τ-Spektralfunktionen.
Dieselbe Methode wurde nun in einer zweiten Analyse angewendet, bei der $240pb^{-1}$ von im Jahr 2002 genommenen Daten untersucht wurden, unter Betrachtung einer komplementären Akzeptanzregion, in der das ISR-Photon unter großen Polarwinkeln nachgewiesen wird. Diese neue Analyse soll in der vorliegenden Dissertation dargestellt werden. Die drei Hauptquellen von *reduziblem* Untergrund ($e^+e^-\gamma$, $\mu^+\mu^-\gamma$ und $\pi^+\pi^-\pi^0$ Ereignisse) werden mit Hilfe von kinematischen Variablen ausgesondert und die verbleibende Kontamination aufgrund der MonteCarlo-Voraussage abgezogen. Vergleiche zwischen Daten und MonteCarlo in mehreren Variablen untermauern die Richtigkeit des Untergrundabzugs: Im Bereich $0.5 - 0.8$ GeV^2 ist der damit verbundene systematische Fehler $< 0.3\%$.
Die Effizienzen der Analyseschnitte wurden in den meisten Fällen mit Hilfe von Kontrolldatensätzen gemessen, wo dies nicht der Fall ist, wurden sie mit MonteCarlo ermittelt. Aufgrund der immer höheren Präzision dieser Art von Messungen wurde spezielle Sorgfalt in der Ermittlung des systematischen Fehlers für jede Effizienz angewendet. Die zur Untergrundsunterdrückung verwendeten Analyseschnitte wurden so gewählt, dass der systematische Fehler minimal blieb. Unter Vernachässigung des Fehlers für den Abzug des *irreduziblem* Untergrunds wird der komplette systematische Fehler am ϱ-Peak zu 0.6% abgeschätzt, sehr viel geringer als in der *Kleinwinkelanalyse*.
Der *irreduzible* Untergrund besteht aus drei Quellen: Die Ereignisse mit Endzustandsstrahlung in erster Ordnung, deren Beitrag mit Hilfe des MonteCarlo-Generators PHOKHARA im Modell der skalaren QED abgeschätzt wird; der resonante Zerfall $\phi \to \varrho^\pm\pi^\mp \to \pi^+\pi^-\gamma$, dessen Wirkungsquerschnitt zwar schlecht bekannt ist, der aber oberhalb von 0.5 GeV^2 vernachlässigbar ist; und schließlich der Beitrag von Skalarmesonen im Strahlungszerfall des ϕ in $f_0(980) + \gamma$. Der

Hauptbeitrag zum Fehler der Messung des Pion-Formfaktors kommt derzeit vom Beitrag der Skalarmesonen. Die Natur dieser Teilchen ist immer noch umstritten, und es existieren mehrere Modelle zur Beschreibung ihrer Dynamik. Die Vorhersagen dieser Modelle wurden mit Hilfe der *forward-backward* Asymmetrie mit den Daten verglichen. Diese Variable entsteht durch die Interferenz zwischen der Anfangszustandsabstrahlung, wobei sich die Pionen in einem ungeraden Zustand bezüglich der Ladungskonjugation befinden, und der Endzustandsabstrahlung und dem Strahlungszerfall des ϕ, bei denen sich die Pionen in einem geraden Zustand bezüglich der Ladungskonjugation befinden. Diese Interferenz ist für die Verzerrung der Polarwinkelverteilungen von π^+ und π^- verantwortlich. Da in der Großwinkelanalyse eine große Anzahle an Ereignissen mit Endzustandsabstrahlung vorhanden ist, und da die *forward-backward* Asymmetrie sehr sensitiv auf die Präsenz von Skalarmesonen ist, wurde diese Variable in der vorliegenden Arbeit benutzt, um diese Teilchen zu untersuchen. Aus dem Vergleich der Daten mit der MonteCarlo-Vorhersage verschiedener Modelle konnte ein Modell ausgewählt werden, welches am besten zu den Daten passt. Mit Hilfe weiterer Vergleiche zwischen dem ausgewählten Modell und den Daten konnten die im Modell auftretenden Parameter des $f_0(980)$ angepasst werden. Diese Methode erlaubt nicht nur, den Beitrag skalarer Mesonen von den Daten abzuziehen, sie ist auch sehr vielversprechend wenn es darum geht, weitere Informationen über diese Teilchen zu erhalten. Ein neuer MonteCarlo-Generator (EVA), welcher sowohl den Beitrag von Skalarmesonen als auch des direkten Zerfalls $\phi \to \varrho^{\pm}\pi^{\mp}$ enthält, wurde vor kurzer Zeit veröffentlicht. Die Paramter der Skalarmesonen wurden in EVA noch nicht angepasst. Momentan wird der Vergleich zwischen den Vorhersagen von PHOKHARA und EVA benützt, um eine Abschätzung für den systematischen Fehler auf die durch die Skalarmesonen erzeugte Korrektur zu erhalten. Dies ist der dominierende systematische Fehler auf die Messung des Pion-Formfaktors zwischen 0.5 und 0.85 GeV^2. Der in der Großwinkelanalyse erhaltene Pion-Formfaktor wurde mit den publizierten Werten aus der Kleinwinkelanalyse verglichen. Beide sind innerhalb der systematischen Fehler in Übereinstimmung.

In naher Zukunft wird der systematische Fehler für die Skalarmesonen durch die Anpassungsprozedur mit dem neuen EVA-Generator stark verringert werden. Diese Methode wird eine sehr viel bessere Abschätzung des von den Skalarmesonen erzeugten Untergrunds zur Folge haben. Das Ausmaßdes Einflusses der Skalarmesonen bei niedrigen Massen wurde erst während der Durchführung der Analyse deutlich. Bei der erzielten Präzision der Großwinkelanalyse ist der große systematische Fehler auf den Skalarmesonbeitrag nicht akzeptabel. Mit dem Zweck, Daten ohne einen Beitrag von Skalarmesonen zu erhalten, wurden am KLOE-Experiment im Jahr 2006 $\sim$ 225 pb^{-1} bei $\sqrt{s}$ = 1000 MeV genommen, also 20 MeV unterhalb der Masse des ϕ-Mesons. Der Beitrag der skalaren Mesonen ist außerhalb der ϕ-Resonanz stark unterdrückt, und damit wird dieser *irreduzible* Untergrund nahezu zu Null. Auch der Beitrag von $\pi^+\pi^-\pi^0$ Ereignissen is stark vermindert, was ein Überprüfen der Behandlung dieses

Untergrunds in der Großwinkelanalyse erlaubt. Auf diese Art und Weise ist es zum ersten Mal möglich, die Gültigkeit des Models der skalaren QED für die Amplitude der Endzustandsabstrahlung über einen großen Energiebereich zu überprüfen. Dieser Test wird auf die *forward-backward* Asymmetrie zurückgreifen. Derzeit wird der Test noch untersucht. Er wurde in der vorliegenden Analyse zur Abschätzung des systematischen Fehlers der Endzustandsabstrahlung verwendet.

Summary

The anomalous magnetic moment a_μ, defined as $(g_\mu - 2)/2$, is one of the most precisely measured quantities in particle physics, providing an extremely precise test of the Standard Model. A possible discrepancy between the theoretical predictions and the direct measurement could give a hint for possible new physics contribution. The most recent measurement of a_μ was performed by the Brookhaven experiment in 2004, where an extreme precision of 0.7 part per million has been reached. Theoretical evaluations from several authors have a similar precision but their central values deviate up to three standard deviations with respect to the experimental value. The theoretical predictions are limited by the hadronic contribution to a_μ which cannot be computed by perturbative QCD. The hadronic contribution to the anomalous magnetic moment, a_μ^{hadr}, can be related to the hadronic cross section via a dispersion integral:

$$a_\mu^{hadr} = \frac{1}{4\pi^3} \int_{4m_\pi^2}^{\infty} \sigma_{e^+e^- \to hadr}(s) K(s) ds$$

where the integral is carried out over the invariant mass squared of the hadronic system s; the kernel $K(s)$ is a monotonous function behaving like $1/s$. Low energy hadronic cross sections are therefore strongly enhanced in a_μ^{hadr} and in particular the channel $e^+e^- \to \pi^+\pi^-$ is responsible for about 70% of the total integral to a_μ^{hadr}. If the alternative approach of using the spectral function of hadronic τ-decays (corrected for isospin violation effects) is performed, which can be related to $\sigma(e^+e^- \to \text{hadrons})$ via the conserved vector current theorem, the discrepancy with the direct measurement becomes smaller. The reason for the inconsistency in the comparison of predictions based on e^+e^-- and τ-data is not understood. In order to clarify the nature of this difference more precise experimental measurements of the hadronic cross section are needed, especially at low energies.
KLOE has in the past successfully used the *radiative return* method to measure the hadronic cross section $\sigma(e^+e^- \to \pi^+\pi^-)$ in an analysis of $\sim$140 pb^{-1} of data collected in 2001. Initial State Radiation (ISR) photons emitted by the electron or by the positron lower the nominal energy of the collider (1.02 GeV at the KLOE experiment), allowing a *radiative return* to the ρ and to the ω mesons. With one single data set it is possible to investigate the hadronic cross section from the 2π theshold to the energy of the collider as a function of the two-pions system energy. The radiative cross section and the $\pi^+\pi^-$ cross section can be related

through the radiator function H:

$$s_\pi \frac{d\sigma(e^+e^- \to \pi^+\pi^-\gamma)}{ds_\pi} = H(s_\pi) \cdot \sigma(e^+e^- \to \pi^+\pi^-)$$

being s_π the squared invariant mass of the pions in the final state.
Contributions from photons radiated by one of the two pions in the final state (Final State Radiaton) are a background for the measurement and cannot be distinguished from the signal. Looking at small photon polar angles (*small angle analysis*), in order to reduce the Final State Radiation contribution, the measurement is limited to the energy squared range $0.35 < M^2_{\pi\pi} < 0.95$ GeV^2, being the threshold kinematically forbidden in this acceptance configuration. The obtained result confirms the observed discrepancy between e^+e^-- and τ-spectral functions.
The same method has now been applied to a second analysis, where 240 pb^{-1} of data collected in 2002 have been analysed, looking at the complementary acceptance region (*large angle analysis*), in which the ISR photon is tagged at large polar angles. This new analysis is the subject of the present thesis. The three main sources of *reducible* background ($e^+e^-\gamma$, $\mu^+\mu^-\gamma$ and $\pi^+\pi^-\pi^0$ events) are rejected by means of kinematical variables and the residual contamination is subtracted according to the MonteCarlo prediction. Comparisons data-MonteCarlo on several variables assure that the background subtraction is correct: in the range $0.5 \div 0.85$ GeV^2 the associated systematic error is $<0.3\%$.
The efficiencies due to the analysis cuts have been measured from data control sample in most cases, otherwise they are taken from MonteCarlo. Since the incresing precision in this kind of measurements, particular care has been taken in the evaluation of the systematic error associated to each efficiency. The analysis cuts dedicated to the background suppression have been tuned in order to keep as low as possible the systematic errors. Neglecting the error of the subtraction of the *irreducible* background, the total systematic error on the ρ-peak is estimated to be 0.6%, considerably smaller than in the *small angle analysis*.
The *irreducible* background consists of three sources: the Final State Radiaton-Leading Order events, whose contribution is taken into account by the MonteCarlo generator PHOKHARA using the scalar QED model, the resonant decay $\phi \to \rho^\pm\pi^\mp \to \pi^+\pi^-\gamma$ for which the cross section is poorly known, but which is negligible above 0.5 GeV^2, and finally the scalar meson contribution from the ϕ radiative decay into $f_0(980)$. The dominant error of the pion form factor measurement at present comes from the scalar meson contribution. The nature of these particles is still controversial and several models describing their dynamics are available. The predictions of these models have been compared with the data by means of the forward-backward asymmetry. This variable arises from the interference between the Initial State Radiaton, with $\pi^+\pi^-$ in on odd charge conjugate state, and the Final State Radiaton and radiative ϕ decay with $\pi^+\pi^-$, in an even charge conjugate state, and it is responsible of a distortion of the polar angular distribution of the π^+ and the π^-.

Given the abundance of Final State Radiation contribution in the *large angle* region and the sensitivity of the forward-backward asymmetry to the presence of the scalar mesons, this variable has been widely used in this work to study these particles. Comparing the data with the MonteCarlo prediction using different models for the scalar mesons, we have been able to choose one model that fits better our data. By further comparisons between the chosen model and the data, we have tuned the parameters of the $f_0(980)$ entering the model. This procedure does not allow only to subtract the scalar mesons contribution from the data sample; it is actually a promising method to extract further information on these particles. A new MonteCarlo generator (EVA) taking into account both the scalar meson contribution and the direct decay $\phi \to \rho^{\pm}\pi^{\mp}$ has been recently released. The parameters of the scalar mesons have not been tuned yet in EVA. At the moment we use the comparison between the PHOKHARA and EVA predictions to have an estimate of the systematic error on the scalar mesons correction. This systematic error is the dominant one in the pion form factor that we have extracted between 0.5 and 0.85 GeV^2. The pion form factor measured with the *large angle analysis* has been compared with the published one (*small angle analysis*), and considering the systematic errors of the two, we conclude that they are in agreement.

In the near future, the systematic error on the scalar mesons will be reduced by repeating the tuning procedure on the new EVA generator. This method will allow a much improved determination of the background from scalar mesons.

During the developlent of this work, the issue of the scalar meson contribution at low masses has become clear. Given the high precision achieved in the measurement at *large angle*, the big systematic error coming from the scalar meson contribution is not acceptable. With the purpose to have a sample free from the scalar meson contribution, KLOE has collected in 2006 $\sim$225 pb^{-1} at $\sqrt{s}$=1000 MeV, i.e. 20 MeV lower than the ϕ mass. The scalar mesons contribution is strongly suppressed in the off-peak data, reducing this *irridducible* background almost to zero. Also the contamination from $\pi^+\pi^-\pi^0$ events is drastically reduced, allowing to cross check the treatment of this background in the *large angle analysis*. Like this it will be possible to perform for the first time dedicated tests on the validity of the scalar QED model for the description of the Final State Radiation amplitude over a wide range energy. For this test the forward-backward asymmetry will be used. This test is under study at the moment and has been already used in the present analysis for the estimate of the systematic error of the final state radiation subtraction.

Contents

Introduction

Developed in the years between 1970 and 1973, the Standard Model has been up to now a very successful model in the description of the elementary particles and of their interactions. Apart from the Higgs Boson, all the particles predicted have been experimentally discovered and all the precision tests on the Standard Model have confirmed the theoretical predictions. An extremely precise test involves the anomalous magnetic moment of the muon a_μ. By comparing the experimental value with the theoretical prediction including all the relevant radiative corrections, a possible discrepancy could give a hint of new physics. The interaction of the muon with particles beyond the Standard Model is characterized by the coupling factor $(m_\mu/\Lambda)^2$, where Λ is the energy scale of the process. Even if the contribution from new physics to a_μ might be very small, the high precision of the Standard Model prediction as well as the one of the direct measurement might eventually allow to resolve a contribution from new physics.
The most precise measurement of a_μ comes from the E821 experiment performed in Brookhaven, resulting in the present world average value of

$$a_\mu = (11659203 \pm 8) \times 10^{-10} \tag{3}$$

Theoretical evaluations by several authors are affected by similar uncertainties, but their central values deviate up to three standard deviations with respect to the experimental one. The precision of the mentioned theoretical evaluations within the Standard Model is dominated by the limited knowledge of the hadronic contribution of the muon anomaly. It can be related to the hadronic cross section via the dispersion relation

$$a_\mu^{hadr} = \frac{1}{4\pi^3} \int_{4m_\pi^2}^{\infty} \sigma_{e^+e^- \to hadr}(s) K(s) ds \tag{4}$$

where the integral is carried out over the invariant mass squared of the hadronic system and the kernel $K(s)$ is a monotonous function behaving like $1/s$. Low energy cross sections contribute therefore strongly to a_μ^{hadr}. Since perturbative QCD cannot be used below $\sim$2 GeV, one has to use experimentally measured cross sections in the dispersion integral for low energies. Below 1 GeV the channel $e^+e^- \to \pi^+\pi^-$ is responsible for about 70% of the total a_μ^{hadr}. An alternative input to the dispersion integral is the spectral function of

hadronic τ decay data, corrected for isospin violating effects. A considerable discrepancy appears when comparing e^+e^-- and τ-data. If the latter are used in the evaluation of a_μ^{hadr}, the theoretical value of a_μ shows a small deviation ($\sim 0.7\ \sigma$) from the experimental measurement.

In order to clarify the nature of this difference in the theoretical evaluations, and to claim an eventual hint of new physics, more precise experimental data on hadronic cross sections, especially at low energies, are needed. The KLOE experiment in a recent publication, has for the first time used the *radiative return* method to measure the hadronic cross section $\sigma(e^+e^- \to \pi^+\pi^-)$ at the ϕ-factory DAΦNE. The *Initial State Radiation* (ISR) lowers the center-of-mass energy of the collider ($\sqrt{s}$=1.02 GeV) and allows to investigate the hadronic cross section from the $2m_\pi$ threshold up to the collision energy of the machine. The full energy range below 1 GeV is thus available in one single experiment, without performing an energy scan.

In the above mentioned already published analysis, KLOE has performed a measurement of the pion form factor looking for $\pi^+\pi^-\gamma$ events with the ISR photon emitted at small polar angles. A new and complementary measurement is presented here, in which the photon is detected at large polar angles. This measurement has different experimental issues, first of all concerning the background contamination. It allows to explore the threshold region (down to $2m_\pi$) which is kinematically forbidden in the small photon polar angle configuration. The big amount of final state radiation, if from one side represents an issue of the analysis, from the other allows to make tests of scalar QED, by comparing the distribution of variables in data and in MonteCarlo which enhance eventual discrepancies from the model. The measurement of the threshold results limited by the presence of the scalar mesons, whose existence is well established, but whose properties are still poorly known. Nevertheless the measurement of the pion form factor around the ρ-peak is an important check of the previous KLOE result.

In chapter 1 the theoretical background and the present status of a_μ is given, and after the description of the KLOE detector in chapter 2, a brief remind of the small photon angle analysis together with the motivation for the present work is given in chapter 3. Chapter 4 is dedicated to the description of the signal selection, to the background subtraction to arrive at the mass spectrum which will be used as input for obtaining the pion form factor in chapter 6. The efficiency for each single step of the analysis and the evaluation of the systematic error for the several cuts are outlined in chapter 5. Finally chapter 7 provides an outlook to possible and necessary improvements of the measurement.

Chapter 1

The hadronic cross section and the Standard Model

Given the increasing precision of the modern particle physics experiments, a precise knowledge of the theory and of the input parameters is more and more necessary. The anomalous magnetic moment of the muon $a_\mu = (g_\mu - 2)/2$, as the running of the electromagnetic coupling constant $\alpha_{em}(s)$, is very sensitive to radiative corrections, and the precise determination of these latter is limited by the uncertainty of the photon vacuum polarization from the five lightest quarks relevant for α_{EM}. At low energies perturbative QCD fails in calculating such corrections; however an alternative approach has been worked out, which puts in relation the photon vacuum polarization with the cross sections $e^+e^- \to \gamma^* \to q\bar{q} \to$ hadrons (optical theorem). For this reason precise measurements of hadronic cross sections are extremely useful to improve the standard model prediction on both a_μ and $\alpha_{em}(s)$.

1.1 The dispersion integral

The precision of the theoretical prediction for cross sections from e^+e^- annihilation to lepton pairs is limited by first order loop effects from hadronic vacuum polarization. Fig 1.1(a) shows how the presence of hadronic vacuum polarization in the photon propagator affects the cross setion for a process like $e^+e^- \to \mu^+\mu^-$. The effect depends on the energy squared of the virtual photon connecting the initial with the final state. Together with the corresponding graph from leptonic vacuum polarization, this can be expressed by an energy-dependent coupling costant $\alpha_{em}(s)$ (§ 1.4). In a similar way, the hadronic vacuum polarization modifies the interaction of a muon with an external $\vec{B}$-field, as can be seen in fig. 1.1(b). All the charged particles-antiparticles $e^+e^-, \mu^+\mu^-, \tau^+\tau^-, u\bar{u}, d\bar{d}$,.., contribute to the process, but the basic interest here is in the quark loops, the lepton ones being calculable in QED. The low energy contributions of light quarks to the vacuum polarization cannot be

reliably predicted by perturbative QCD. However, unitarity and analyticity allow to relate it to the hadronic cross section $e^+e^- \rightarrow$ hadrons.

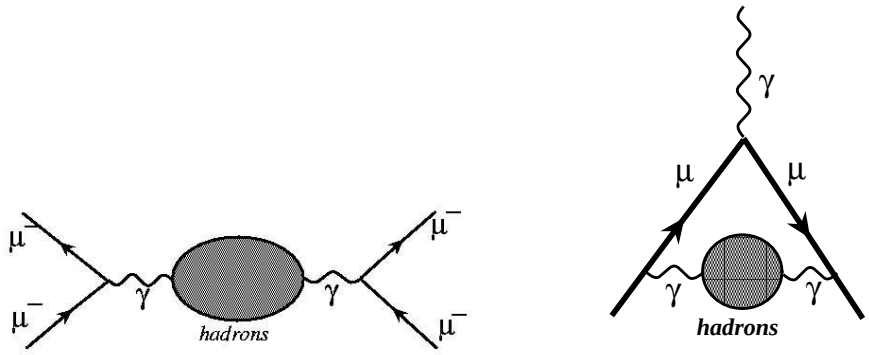

(a) (b)

Figure 1.1: (a) Hadronic vacuum polarization modifying the electromagnetic coupling constant a_{em} in the process $e^+e^- \rightarrow \mu^+\mu-$ (a) and in the anomalous magnetic moment of the muon a_μ (b).

The inclusion of the vacuum polarization into the photon propagator results in a modified photon propagator:

$$\frac{-ig_{\mu\nu}}{q^2} \rightarrow \frac{-ig_{\mu\nu}}{q^2}\frac{1}{1+e^2\Pi_\gamma(q^2)} \tag{1.1}$$

where the $\Pi_\gamma(q^2)$ is the photon vacuum polarization amplitude containing the leptonic as well as the hadronic part. Let us concentrate only on the hadronic part. The unitarity of

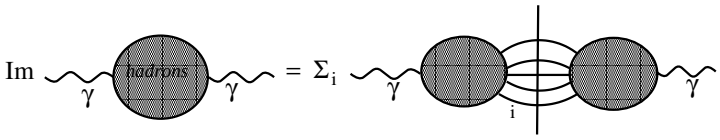

Figure 1.2: The optical theorem relating the hadronic vacuum polarization to the cross section $\gamma^* \rightarrow$ hadrons. The vertical line represents the hadronic intermediate state.

the scattering matrix leads to the optical theorem, according to which the imaginary part of the photon vacuum polarization amplitude can be written as the sum over all possible final states generated from the photon, as outlined in fig. 1.2. The photon vacuum polarization amplitude $\Pi_\gamma(q^2)$ reads:

$$\Im(\Pi_\gamma(q^2)) = \frac{q^2}{e^2}\sigma(e^+e^- \rightarrow \gamma^* \rightarrow \text{hadrons}) \tag{1.2}$$

where γ^* is the virtual photon connecting the initial and the final state.
In terms of the cross section ratio $R(s) = \frac{\sigma(e^+e^-\to\gamma^*\to\text{hadrons})}{\sigma(e^+e^-\to\mu^+\mu^-)}$, it can be expressed as

$$\Im(\Pi_\gamma(q^2)) = \frac{1}{12\pi}R(s) \tag{1.3}$$

taking into account that $\sigma(e^+e^-\to\mu^+\mu^-) = 4\pi\alpha^2/3s^2$.
The analyticity of the photon propagator implies the dispersion relation:

$$\Im(\Pi_\gamma(q^2)) - \Im(\Pi_\gamma(0)) = \frac{q^2}{\pi}\int_0^\infty ds\frac{\Im\Pi_\gamma(s)}{s(s-q^2-i\epsilon)} \tag{1.4}$$

Eqs.1.3 and 1.4 are the basis for any non-perturbative calculation of hadronic vacuum polarization in terms of the measured quantity $\sigma(e^+e^-\to\text{hadrons})$.

1.2 Measurement of the R ratio

As pointed out in the previous section, the ratio R is the experimental input which enters in the evaluation of a_μ. In fig. 1.3(a) a set of values of R in the energy range between the threshold $2m_\pi$ and 10 GeV from different experiments is presented. Low energy hadronic cross sections have been measured up to recently by experiments running at e^+e^- colliders (OLYA [1], TOF [2], ND [3], CMD [4], CMD-2 [5][6], SND [7][8], DM1 [9], DM2 [10], KLOE [11]). At low masses, where the reaction $e^+e^-\to\pi^+\pi^-$ is dominant, presently three precision sets of data are available: two of them from CMD-2 and SND, both running at the VEPP-2M collider in Novosibirsk and claiming a systematic error respectively of 0.6 % ([5],[6]) and of 1.3% for $\sqrt(s)$ >420 MeV and 3.2% for $\sqrt(s)$ <420 MeV ([7],[8]), the third one from KLOE, running at the DAΦNE collider at Frascati whose measurement has a systematic error of 1.3% ([11]). In the region close to the threshold ($\sqrt{s}\sim 2m_\pi$) the data from SND are the most recent, with a relatively large error. Clearly this region requires more experimental precision. The CMD-2 experiment has provided also precise measurement of important cross section channels such as $\sigma(e^+e^-\to\pi^+\pi^-\pi^0)$ [13], $\sigma(e^+e^-\to\pi^+\pi^-\pi^0\pi^0)$ [14] and $\sigma(e^+e^-\to\pi^+\pi^-\pi^+\pi^-)$[14]. An upgrade of the experiment is in progress and will be able to provide more accurate results in the energy range 0.4÷2 GeV, thanks to the 10 times bigger statistics it is expected to collect.
An improvement of the knowledge of the hadronic cross section above 1 GeV comes also from the BABAR experiment (running at the B-factory PEP-II at an energy of $\sqrt{s} = 10.6$ GeV). This collaboration has already published results [15] [16] of several analysis with three and four hadrons as final state ($e^+e^-\to\pi^+\pi^-\pi^0, \pi^+\pi^-\pi^+\pi^-, K^+K^-\pi^+\pi^-, K^+K^-K^+K^-$) with the systematic accuracy of of 5% in the mass region 1-2 GeV and lager errors between 2 and 4.5 GeV. They have obtained results [17] also in the six hadrons channels, i.e. $e^+e^-\to 3(\pi^+\pi^-), 2(\pi^+\pi^-\pi^0), 2(\pi^+\pi^-K^+K^-)$, improving largely the existing measurements.
To complement the cross section data from e^+e^--collider experiments, precise measurement

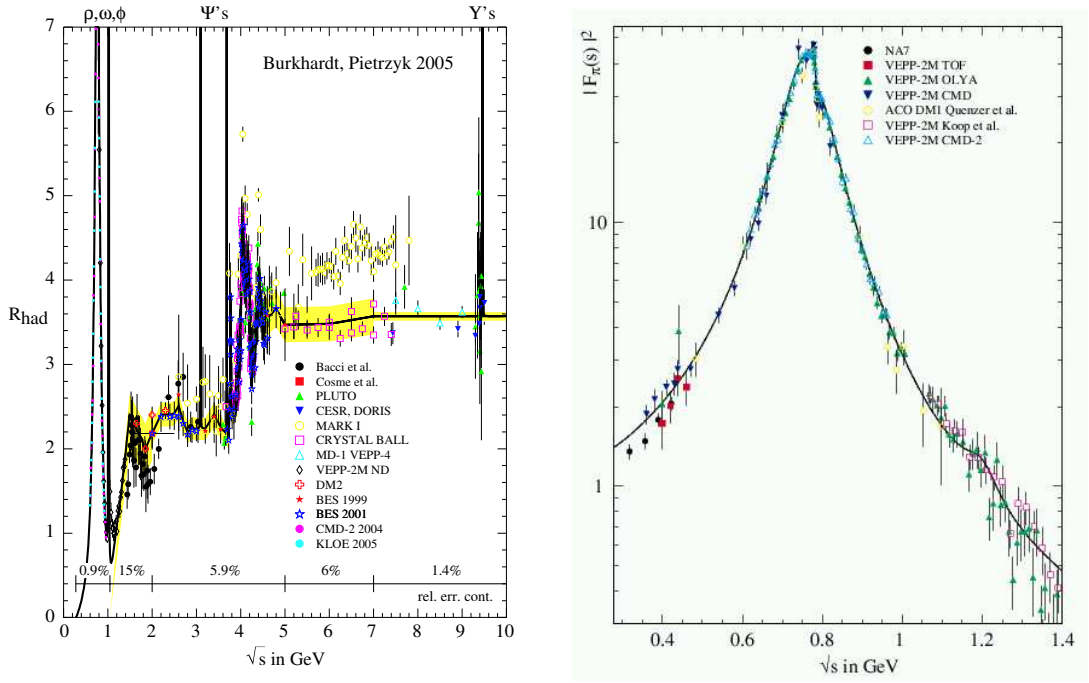

(a) (b)

Figure 1.3: (a) Comparison of R measurements (from [12]). (b) The pion form factor as measured by the experiments NA7, TOF, OLYA, CMD and CMD-2. The last precise measurements of $\sigma(e^+e^- \to \pi^+\pi^-)$ do not contribute to this plot.

of τ lepton decays can be used, as suggested in [18]. Assuming the charged vector current is conserved (CVC), the isovector part of the cross section for e^+e^- into hadrons can be derived from τ-decay spectra by an isospin rotation, as illustrated in fig. 1.4, where the decay $\tau^- \to \nu_\tau \pi^- \pi^0$ is related to the reaction $e^+e^- \to \pi^+\pi^-$, forming the two pions a vector in the isospin space. In τ decay processes the only interaction involved is the weak

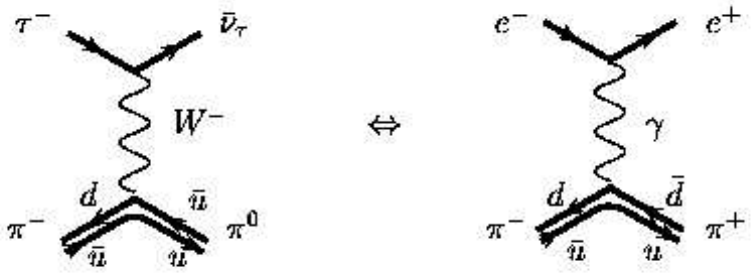

Figure 1.4: The decay $\tau^- \to \pi^-\pi^0\nu_\tau$ (a) can be seen as the isospin rotation of the isovector part of the process $e^+e^- \to \pi^+\pi^-$ (b), provided that CVC holds.

interaction, therefore any effects from vacuum polarization are excluded. What is really related to the $e^+e^- \to \pi^+\pi^-$ cross section is the τ spectral function $v_{\pi^-\pi^0}(s)$ that can be extracted directly from the corresponding invariant mass spectra of the final state (i.e. $\pi^-\pi^0$ in fig. 1.4), through the relation:

$$v_{\pi^-\pi^0}(s) = \frac{m_\tau^2}{6|V_{ud}|^2 S_{EW}} \frac{B(\tau^- \to \nu_\tau \pi^-\pi^0)}{B(\tau^- \to \nu_\tau e^- \bar{\nu_e})} \frac{1}{N_{\pi^-\pi^0}} \frac{dN_{\pi^-\pi^0}}{ds} \left[\left(1 - \frac{s}{m_\tau^2}\right)^2 \left(1 - \frac{2s}{m_\tau^2}\right) \right]^{-1} \tag{1.5}$$

where $|V_{ud}|$ is the CKM weak mixing matrix element and S_{EW} accounts for electroweak radiative corrections. The cross section $\sigma(e^+e^- \to \pi^+\pi^-)$ can be calculated from $v_{\pi^-\pi^0}(s)$ via the relation

$$\sigma^{I=1}_{\pi^+\pi^-} = \frac{4\pi\alpha^2}{s} v_{\pi^-\pi^0} \tag{1.6}$$

These equation holds only in the limit of exact isospin invariance; breaking of isospin due to electromagnetic effects and up-down quark mass splitting have to be taken into account properly. This is done in [19] for the most relevant $\pi\pi$ channel; once the τ spectral function is corrected for the isospin breaking effects, it can be compared directly to the corresponding hadronic cross sections measured in e^+e^- annihilation, as it is done in fig. 1.5 for the $\pi^+\pi^-$ channel. Although the latest CMD-2 data are basically consistent with τ data for the energy region below 850 MeV (0.72 GeV^2 in the plot), there is a clear discrepancy for larger energies. The most recent e^+e^- data from KLOE confirms the discrepancy with the τ data. Among the possible origins of this discrepancy, one may think of inconsistencies in the e^+e^- data, or in the τ data, or in the isospin-breaking correction applied to the τ spectral function. Possible additional isospin breaking effects were recently discussed [20] giving rise

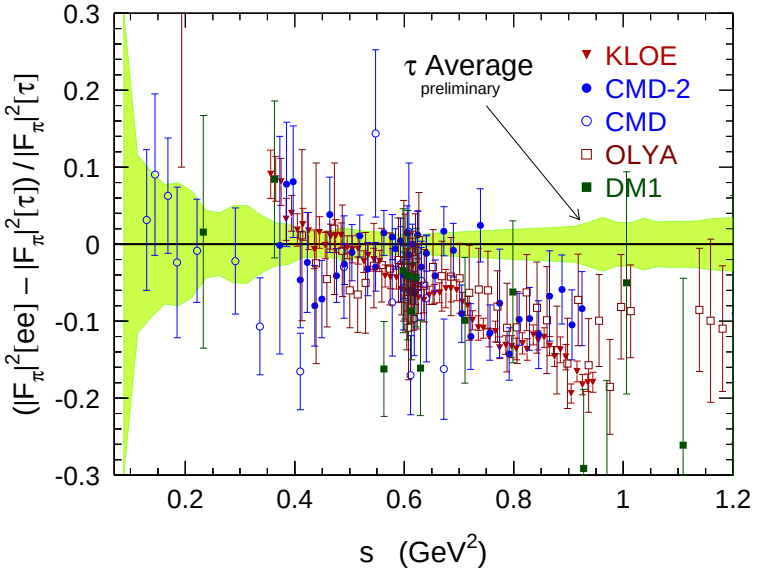

Figure 1.5: Relative comparison of the $\pi^+\pi^-$ spectral function from e^+e^- data and isospin breaking corrected τ data. The band shows the uncertainty in the τ spectral function.

to possible mass and width differences between the neutral and charged ρ-meson.

1.3 The anomalous magnetic moment of the muon

The magnetic moment of a lepton l ($l = e, \mu, \tau$) $\vec{\mu_l}$ is related to the spin $\vec{s_l}$ of the particle through the relation:

$$\vec{\mu_l} = g_l \frac{e\hbar}{2mc} \vec{s_l} \tag{1.7}$$

In 1.7 the gyromagnetic factor g_l appears: in the Dirac theory it is predicted to be exactly two for point-like particles of spin 1/2. However due to quantum corrections g_l is slightly different from two; we remind that its deviation is expressed by the quantity $a_l = (g_l - 2)/2$, the lepton anomaly.

The anomalous magnetic moment of the electron has been measured for the first time by Crane *et.al* in 1953 [21], confirming the theoretical prediction made by Schwinger in 1948 [22]. The agreement between the two results has been one of the first confirmations of the validity of QED. In the Standard Model the magnetic anomaly of a lepton has three contributions, each of them representing the nature of the interaction where the radiative corrections come from:

$$a_l^{SM} = a_l^{QED} + a_l^{weak} + a_l^{hadr} \tag{1.8}$$

In the case of the electron, the contribution to the anomalous magnetic moment from hadronic and weak loops is negligible, due to the m_l^2-dependence of these effects. This makes a_e a unique test of QED, allowing also for an extremely precise determination of the fine structure constant α [23]. On the contrary, for the muon the weak and hadronic loops (as well as possible contribution due to new physics)) are enhanced by the factor $(m_\mu/m_e)^2 \sim (200)^2$; therefore the measurement of a_μ is a high precision test not only for the QED, but more generally for the Standard Model. The same argument could be applied to the τ, but its short lifetime (of the order of 10^{-13} s) makes precision measurement of a_τ impossile.

1.3.1 Direct measurement of a_μ

The angular frequency of a particle of mass m, charge e and momentum p in a uniform magnetic field B (called *cyclotron* frequency) is

$$\omega_C = \frac{eB}{m} \tag{1.9}$$

while the spin precession is:

$$\omega_s = g \frac{eB}{2m} \tag{1.10}$$

where the proportionality with the gyromagnetic factor g comes from the relation between the spin and the magnetic moment.

This suggests the possibility of a direct measurement of the $g-2$. For high momenta, eqs. 1.9 and 1.10 become:

$$\omega_C = \frac{eB}{\gamma m} \quad \text{and} \quad \omega_s = \frac{eB}{\gamma m} + a\frac{eB}{m} \tag{1.11}$$

and the difference between the two is:

$$\omega_a = \omega_C - \omega_s = a\frac{eB}{m} = a\gamma\omega_C \tag{1.12}$$

which means for example that for instance for $a = 0.1$ the spin rotates with respect to the momentum by 1/10 turn by turn.

The experiments which have measured a_μ, the two oldest carried out from 1961 until 1970's at CERN, and the most recent one whose result was published by BNL in 2004, use pions (obtained from protons on a target) decaying in muons. Forward decay muons are higly polarized (therefore the direction of their spin is known). The muons are accumulated in a storage ring, where they decay into electrons ($\mu^\pm \to e^\pm\nu_e\nu_\tau$). The crucial point with this kind of experiments is that, given the V-A nature of the weak interaction, the favorite direction of the electron momentum is opposite to the direction of the spin of the muon. This means that if one measures the direction of the electron momentum, one knows (on the average) the direction of the muon spins. This correlation is enhanced if one cuts on the minimum energy of the detected electron. At BNL the last measurement of the negative muon anomalous magnetic moment ([24]) has been performed by counting the number of decay electrons above an energy threshold as a function of time, which is modulated with the frequency ω_a of eq. 1.12:

$$N(t) = N_0(E)e^{-t/\gamma\tau}\left[1 + A(E)sin(\omega_a t + \phi_a(E))\right] \tag{1.13}$$

where the normalization N_0, the asymmetry A and the phase ϕ_a vary with the energy E. An electrical quadrupole field is applied for vertical focusing purpose; the presence of such a field modifies eq. 1.12 and $\vec{\omega}_a$ becomes:

$$\vec{\omega}_a = \frac{e}{mc}\left[a_\mu\vec{B} - \left(a_\mu - \frac{1}{\gamma^2-1}\right)\vec{\beta}\times\vec{E}\right] \tag{1.14}$$

The dependence of $\vec{\omega}_a$ on the electric field is removed by storing muons with the 'magic' $\gamma = 29.3$, corresponding to muons of momentum $p = 3.09$ GeV. In fig. 1.6 the time spectrum for positrons with energy above 2 GeV is shown. Each line refers to a period of 100 μs. The value of ω_a is extracted from a fit of the curves shown and is used, together with a very precise measurement of the magnetic field B, to determine a_μ according to:

$$a_\mu = \frac{m_\mu}{e}\frac{\omega_a}{B} \tag{1.15}$$

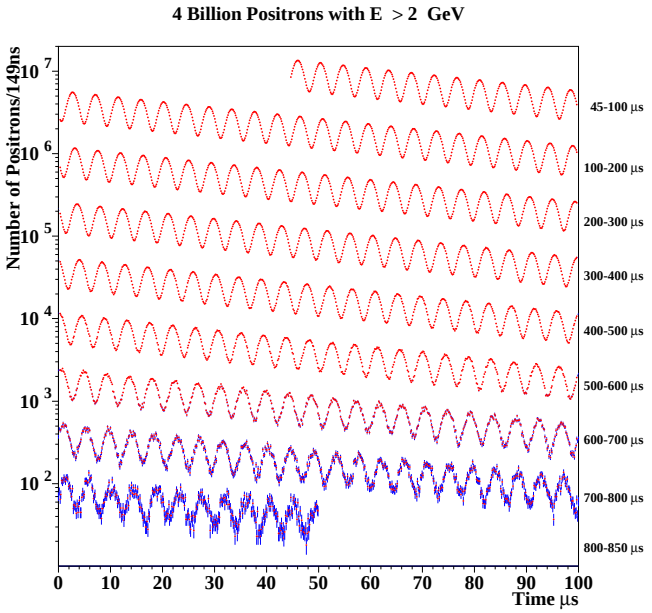

Figure 1.6: Time spectrum for positrons with energy above 2 GeV collected from January to March 2000 at BNL. Data points are shown in red, error bars in blue.

The four measurements performed at BNL are shown in fig. 1.7 together with the previous values obtained at CERN. The present world average is:

$$a_\mu = (11659208 \pm 6) \times 10^{-10} \tag{1.16}$$

1.3.2 Theoretical evaluation of a_μ

The QED contribution to a_μ is defined as the contribution arising from the diagrams containing only leptons and photons. It can be expressed in the general form:

$$a_\mu^{QED} = A1 + A2(m_\mu/m_e) + A2(m_\mu/m_\tau) + A3(m_\mu/m_e, m_\mu/m_\tau) \tag{1.17}$$

where m_e, m_μ and m_τ are the masses of the three leptons. The term $A1$ (correponding to the Schwinger term) is mass independent, while $A2$ and $A3$ are functions of the mass ratios. The functions $A_i (i = 1, 2, 3)$ can be expanded as a power series in α/π and computed order by order. The two- ([25]-[29]) and three-loops ([30]-[33]) contributions are known analytically, while most of the four-loop contributions (made up of more than 1000 diagrams) are known only numerically. The five-loops contribution is almost unknown; just a couple of estimates exists whose uncertainties dominate the error of the total QED prediction. Efforts to improve the knowledge of these terms are currently being pursued.

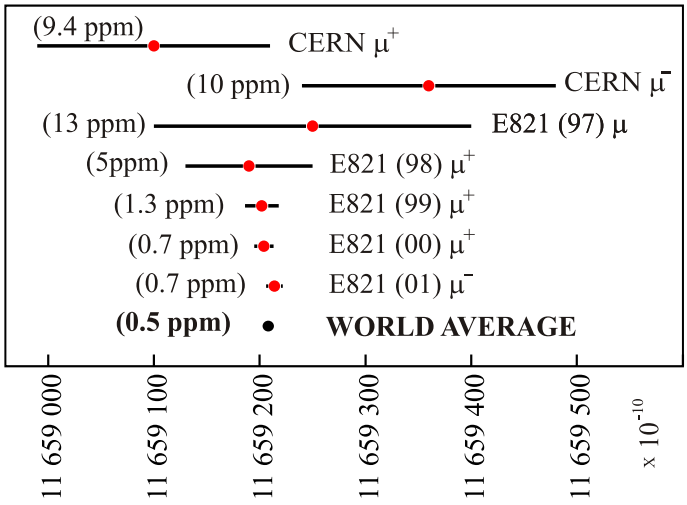

Figure 1.7: Results for a_{μ^+} and a_{μ^-} from CERN and E821.

The most recent value of the QED contribution to a_μ is [34]

$$a_\mu^{QED} = (116584718.5 \pm 0.1 \pm 0.4) \times 10^{-11} \tag{1.18}$$

The electroweak contribution to the anomalous magnetic moment of the muon is suppressed by a factor $(m_\mu/m_W)^2$ with respect to the QED effects. The one loop part was computed in 1972 by several authors and it is known analytically while the two-loops part is computed in [35] and [36]: the three give together a value of

$$a_\mu^{EW} = (154 \pm 2 \pm 1) \times 10^{-11} \tag{1.19}$$

where the first error is due to hadronic loop uncertainties in the two loop corrections and the second one accounts for the unknown Higgs mass (the mass range between 114 and 250 GeV has been assumed in this evaluation), the current top mass uncertainty and the neglected three-loops effects.

While the QED and the electroweak part of a_μ can be calculated precisely, the theoretical error of a_μ is dominated by the hadronic contribution a_μ^{hadr}. The leading order part of a_μ^{hadr}, depicted in fig. 1.1(b) can be written as the following dispersion integral:

$$a_\mu^{hadr} = \frac{1}{4\pi^3} \int_{4m_\pi^2}^{\infty} ds\, \sigma^{hadr}(s) K(s) = \left(\frac{\alpha_\mu}{3\pi}\right)^2 \int_{4m_\pi^2}^{\infty} ds\, \frac{R(s)\hat{K}(s)}{s^2} \tag{1.20}$$

It is thus the precision of $R(s)$ which determines the uncertainty of a_μ^{hadr}. Above energies of some GeV, $R(s)$ can be calculated in the perturbative QCD frame, but at low energies

one can only rely on experimental data. The kernel function $\hat{K}(s)$ is given from

$$\hat{K}(s) = \left(\frac{\alpha m_\mu}{3\pi}\right)^2 \left\{ \frac{x^2}{2}(2-x^2) + \frac{(1+x^2)(1+x)^2}{x^2}\left[ln(1+x) - x + \frac{x^2}{2}\right] + \frac{1+x}{1-x}x^2 ln(x)\right\} \tag{1.21}$$

where $x = (1-\beta_\mu)/(1+\beta_\mu)$ and $\beta_\mu = \sqrt{1-4m_\mu^2/s}$ (the function $K(s)$ is calculated in [37] and [38]). The $\hat{K}(s)$ function has a $1/s$ behavior, increasing monotonically from 0.63 at

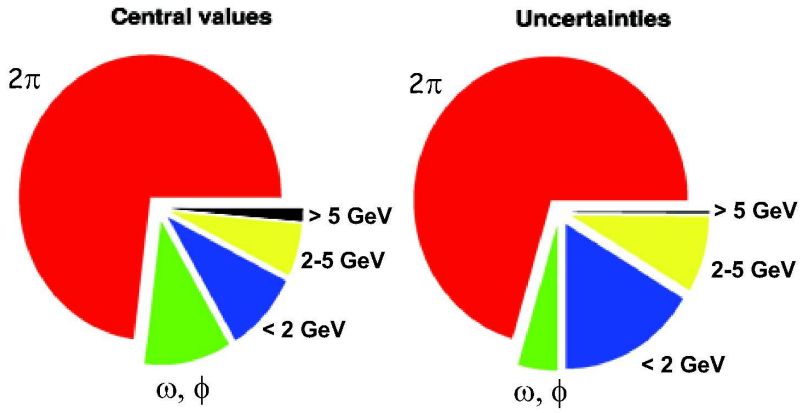

Figure 1.8: Fractions of the total contributions and (errors)^2 for a_μ^{hadr} coming from various energy intervals. The plot is taken from [39].

the two pion threshold, up to 1 at ∞. The cross-section has also an intrinsic $1/s$ behavior, enhancing hence the low energy region in the integral. About 67% of the contribution to a_μ^{hadr} comes from the region $4m_\pi^2 < s < m_\phi^2$ (see fig. 1.8). Therefore a precise measurement of the cross section $e^+e^- \to \pi^+\pi^-$, dominated by the ρ resonance, is crucial in the evaluation of a_μ^{hadr}. We will come back again to this topic at the end of this paragraph.
For the complete computation of a_μ the higher order hadronic contributions a_μ^{HHO} have to be included. They are usually divided into two terms, $a_\mu^{HHO}(vp)$ containing all the additional fermionic loops or photonic correction to the vacuum polarization diagram of fig. 1.1(b), and $a_\mu^{HHO}(lbl)$ due to the *light-by-light* diagram of fig. 1.9. The latest value for $a_\mu^{HHO}(vp)$ is [40]

$$a_\mu^{HHO}(vp) = (-97.9 \pm 0.9_{exp} \pm 0.3_{rad}) \times 10^{-11} \tag{1.22}$$

The *light-by-light* term cannot be expressed in terms of experimental quantities and its evaluation has to rely purely on theoretical considerations; its value has changed sign three times in the last decades. Its updated estimate is [41]

$$a_\mu^{LBL} = (136 \pm 25)10^{-11} \tag{1.23}$$

The total values for a_μ, according to different evaluations, are reported in tab1.1. The value in [42] uses also the measurement of KLOE. The discrepancies between the experimental

References	$a_\mu^{HLO} \times 10^{11}$	σ
e^+e^- **data**		
Davier[43]	$11659180.5 \pm 4.4_{had} \pm 3.5_{LBL} \pm 0.2_{QED+EW}$	
Hagiwara *et al.*[44]	11659180.4 ± 5.1	2.7
Hagiwara *et al.*[40]	11659183.6 ± 6.9	2.7
Ezhela *et al.*[45]	11659190.8 ± 9.2	1.6
Jegerlehner[46][47]	11659186.0 ± 9.0	2.0
Davier[48]	11659187.5 ± 7.6	2.1
de Trocóniz & Yndurain[49]	11659185.6 ± 5.5	2.7
Höcker[42]	11659184.6 ± 6.9	2.6
τ **data**		
Davier[48]	11659202.2 ± 6.3	0.7
de Trocóniz & Yndurain[49]	11659193.9 ± 5.4	1.7

Table 1.1: Standard Model prediction for a_μ. The several predictions differ each other for the leading-order hadronic contributions. For each a_μ^{hadr}, the difference between the experimental values and the theoretical prediction in terms of standard deviations is reported as well. In the evaluation reported in the first row all the most recent results from e^+e^- sector are included.

measurement and the theoretical prediction spans the range of values from 1.6 to 2.7σ in the e^+e^-- data sector, becoming smaller if considering only τ- data based evaluations. The difference between the two groups prevents them to be combined in a single Standard Model Prediction. When leaving out the theoretical τ- data based predictions (as has been proposed in the last years) it remains to be understood wheter the discrepancy between the e^+e^-- data based computation and the experimental value is due to a new physic contribution or probably due to a systematic effect not completely understood up to now. Therefore it is highly desirable that the cross section measurements are checked by independent experiments.

Let us come back now to the dispersion integral and to the data sets presently available. In the evaluation of the dispersion integral the *bare* cross section has to be used and the higher order hadronic corrections are addressed separately. In order to obtain the *bare* cross section from the measured one, one has to perform several radiative corrections, taking into

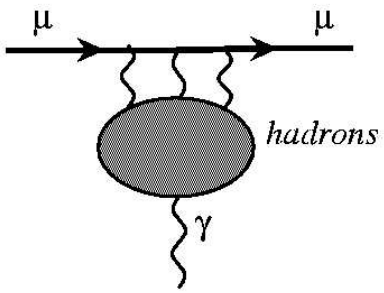

Figure 1.9: Hadronic *light-by-light* contribution to a_μ.

References	a_μ^{hadr} **in** 10^{-10} **units**
Jegerlehner[50]	692.10 ± 5.64
Davier[43]	$690.8 \pm 3.9 \pm 1.9_{rad} \pm 0.7_{QCD}$
Hagiwara *et al.*[40]	$692.4 \pm 5.9_{exp} \pm 2.4_{rad}$
Ezhela *et al.*[45]	$699.6 \pm 8.5_{exp} \pm 1.9_{rad} \pm 2.0_{proc}$
Jegerlehner[46][47]	694.8 ± 8.6
Davier[48]	$696.3 \pm 6.2_{exp} \pm 3.6_{rad}$
de Trocóniz & Yndurain[49]	$694.4 \pm 4.8_{exp} \pm 1.0_{rad}$
Höcker[42]	$693.4 \pm 5.3_{exp} \pm 3.5_{rad}$

Table 1.2: Recent evaluations of the leading-order hadronic contribution to a_μ based on e^+e^- data. All the estimates contains the new results (after the ri-analysis) of CMD-2, while the the first and last one contains the measurement from KLOE.

References	a_μ^{hadr} **in** 10^{-10} **units**
Davier[48]	$711.0 \pm 50_{exp} \pm 8_{rad} \pm 28_{SU(2)}$
de Trocóniz & Yndurain[49]	$702.7 \pm 47_{exp} \pm 10_{rad}$

Table 1.3: Recent evaluations of the leading-order hadronic contribution to a_μ based on τ data.

account also the initial state radiative corrections, described by pure QED. Moreover the measured cross section contains the effect of the photon vacuum polarization, and it has to be *undressed* with respect to that. Finally the computation of the final state radiation effects (namely the effect of photons emitted in the final state from one of the hadrons) is also necessary, and here a certain model-dependence enters. The problem with data from old experiments is to understand if, and in the case how, all these corrections have applied. The latest published results from CMD-2, SND and KLOE are both corrected for the above mentioned effects. Table 1.2 reports some recent evaluations of the leading-order hadronic contribution to a_μ based on e^+e^- data. The last entry of the table contains also the result that KLOE has obtained for the cross section $e^+e^- \to \pi^+\pi^-$ [11]. Before the KLOE measurement was published the low mass region relied completely on the result of one single experiment, i.e. the CMD-2 experiment. The reported evaluations are well in agreement with each other; the theoretical uncertainty has been improved with respect to the past thanks to the new measurements; the quoted uncertainties are mainly due to experimental errors, besides missing radiative corrections and the error coming from the integration procedure. The evaluations presented in tab. 1.2 have to be compared with the two recent computation of a_μ^{HLO} based on τ data and are shown in tab. 1.3.

The most recent results in the $\pi^+\pi^-$ channel of the e^+e^- experiments are compared in fig. 1.10(a) by plotting the CMD-2 and SND data points relative to the interpolated KLOE data points. Sixty points between 0.35 and 0.95 GeV^2 of the KLOE spectrum have been interpolated; the obtained curve is then compared with SND (in red) [8] and with the results CMD-2 obtained analyzing the data collected in 1995 (in green) [6] and the ones collected

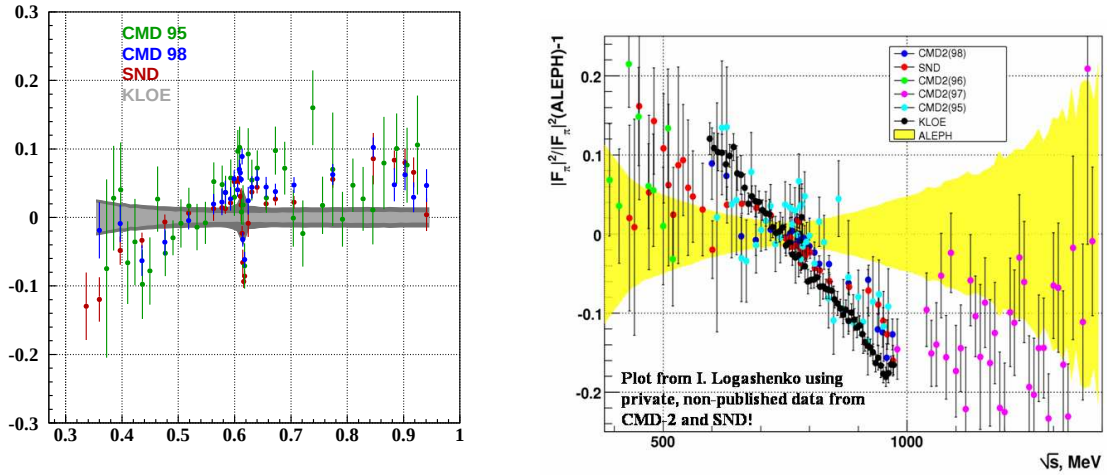

(a) (b)

Figure 1.10: (a) Comparison among the band obtained with an interpolation of 60 KLOE points in the energy range 0.35 - 0.95 GeV^2 and the CMD-2 and the SND data points (b) Comparison among the different spectral functions obtained both from e^+e^- and in τ data, among which the new preliminary data from SND [51]

in 1998 (in blue) [52]. In this plot the light gray band indicates the statistical error of the KLOE spectrum and the dark gray stands for the systematic one. For the other two experiments only the statistical errors are considered. Some disagreement between KLOE and CMD2/SND is observed.

Nevertheless, even if not in a perfect agreement with each other, all the e^+e^--data sets show the same trend when compared with the τ spectral function, as shown in fig. 1.10(b) (this plot does not included the last result of CMD-2, of the data collected in 1998). In this plot the e^+e^--experiment points are plotted relative to the ALEPH measurement, coming from τ-data. The yellow band indicates the error of ALEPH measurement. It is evident that the e^+e^- experiment see large deviation to τ-data in all the spectrum

There has been recently a new preliminary result from the Belle collaboration in the τ-sector: they have obtained the pion form factor from the τ decay $\tau \to \pi^-\pi^0\nu$ [53]: the comparison of their result with the pion form factor measured by CLEO and ALEPH is shown in fig. 1.11(a). The new Belle result is systematically lower than the previous two, going into the direction of the e^+e^- experiments, as shown in fig. 1.11(b). This is the same plot like fig. 1.10(b) including the preliminary measurement of Belle. Besides the general need of having more data on hadronic cross section, the region below the ρ mass especially requires more precision. Indeed it gives a large contribution to a_μ (around 13% for $\sqrt{s} < 0.61$ GeV) and it is still poorly known. New possibilities for measuring hadronic cross sections are offered by the *radiative return*, which has been used for the first time

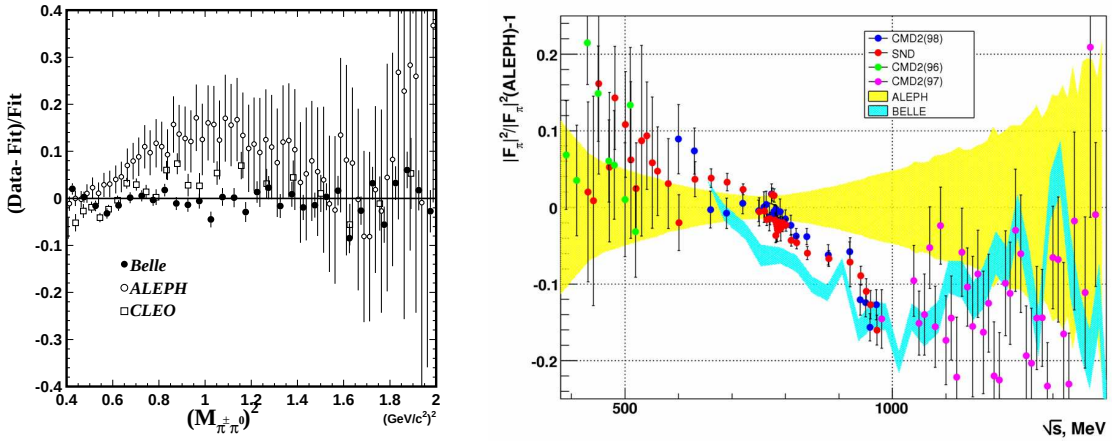

(a) (b)

Figure 1.11: (a) Comparison of the pion form factor squared $|F_\pi(s)|^2$ measured by Belle to that measured by CLEO and ALEPH (from [53]). (b) As in 1.10(b) with the addition of the preliminary result from Belle (plot from [51]).

by KLOE in its measurement of $\sigma(e^+e^- \to \pi^+\pi^-)$ as will be discussed in more details in chapter 3.

1.4 The running of α

The fine structure constant α is a fundamental input parameter of the electroweak Standard Model. Vacuum polarization by virtual pairs tend to screen partially the electrical charge, modifying the value of the *bare* charge e. The charge screening effects determine a redefinition of the classical charge e^2. This constant must be replaced by a *running charge* depending on the energy scale s as:

$$e^2 \to e^2(s) = \frac{e^2 Z}{1 + \prod'_\gamma(s)} \tag{1.24}$$

where Z is a renormalization factor fixed by the condition that $e^2(s)$ equals the classical charge in the limit $q^2 \to 0$ and $\prod'_\gamma(s)$ is the photon vacuum polarization amplitude. The electrical charge e is less screened at low momentum transfer ($s \to 0$), while the strength of the interaction grows with the energy. This is the reason why the value for the coupling constant at m_Z^2 is significantly larger than the one in the limit at $s \sim 0$. Exactly as for the muon anomalous magnetic moment, it is the limited knowledge of the hadronic vacuum polarization that dominates the uncertainty for $\alpha(m_Z^2)$. The *running* of α is usually written as:

$$\alpha_{em}(s) = \frac{\alpha_{em}(0)}{1 - \Delta\alpha(s)} \tag{1.25}$$

where $\Delta\alpha$ is composed of different contributions:

$$\Delta\alpha(s) = \Delta\alpha^{lep}(s) + \Delta\alpha^{hadr}(s) + \Delta\alpha^{top}(s) \tag{1.26}$$

The leptonic contribution is directly calculated and it is known up to three-loops [54] at $s = m_Z$ and equal to

$$\Delta\alpha^{lep}(m_Z^2) = 314.98 \times 10^{-4} \tag{1.27}$$

The contribution from the top quark is very small [55]:

$$\Delta\alpha^{top}(m_Z^2) = -0.7 \times 10^{-4} \tag{1.28}$$

As for the hadronic contribution to the muon magnetic moment, the hadronic contribution to $\Delta\alpha^{hadr}(s)$ can be expressed via a dispersion integral:

$$\Delta\alpha^{hadr}(s) = \frac{-e^2 s}{12\pi^2}\,\Re\int_{4m_\pi^2}^{\infty} ds^{'}\,\frac{R(s^{'})}{s^{'} - s - i\epsilon} \tag{1.29}$$

and again R is an experimental input for the low mass region. Assuming pQCD to be applicable above some energy E_{cut}, eq. 1.29 can be written as:

$$\Delta\alpha^{hadr}(s) = \frac{-e^2 s}{12\pi^2}\left(\Re\int_{4m_\pi^2}^{E_{cut}} ds^{'}\,\frac{R(s^{'})}{s^{'} - s - i\epsilon} + \Re\int_{E_{cut}}^{\infty} ds^{'}\,\frac{R(s^{'})}{s^{'} - s - i\epsilon}\right) \tag{1.30}$$

Different theoretical approaches have been used to evaluate $\Delta\alpha^{hadr}(s)$: they differ for the choice of E_{cut} in the dispersion integral or in the way the different data sets are combined. Some authors assume the validity of pQCD already above 1.8-2.5 GeV ([56],[55],[57],[58]), others prefer to use experimental data up to 12 GeV, most of all in the resonance region ([58], [59]). All these different evaluations are in a reasonable agreement with each other (see fig. 1.12).
Also the τ spectral function have been used for the evaluation: the difference between e^+e^-- and τ-data based approach has been calculated in [48] and yields:

$$\Delta\alpha(e^+e^-) - \Delta\alpha(\tau) = (-2.37 \pm 0.62) \times 10^{-4} \tag{1.31}$$

which is bigger than the uncertainties of the mean value of α.
In order to obtain more precise estimates for α more accurate measurements of hadronic cross section are needed. Fig. 1.13 shows the relative contribution of different energy region to the magnitude and uncertainty of $\Delta\alpha^{hadr}(M_Z^2)$. In the standard approach, using the R-ratio as experimental input up to 12 GeV, the largest contribution to $\Delta\alpha^{hadr}$ comes from the 1-2 GeV and 2-5 GeV energy region. However, if pQCD is used already for $\sqrt{s}$ >1.8 GeV, a precise measurement of the hadronic cross section below 1 GeV plays a more important role in the reduction of the uncertainty of $\Delta\alpha$.

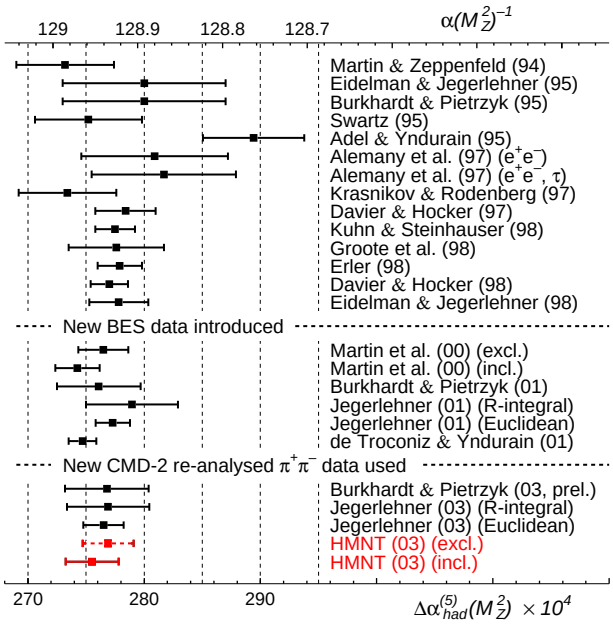

Figure 1.12: Recent evaluations of α^{hadr} (lower scale) with the corresponding value of $\alpha(M_Z^2)^{-1}$ at the Z boson mass shown in the upper scale [40].

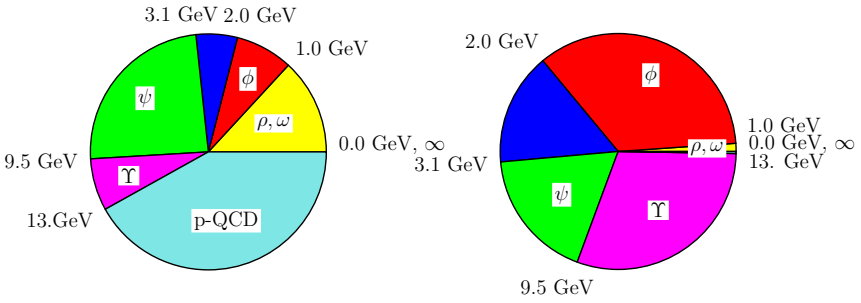

Figure 1.13: Fractions of the total contributions (on the left) and (errors)^2 (on the right) to $\Delta\alpha^{hadr}(M_Z^2)$ coming from different energy intervals. The plot is taken from [50]

1.5 The pion form factor

The form factor describes the interaction between a photon and the observable hadrons. For the two pion final state $F_\pi(s)$ parametrizes the coupling between the photon and the $q\bar{q}$ pair hadronizing into a resonant state that subsequently decays into two pions. It contains thus all the parameters of the corresponding resonance and can be directly related to the

cross section $\sigma(e^+e^- \to \pi^+\pi^-)$ via the relation:

$$\sigma_{e^+e^-\to\pi^+\pi^-}(s) = \frac{\pi\alpha^2}{3s}\beta^3|F_\pi(s)|^2 \tag{1.32}$$

with s the center-of-mass energy squared, m_π the charged pion mass and $\beta_\pi = \sqrt{1-4m_\pi^2/s}$ the pion velocity in the center-of-mass frame.

In the form factor all possible effects which are represented in the blob of fig. 1.1(a) are included. Therefore its measurement can be used to determine all the properties of the underlying hadrons, where the reaction proceeds to. Particularly interesting are the parameters for isospin violating effects, like the $\rho - \omega$ interference, which creates an observable effect in the data spectrum at $s = m_\omega^2$. Several theoretical parametrizations for the pion form form factor exist. The CMD-2 collaboration in the fit to their experimental pion factor uses a parametrization for $\rho(770)$- and $\rho(1450)$-mesons due to Gounaris and Sakurai [60]. A different parametrization is given by Kühn and Santamaria [61] and is the one used in the PHOKHARA Monte-Carlo generator ([62], [63], [64]), which is the reference $e^+e^- \to \pi^+\pi^-\gamma$ events generator used by KLOE.

Chapter 2

The KLOE experiment

The KLOE experiment has collected data from 2000 up to march 2006 at the e^+e^- collider DAΦNE at Frascati (Italy). In the present chapter both the DAΦNE machine and the KLOE detector are described.

2.1 The DAΦNE accelerator

The DAΦNE [1] ϕ-factory is an e^+e^- collider running at a fixed center-of-mass energy with high luminosity. Operating at a center-of-mass energy of the ϕ-meson (m_ϕ=1019.44 MeV), DAΦNE is optimally suited for kaons physics, due to the fact that the ϕ decay fraction into kaons (neutral and charged) is 83%. The physics program of KLOE covers the measurement of all kinds of kaon braching ratios (but also the study of radiative ϕ decays and of the continuum below 1 GeV), while the DEAR (DAΦNE Exotic Atoms Research) experiment investigates kaonic hydrogen which is produced stopping K^- in a gaseous hydrogen target. Finally FINUDA (FIsica NUcleare a DAΦNE) studies hypernuclei which are produced stopping a low energetic K^- in a thin target via the reaction $K^-+n \rightarrow \Lambda+\pi^-$. Additionally DA$\Phi$NE is a laboratory for synchrotron light due to the high electron currents which are stored in one of its two rings.
In fig. 2.1 the layout of the DAΦNE complex is shown. In the $\sim$60 m long linear accelerator the electrons are accelerated up to 250 MeV and focused to a spot of 1 mm radius. They collide with a removable target made of tungsten to produce positrons. They are separated from the electrons by means of magnetic dipoles and then accelerated up to 550 MeV. In the electron mode the converter is removed from the beam and the electrons are accelerated up to a maximum energy of 800 MeV. The particles from the LINAC are injected into the accumulator ring, which has a circumference of 32.6 m. Here the particles are decelerated to 510 MeV and the beam characteristics, as energy spread and acceptance, are improved.

[1] Double Annular ϕ-factory for Nice Experiments

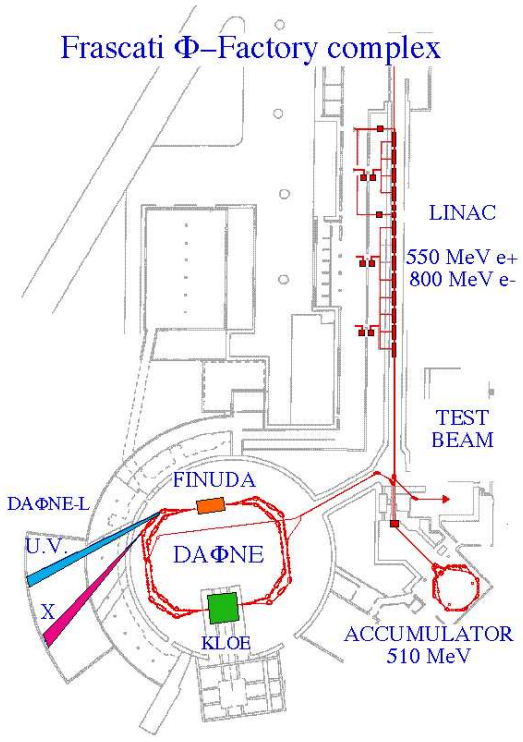

Figure 2.1: The DaΦNE ϕ factory in Frascati.

The accumulator contains only one particle type (electrons or positrons) at a time. After the bunch has reached the desired number of particles, it is injected into one of the two main rings. This can be done while the beams are circulating without interrupting the data taking process (*topping up*). The main rings have a circumference of 97.7 m and are coplanar to each other. At the two Interactions Points (IP) beam-beam interactions are strongly reduced by focusing the beams (*low-beta technique*). The presence of two different rings forces the beams to meet at a crossing angle of $\sim$25 mrad; as a consequence the ϕ mesons are produced with a small momentum component in the horizontal plane towards the ring center, $p_x \sim 13$ MeV. The double annular structure minimizes the beam-beam interactions and allows to achieve a high luminosity by increasing the number of bunches circulating in the collider, while the number of particles in the single bunch is limited by intra-beam interactions. The maximum number of storable bunches is 120, corresponding to an inter-bunch time of $\sim$2.7 ns. Furthermore, since the dumping due to the synchrotron radiation is too small, the emission of synchrotron radiation is doubled by the use of 8 conventional electromagnets (wigglers).

The two interaction points are completely surrounded by detectors. The KLOE experiment occupies permanently one of the two interaction regions (IR). The DEAR experiment has taken data in 2002 at the second IR, before the insertion of the FINUDA detector during the shutdown of 2003. Since commissioning in 1999, the collider has undergone major modifications in order to improve its performances. About 99% of its original magnets have

Beam energy [MeV]	510
Trajectory length [m]	97.69
RF frequency [MHz]	368.26
Bunch spacing [ns]	2.7
Particles/bunch [10^{10}]	8.9
Maximum design luminosity [$\mathrm{cm}^{-2}s^{-1}$]	5.3 $\times 10^{32}$

Table 2.1: Some of the DAΦNE parameters in 2002.

been exchanged, the beta-parameters have been further reduced to increase the luminosity and allows $\sim$ 100 bunch collisions, new interaction regions have been installed during the shutdown of 2003. A brief summary of the design parameters of the collider is listed in table 2.1

2.2 The KLOE detector

The KLOE detector [2] is a general-purpose detector permanently installed in one of the two interaction regions of DAΦNE. The detector has been optimized do detect all charged and neutral decays of K_S and K_L mesons. It consists essentially of a cylindrical drift chamber to detect charged particles and an electromagnetic calorimeter allowing to detect photons down to 10 MeV, which surrounds the drift chamber almost hermetically (see fig. 2.2). Both the drift chamber and the calorimeter are placed in a superconducting coil providing a longitudinal magnetic field of 0.52 T.

[2] K LOng Experiment

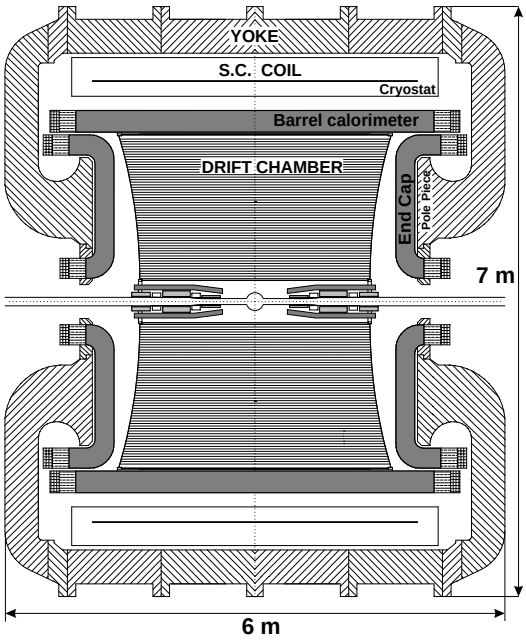

Figure 2.2: Section of the KLOE detector.

2.2.1 The drift chamber

The design of the KLOE drift chamber has been driven by the event topology of the K_L decay. At the energies of DAΦNE the mean decay length of a K_L is 3.43 m and the angles with respect to the z-axis are distributed as $sin^2(\theta)$; to detect them the chamber has to have a high and uniform reconstruction efficiency over a large volume, in order to deal with the long decay path of K_L and the isotropic distribution of its decay products. The shape of the chamber is a 3.3 m long cylinder with 25 cm of inner radius and 2 m of external one [65]. The requirements of three-dimensional track reconstruction led to drift cells almost squared arranged in coaxial layers. All the wires belonging to the same layer are parallel to each other and have the same stereo angle with the line parallel to the z-axis, passing through the end plate of the chamber where the wire is connected, see fig. 2.3(a). The stereo angles alternate from one layer to the next, and their magnitudes vary from ± 60 to ± 150 mrad. These values assure a good resolution of the measurement of the z-coordinate: being $\sigma_z = \sigma_{r\phi}/tan(\epsilon)$ and with an average $r\phi$ resolution of 200 μm, the z resolution is about 2 mm over the whole chamber volume. The ratio between field and sense wires is 3:1. Field wires are also disposed in concentric layers following the stereo angles of the sense wires layer above them. Since the track density is much higher at small radii due to the relatively small momenta of charged particles produced in the ϕ decays and since vertexing of $K_S \to \pi^+\pi^-$ is required, the innermost layers have cells of smaller size (see fig. 2.3(b)), being the dimensions 2×2 and 3×3 cm^2 respectively. Simulation studies have shown that

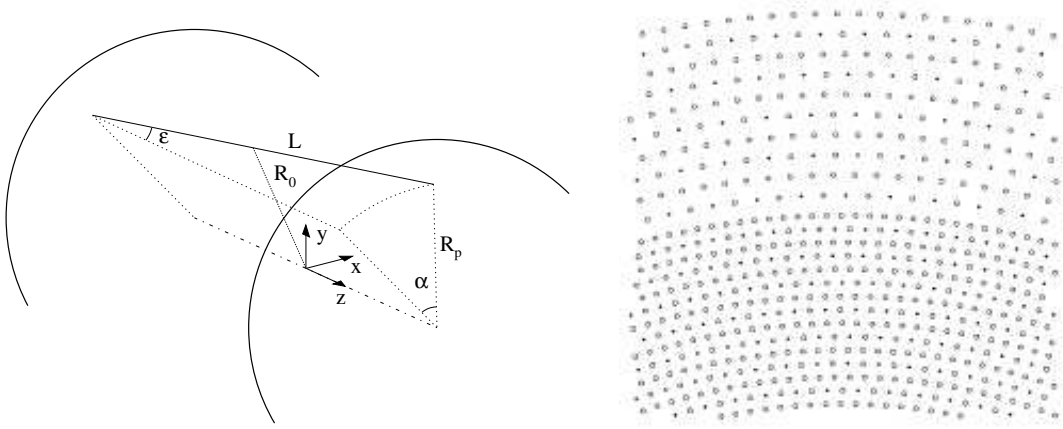

(a) (b)

Figure 2.3: (a) Sketch of the stereo angles of the cells. (b) Drift cells configuration at z=0; a portion of the chamber at the boundary between small cells in the inner layers and large cells in the outer cells is shown. Full dots indicate the sense wires while the circles indicate the fields wires.

good efficiency and spatial resolution are achieved with a helium-based gas mixture (which minimizes multiple scattering), with a gain of ∼10^5, together with gold-plated tungsten 25

μm thick sense wires and silver-plated aluminum 80 μm thick field wires at a voltage of 1800-2000 V. The number of layers is 58, of which 12 consist of small cells and 46 of big ones. The number of drift cells increase by ΔN=6 from one layer to the next, with a total number of 12585 drift cells, corresponding to about 52000 wires (field plus sense).
The gas which fills the chamber is a 90% helium, 10% isobutane mixture. The helium is the active element and thanks to its low atomic mass reduces the effect of multiple scattering and regeneration. The isobutane absorbs UV photons produced in recombination processes (in order to avoid the production of discarge in the chamber). The mixture has a radiation length $X_o \simeq$1300 m; taking into account also the presence of the wires, the average radiation length in the whole chamber volume is about 900 m.
Since the number of cells is a multiple of six for each layer, connections to the wires are grouped by six. The bulk of ionization in the chamber is due to beam background and decreases with radius. For this reason the number of sense wires connected to one high voltage line increases with the radius. The preamplifier outputs are sent to an amplifier-discriminator-shaping circuit (ADS). This circuit provides a discriminated signal for the TDC (for drift time measurement) and the ADC (for dE/dx measurements), plus a further signal sent to the trigger module.
The momentum resolution for electrons with 510 MeV energy and polar angles $50° < \theta < 130°$ is $\sigma_p \simeq 1.3$ MeV (relative resolution σ_p/p=2.5$\times 10^{-3}$, as shown in fig. 2.4).

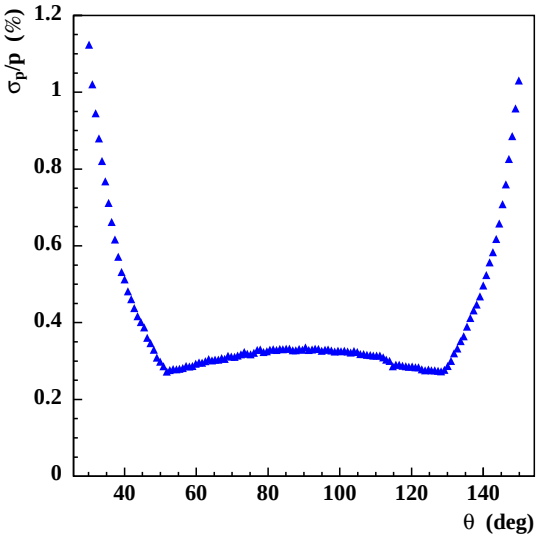

Figure 2.4: Momentum resolution σ_p/p as a function of the polar angle θ for Bhabha events.

2.2.2 The electromagnetic calorimeter

The flight path of a K_L particle before decaying into π^0 is obtained from the measurements of the time of arrival of the two photons (from the π^0 decay) in the calorimeter. Neutral kaons from ϕ-decays travel with a velocity $\beta \sim 1/5$: in order to determine the K_L flight

path with a precision of ∼0.6 cm, a precision of 100 ps in the time measurement is needed. Hence, special KLOE needs are very good time resolution, full solid angle coverage and as few amount of material in front of the calorimeter as possible. The energy resolution requirements are not particularly stringent, ∼5% at the maximum energy of 1000 MeV. A lead-scintillating fiber sampling calorimeter has been designed to fulfill these requests [66]. Scintillating fibers offer several advantages, in particular they provide good light transmission over the whole distance, up to ∼4.3 m. The barrel has an almost cylindrical shape, consisting of 24 modules 4.3 m long, 23 cm thick with a trapezoidal cross section. Two endcaps, made of 32 vertical volumes 0.7 to 3.9 m long and 23 cm thick, close the cylinder. Their cross section is rectangular, of variable width. Thanks to the large overlap of barrel and endcaps, the calorimeter has no inactive gap at the interface of the three components. The central endcap modules are vertically divided into two halves to allow the passage of the beam-pipe.

All modules are made of 200 grooved, 0.5 mm thick lead foils alternating with 200 layers of 1 mm diameter scintillating fibers, glued together (see fig. 2.5). The ratio, by volume, lead:fiber:glue is 42:48:10; the total thickness of the calorimeter is 23 cm, corresponding to 15 radiation lengths, in order to contain the whole electromagnetic avalanche. The read-out at both sides of each module is connected via light pipes of plexiglas to photomultipliers. The whole calorimeter is split in five planes in depth, the last one being thicker than the other four. In the transverse direction each plane is subdivided into cells 4.4 cm wide. The set made of five cells lined up, one for each transverse plane, is named a *column*. The photomultipliers work in a magnetic field of 0.56 T; the outer parts of the endcaps have been designed to minimize the transverse component of the field acting on the photomultipliers axis. The residual of such a component is < 0.4 kG. Since the time resolution depends also on the efficiency of the light collection, this quantity has been maximized, up to a value of ∼80-90%. The signal coming out from the photomultipliers passes through a preamplifier, before being split into three different circuits: a first part goes to the trigger, the other two parts to the ADC's and the TDC's respectively. The energy deposit in each cell is obtained by the charge measured at each side of the modules by the ADC's. The time of arrival of a particle is derived from the time intervals measured at each side of the modules by the TDC's. The difference between the arrival time at the two ends of the fiber allows to reconstruct the coordinate along the fiber. The resolution of the longitudinal z coordinate is $\sigma_z \sim 9$ mm $/\sqrt{E(GeV)}$. The energy resolution and the linearity of the calorimeter are determined using radiative Bhabha events, whose photons cover a wide energy and angular range. With the information coming from the drift chamber one obtains the photon direction and the photon energy E_γ with good accuracy. What is required is the matching of the photon direction obtained from Bhabha events and from the position in the cell of the calorimeter determined from the time-of-light. For each 10 MeV energy interval in E_γ, the distribution $E_{cl} - E_\gamma$ is fitted with a gaussian to find its central value. The plot of fig. 2.6(a) shows the results of this procedure for the whole

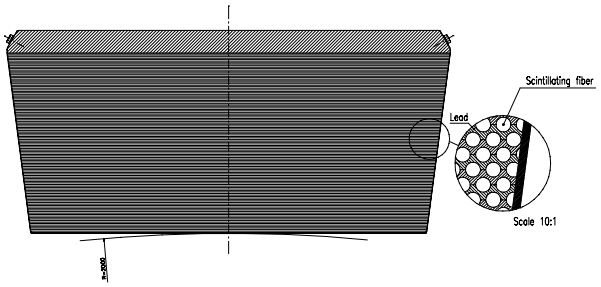

Figure 2.5: Fiber-lead sampling structure of the KLOE calorimeter.

energy range E_γ: the linearity is better than 1% for E_γ >75 MeV. Deviations of the order of 4-5% are observed at low energies, mainly due to the loss of parts of the shower in the cluster reconstruction. The energy resolution, dominated by sampling fluctuations, can be parametrized as $5.7\%/\sqrt{E(GeV)}$ (see fig. 2.6(b)). The photon detection efficiency is

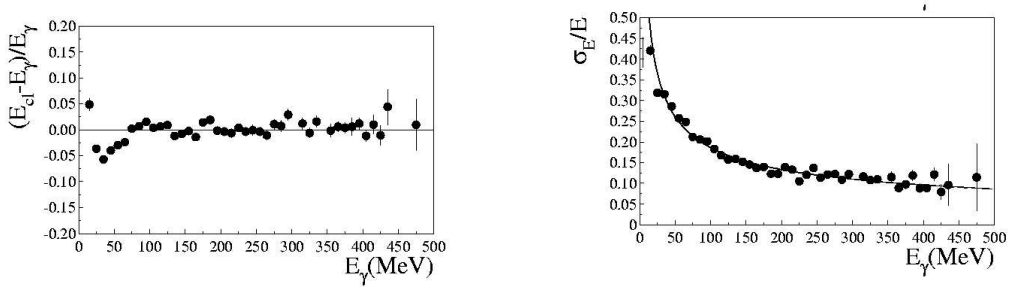

(a) (b)

Figure 2.6: Calorimeter linearity (a) and resolution (b) for photons as a function of the photon energy E_γ. The resolution is parametrized with $5.7\%/\sqrt{E(GeV)}$.

defined as the number of detected clusters divided by the number of produced photons. It has been measured with different samples: here we report the result obtained with radiative Bhabha events (where $e^\pm$ direction and energy are measured with the drift chamber), with the decays $\phi \to \pi^+\pi^-\pi^0$ and $K_L \to \pi^+\pi^-\pi^0$ (where energy and direction of one of the two photons from the π^0 is deduced from the tracking information and the energy and direction of the other photon) (see fig. 2.7(a)). The results obtained with the different channels are in reasonable agreement with each other, and for energies larger than 100 MeV a constant value of more than 98% is observed.

The time resolution is given in fig. 2.7(b) for photons from different radiative ϕ decays. Good agreement among the different measurements is observed down to 100 MeV. The curve in the plot gives the resolution of the calorimeter: $\sigma_t = 54$ ps$/\sqrt{E(GeV)} \oplus 140$ ps.

2.2.3 The trigger system

The KLOE trigger system has to discriminate among events from ϕ decays and Bhabha events, cosmic rays and machine background. The time between bunch crossings at DAΦNE is 2.7 ns; this is too short to generate a trigger. That is the reason why the KLOE trigger operates in a continuous mode. The signal from the trigger is synchronized afterward to the bunch crossing time. At the full design luminosity, a total rate (physical events plus background) of ∼90 kHz is produced, ∼5 kHz coming from ϕ production, ∼80 kHz from Bhabha and machine background rates with about 40 kHz from each and the remaining ∼5 kHz from cosmic rays. The Data Acquisition (DAQ) can handle a total rate up to ∼10 kHz. The trigger must provide good background rejection in order not to overload the DAQ, without losing efficiency of the physical events. Both calorimeter and drift chamber can be

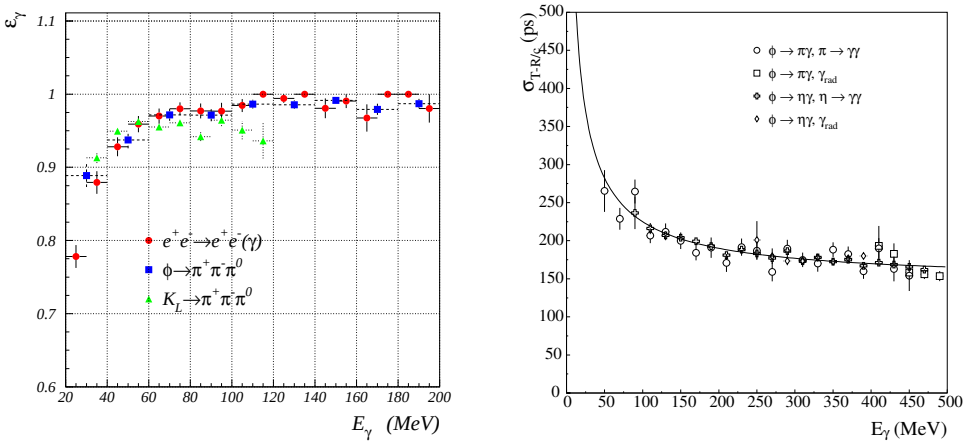

(a) (b)

Figure 2.7: (a) Calorimeter efficiency for different ϕ decays and (b) time resolution for ϕ radiative decays, both as a function of E_γ .

used to generate the trigger [67], since the combined information of the two devices allows to distinguish several processes. Also the topology of the different reactions is crucial in the separation. For example, low angle Bhabha events are concentrated in the two endcaps of the calorimeter as well as the machine background. Both produce a low multiplicity in the drift chamber, in contrast to the ϕ-decay events. Cosmic rays behave differently from the these two background sources: ∼85% of them deposit their energy in the barrel, and their multiplicity in the chamber is similar to the one of physical events.

The trigger is based on the local energy deposit in the calorimeter and multiplicity information from the drift chamber. It works in two levels (see fig. 2.8). An early trigger with fast timing (to start the front-end electronic read-out) is generated which uses as much information as possible from the chamber. After the arrival of this first level trigger,

additional information is collected from the drift chamber and used, together with the clorimetric information, to constrain the former and start the DAQ. The calorimeter triggers if the local energy deposits are larger than a programmable threshold. Two thresholds are fixed for each calorimeter signal, the first at low energy ∼50 MeV, in order to trigger on low energy particles from ϕ decays, and the second one at high energy ∼350 MeV, in order to identify Bhabha events. These latter are rejected or accepted as downscaled sample to be used for the calorimeter calibrations. The signals from the wires of the chamber, after being preamplified, are sent to a TDC and the trigger signal is formed with a width of 250 ns. The first level trigger can be summarized as follows:

ϕ trigger: (2 Low-Energy-Threshold hits with barrel-barrel, barrel-endcaps or endcaps-endcaps topology) or (15 drift chamber hits within 250 ns)

Bhabha veto: 2 calorimeter signal lower than the high threshold with barrel-barrel or endcaps-endcaps topology.

The level 1 trigger T1 sets a 2 μs long signal, which vetoes the other first level trigger and allows signal formation from the drift chamber cells.

Before being passed to the front-end electronics of the calorimeter, the first level trigger is synchronized with the DAΦNE radio-frequency. Therefore the calorimeter TDCs measure the time with respect to a bunch crossing coming n periods after the collision which has originated the event, where n is then determined at offline reconstruction level.

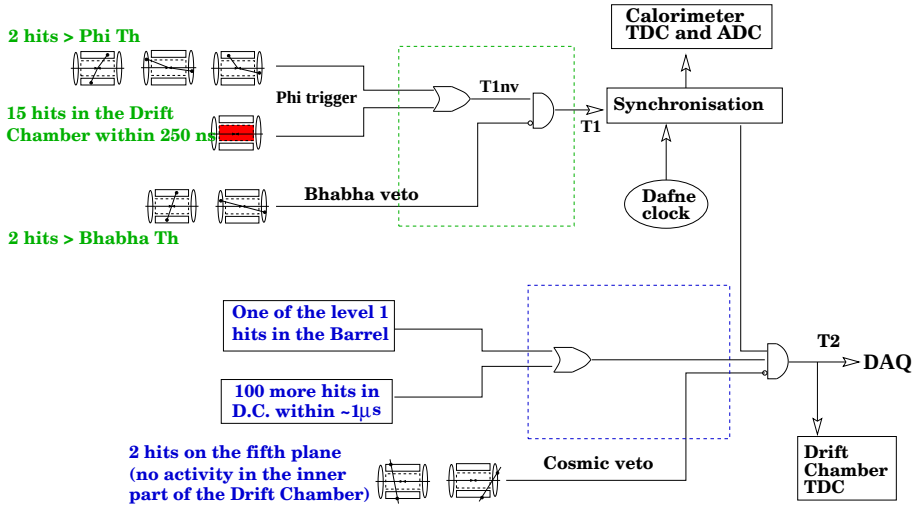

Figure 2.8: KLOE trigger logic.

At the end of the dead time (2 μs) the trigger system asks for the confirmation of the level 1 decision. In the second level two conditions similar to the ones of the first level are requested, but the thresholds now are chosen to be equal to the energy average released in a cell by a minimum ionizing particle MIP (40÷50 MeV). Once two sectors are above threshold, the cosmic ray bit is activated and the event is flagged as cosmic. The cosmic flag requires two energy releases above threshold on the outermost plane of the calorimeter in

barrel-barrel or barrel-endcap configuration. The level trigger T2 produces the stop signal for the chamber TDC's and starts the data acquisition. It can be summarized as follows:
ϕ trigger: (at least 1 calorimeter hit in the barrel or 3 in the same endcap) or (40 drift chamber hits detected during 850 ns after T1)
cosmic flag: 2 hits on the external plane of the calorimeter with barrel-barrel or barrel-endcap topology.
To avoid the rejection of $\mu^+\mu^-(\gamma)$ (and $\pi^+\pi^-\gamma$) events, which arrive easily at the outer planes of the calorimeter, a third level trigger T3 has been developed. Each event flagged by T2, will pass the T3 filter before being written on tape or rejected. The T3 filter performs a fast preliminary pattern recognition looking for tracks coming from the interaction point. If it finds no tracks from the IP, the event is rejected. The insertion of the T3 filter from beginning of the year 2002 was very important for the measurement of the $\pi^+\pi^-\gamma$ channel, reported in this thesis, since it increased significally the efficiency of signal events with respect the 2001.

EMC trigger

For the trigger purpose the whole granularity of the calorimeter is not needed and the 5000 readout channels are grouped in ∼200 summed signals. The barrel is divided into three groups of 47 trigger channels, named *normal, overlap* and *cosmic* series. Each sector in the *normal* and *overlap* series is made of 5×6 columns (see fig. 2.9), while the *cosmic* series (used for the cosmic flag) consists only of the cells of the fifth plane of the calorimeter. In total there are 48×3 sectors. The geometry of the trigger sectors in the endcaps is more complicated, and, like for barrel, it consists of the *normal* and *overlap* series. Since the multiplicity is higher in the forward region, mostly due to background, the two series are segmented in groups of 4 columns in the zone close to the beam pipe, and 5 or 6 elsewhere. The signals from the cells forming a column are summed up, followed by the sums of the six columns of a given trigger sector. The analog signal of each trigger sector is performed at both sides (labeled A and B in the following) and it is compared to a high and a low threshold which are fixed during the DAQ initialization. The four logical signals $T_A^{low}, T_A^{high}, T_B^{low}$ and T_B^{high} generate the signal T for each sector according to the logical equation: $T = (T_A^{low}$ and $T_B^{low})$ and $(T_A^{high}$ or $T_B^{high})$. This two-threshold scheme is applied in order to obtain as much as possible uniform response as a function of the coordinate along the fibers of the energy deposit, minimizing thus the effect of the light attenuation along the fibers.

2.3 Data reconstruction and event classification

KLOE started its data taking for physics events in 2000. Between the year 2000 up to 2006 (with a long interruption in 2003) an integrated luminosity of 2.5 fb^{-1} has been collected and the data taking has been definitely stopped in March 2006. In the last three months

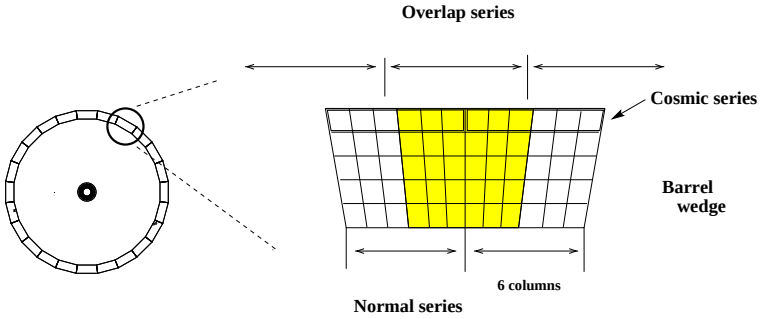

Figure 2.9: Trigger sector in the barrel. The two series, the *normal* ans the *overlap* are shown.

of data taking the center-of-mass energy of DAΦNE was reduced to $\sqrt{s}$=1000 MeV (off-resonance) in order to allow a background-free measurement of t he hadronic cross section via radiative return.

2.3.1 Data reconstruction

The data acquisition system (see [68]) handles about 23000 front end channels from the drift chamber, the calorimeter and the trigger. It can manage a readout of 10 MB/s. For the typical peak luminosity of 2002 (5×10^{31} cm^{-2}s^{-1}), the trigger rate was 1.6 kHz and the average event size 2.7 kB, leading to a data acquisition of 4.3 MB/s. This latter was handled by only three out of seven on-line nodes.
The on-line server writes raw data in 1-GB files. Data taking is divided into runs of approximately the same integrated luminosity (200 pb^{-1} in 2002) and the run number associates uniquely machine parameters, calibration constants (see §2.3.2 and 2.3.3) and all the relevant quantities of the detector related to the specific run. Raw data are kept on disk until calibration and reconstruction are completed. The reconstruction process starts immediately after the completion of the calibration jobs for the run. Each of the 20 jobs, which is divided into the raw data file corresponding to a single run, are processed in parallel by a separate reconstruction job. The reconstruction program consists in several modules performing the following task:

- loading the drift chamber and the calorimeter calibration constants;
- calorimeter clusters reconstruction and determination of the time of flight and of the energy deposition;
- determination of the current bunch crossing;
- rejection of the machine background and cosmic ray events;
- track fitting of the charged particles;
- vertex reconstruction for the charged particles;

- association of the drift chamber tracks with the calorimeter clusters for charged particles hitting the calorimeter;
- event classification and streaming into one of the physical stream.

Machine background and cosmic rays events are filtered out before the tracking procedure, which is the most CPU-intensive reconstruction task. The filter algorithm (FILFO) is based only on information from the calorimeter. The last step of the reconstruction procedure is the classification of events on the basis of topological information into different streams. Five streams are defined, containing Bhabha scattering events, ϕ decays into charged kaons, ϕ decays into neutral kaons, $\phi \to \pi^+\pi^-\pi^0$ and radiative ϕ decays, and for each of them a different file is created. Apart from the Bhabha stream, a further reduction is done for each stream, keeping only the information needed for the physical analysis. The resulting set of data-summary tapes (DSTs) is six times smaller in size than the corresponding reconstruction output files and can be kept on disk for an easy access.

2.3.2 Clustering

A cell is defined as the smallest 'part' of calorimeter seen by two photomultipliers at its ends. The photomultiplier outputs are preamplified and sent with a delay of 220 ns (the time necessary to the trigger do decide whether to start the acquisition or not) to ADC's and to the TDC's. Let's label the two ends of a cell as A and B: for each cell two time signals $t^{A,B}$ and two amplitude signals $S^{A,B}$ are recorded from the corresponding photomultiplier outputs. The position of the energy release along the fiber direction is obtained from the time difference $t^A - t^B$. If $T^{A,B}$ are the counts in the TDC's, the time at the ends of the cell will be $t^{A,B} = c^{A,B} \times T^{A,B}$, where $c^{A,B}$ (in ns/counts) are the TDC's calibration constants. The particle time arrival t and the position along the fiber direction is (the zero is taken at the fiber center):

$$t\,(ns) = \frac{t^A + t^B}{2} - \frac{t_0^A + t_0^B}{2} - \frac{L}{2v} - t_0^G \tag{2.1}$$

$$s\,(cm) = \frac{v}{2}(t^A - t^B - t_0^A + t_0^B) \tag{2.2}$$

with L and v the cell length (in cm) and the light velocity (in cm/s) in the fiber, $t_0^{A,B}$ are overall time offset and t_0^G is the event global time offset. The two coordinates orthogonal to the fiber direction are given by the center of the cells according to the measured geometry. The constants c^A and c^B of every TDC channels (4880) have been measured in some preliminary test (as well as the length L of the cells), before the installation of the experiment. They provide the conversion from TDC counts to ns (average value is 53 ps/counts).

The need to measure the global time of the event t_0^G comes from the fact that the time spread of the event (which can reach 30÷40 ns for $K_S K_L$ events) is bigger than the time

interval between two consecutive bunch crossing. The DAΦNE machine clock has a period T_{RF} of 2.7 ns and the time between one bunch crossing and the next is n×2.7 ns, with n depending on the bunch filling in the machine. The event reconstruction has to find the true bunch crossing for each event, then it is subtracted event by event. This procedure takes into account several effects: the time of flight of the particles, the delay between trigger and calorimeter due to electronics and cables and the fact that the trigger signal is synchronized with the DAΦNE radio frequency. In order to determine t_0^G a calibration of the delay and of T_{RF} is performed using $\gamma\gamma$ events, which provide the easiest time signature. The expected time of such a sample is given by R/c, where R is calculated assuming a neutral particle coming from the interaction point and c is the light speed. From the residual difference from the measured time t and expected time of flight R/c, the delay due to cables and electronics and the synchronization RF are simultaneously measured. The time between peaks in fig. 2.10 is the inter-bunch and it is a multiple of RF period. The delay is obtained by selecting one peak; any peak is in principle equivalent as a reference time. The energy signal E on

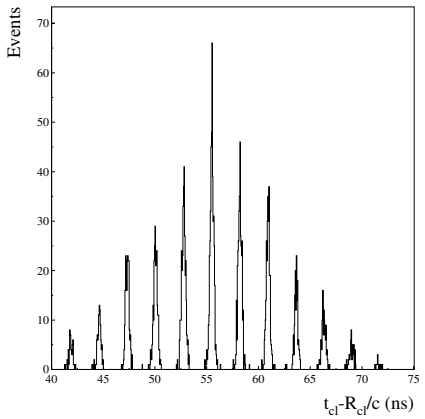

Figure 2.10: t-R/c distribution for $\gamma\gamma$ events before any corrections.

each side of the cell is obtained from the counts S in the ADC's:

$$E^{A,B}\,(MeV) = \frac{S^{A,B} - S_0^{A,B}}{S_M} \times \kappa_E \tag{2.3}$$

where $S_0^{A,B}$ are the zero offsets of the amplitude scale, S_M is the signal for a minimum ionizing particle crossing the calorimeter center and κ_E is the energy scale factor (in MeV/counts). The energy zero off-sets $S_0^{A,B}$ are obtained from cosmic ray runs without circulating beam, i.e. with very low occupancy of the detector. In the S_M factor, the response of the photomultipliers, the fiber light yield and the electronic gain is considered. Cosmic rays are used to measure also this quantity: during a typical cosmic ray run (18 hours of data taking), ∼1000 events per cell are collected. The mean values of the gaussian used to fit the amplitude spectra are by definition the S_M (for each cell) which enter in

eq. 2.3. Finally, in order to be independent from the position, a correction factor $A^{A,B}(s)$, due to the attenuation along the fiber length, is applied, and the energy of the cell becomes:

$$E\,(MeV) = (E^A \cdot A^A + E^B \cdot A^B)/2 \tag{2.4}$$

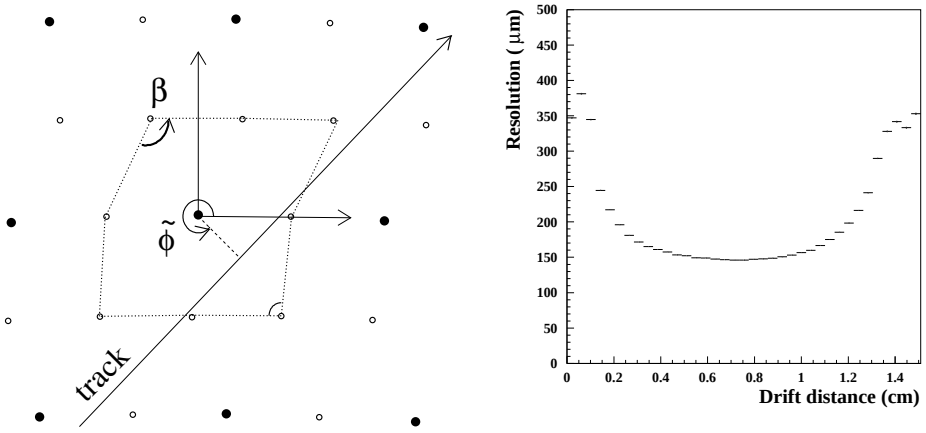

(a) (b)

Figure 2.11: (a) Definition of the variables used in the $s-t$ relations classification. (b) Spatial resolution as a function of drift distance over all big cells for a single $\tilde{\phi}$ value.

The first step in the event reconstruction is the processing of the calorimeter information. Once the cells have been reconstructed, the *clustering algorithm* merges together groups of adjacent cells. A cell becomes part of the cluster if times and amplitudes are available from both sides of the fiber. If one of these four information is missing (*incomplete* cell), the cell belonging to the barrel is recovered on the basis of the difference $\Delta\phi$ between its azimuth and that of the closest cluster. Incomplete cells are assigned to a cluster if $|\Delta\phi| < 3°$. An analogous procedure is repeated in the two endcaps using the z-coordinate. The cluster energy E_{cl} is simply the sum of the energies of the cells making the cluster, while the cluster positions and time (x_{cl}, y_{cl}, z_{cl} and t_{cl}) are computed as energy-weighted averages of the cell variables.

2.3.3 Tracking

Due to the large cell dimensions and to the variation of the electric field along the wires, the drift velocity is not saturated. These effects produce space-time (s-t in the following) relations dependent upon the spatial coordinates of the cell and on the incidence direction of the track in the cell. The s-t relation has been parametrised according to the two variables β and $\tilde{\phi}$ defined in fig. 2.11(a). Six cells with β varying between 65° and 125° are chosen as reference cells. In each of these cells the $\tilde{\phi}$ angle is divided into 36 intervals of 10°. Since only

the upper part of the cell is deformed by the stereo geometry, in 20 bins of $\tilde{\phi}$ corresponding to the lower part, the s-t relation is the same for all the six reference cells. This results in a total of 16×6+20=116 parametrisation (to be doubled once one considers both small and big cells). In the single cell, the drift distance is related to the drift time in terms of a 5^{th} order Chebychev polynomial $t_{drift} = P(C_i^k, d)$, where t_{drift} is the measured time, d is the impact parameter and the 6×232 coefficients C_i^k (k=1,...,232 and i=1,...,t) account for the cell type, track orientation and cell shape, as described above. An automatic calibration procedure checks the validity of the current s-t relations at the beginning of each run and calculate new C_i^k using cosmic ray events, if necessary. For more details see [68].

The event reconstruction in the drift chamber starts with the Pattern Recognition. It searches for candidate tracks, firstly in the xy plane, then looks for the projection in the z plane. Due to the stereo setting of the wires, a track in the chamber is seen as two distinct curves. In each stereo views, hits close in the space are associated to form a chain, on the basis of their curvature, and the left-right ambiguity is solved requiring the single-view candidate track to have a minimum of four hits in at least two layers. At this stage the magnetic field is assumed to be homogeneous, multiple scattering and energy loss are not treated, and rough s-t relations are used. The track fitting minimises iteratively a χ^2 function based on the comparison between the measured (as obtained by the s-t relations) and expected (from the fit) drift distance for each hit (see fig. 2.11(b)). The drift distance is corrected using more accurate s-t relations which depend on the track parameters and all the effects neglected in the pattern recognition (local variation of the magnetic filed, multiple scattering and energy loss) are now taken into account. After a first iteration, dedicated procedures recover missed hits or wrongly assigned by the pattern recognition, merge splitted tracks and split kinked tracks. The tracks from the fitting procedures are then used to look for primary and secondary vertices. In order to reduce the number of combinations, the tracks are firstly extrapolated in the $x - y$ plane and primary vertices are searched for using tracks whose impact parameter is smaller that 10% than their radius of curvature. The remaining tracks are then connected with secondary vertices. For tracks crossing the beam-pipe or the walls of the chamber, the momentum is corrected for energy loss and multiple scattering.The minimization of a χ^2 function based on the distance of the closest approach between tracks is used to assign the two tracks to a vertex. For a vertex inside the beam-pipe the spatial resolution is about 2 mm. For each track pair, a χ^2 function is evaluated from the distances of closest approach between tracks. For more details on the vertex fitting procedure see [69].

Chapter 3

Motivation for the Large angle analysis

A first measurement of the hadronic cross section $\sigma(e^+e^- \to \pi^+\pi^-)$ has been performed using data collected by the KLOE detector in 2001. A complementary analysis with the data collected in 2002 in a different phase space is presented in this thesis.
In the present chapter a short description of the already published analysis is given, together with the motivations for the second analysis, as well as the main differences between the two of them.

3.1 The *radiative return* method

The standard way for measuring the hadronic cross section is to perform an energy scan, in which the collision energy of the machine is changed and the desired measurement is done point-by-point. The DAΦNE collider has been designed as a meson-factory operating at the ϕ mass (1019.4 MeV), and the variation of the center-of-mass was not foreseen. As an alternative, the idea has been worked out to obtain $\sigma(e^+e^- \to \text{hadrons})$ using the radiative process $e^+e^- \to \text{hadrons}+\gamma$, where the photon is radiated by the initial electron or positron (see fig. 3.1(a)), lowering the center-of-mass of the hadronic system [70]. The cross section $\sigma(e^+e^- \to \pi^+\pi^-\gamma)$ is thus measured as a function of the two pion invariant mass squared s_π in the allowed energy range, from the threshold $4m_\pi^2$ to m_ϕ^2. The possibility to measure the hadronic cross section using the *radiative return* method relies on the assumption that the radiative photon does not interfere with the final state process. In this case the initial state $e^+e^-\gamma$ and the hadron production factorize and the cross section $\sigma(e^+e^- \to \pi^+\pi^-)$ can be expressed as a function of the differential cross section $\sigma(e^+e^- \to \pi^+\pi^-\gamma)/ds_\pi$:

$$s_\pi \frac{d\sigma(e^+e^- \to \pi^+\pi^-\gamma)}{ds_\pi} = H(s_\pi) \cdot \sigma(e^+e^- \to \pi^+\pi^-) \tag{3.1}$$

where an accuracy better than 1% is necessary for the radiator function $H(s_\pi)$. Under the condition of factorization and only one photon radiated, s_π equals the hadronic invariant

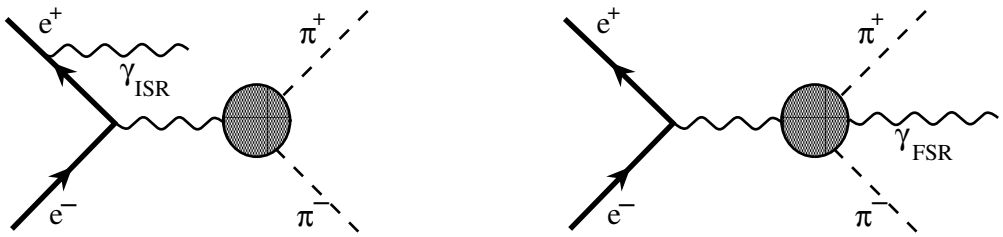

(a) (b)

Figure 3.1: Leading order contribution to ISR (a) and to FSR (b) process.

mass and the following relation holds:

$$s_\pi = Q^2_{\pi^+\pi^-} = m^2_\phi - 2E_\gamma \tag{3.2}$$

For the evaluation of $H(s_\pi)$ the MonteCarlo generator PHOKHARA ([71][62][63]) has been used. It includes hard, soft and virtual radiative corrections to the process $e^+e^- \to \pi^+\pi^-\gamma$ at next-to-leading order and also final state radiation from the pions described according the scalar QED (i.e. treating pions as point-like particles).
eq.řefeq:masterformula is not valid anymore if the radiated photon couples to the pion as shown in fig. 3.1(b). A wrong energy value would be in this case associated to the two-pion system, since the $\pi^+\pi^-$ pair is produced at $\sqrt{s} = m_\phi$ and the energy is then reduced by Final State Radiation (FSR). Therefore this kind of process represents a background for the analysis and it needs to be reduced as much as possible.
The systematic errors for a measurement with the *radiative return* method are different compared with the ones from an energy scan measurement, making this method complementary to the energy scan. In the case of the *radiative return* the normalization parameters (as luminosity, energy of the machine) have to be determined only once and are the same for each point of the spectrum, while for an energy scan they have to be measured for each energy point separately. Moreover the *radiative return* method does not need dedicated machine time, it can be performed in parallel with the standard physics program. On the other hand the FSR contribution has to be well suppressed, if possible, or precisely understood otherwise, in order to be subtracted from the data. Precise theoretical calculations of the radiator function H are necessary as well, since the uncertainty of this quantity enters directly the error of the $\pi^+\pi^-$ cross section.

Finally the cross section $e^+e^- \to \pi^+\pi^-\gamma$ is suppressed by a factor α/π with respect to the cross section $e^+e^- \to \pi^+\pi^-$; therefore a larger integrated luminosity is necessary to reach the same level of accuracy. This is not a problem at a modern meson-factory, all working at high luminosity.

3.2 The *small angle* analysis

As mentioned above, the FSR events are simulated in PHOKHARA according to the model of scalar QED (sQED); the model dependence makes it unavoidable to reduce this contribution as much as possible. Final state radiation cannot be distinguished from ISR experimentally, but can be significantly reduced by choosing appropriate angular cuts. In the 2001 data analysis [11] cuts have been applied to select photons in the forward-backward region, i.e. being these emitted preferentially along the beam direction to enhance the ISR contribution. The preferred emission direction of the photons both from ISR and FSR are displayed in fig. 3.2(a) and in fig. 3.2(b) where the distribution of the cosine of the minimum angle between the photon and one of the two pions in the two pion rest frame is plotted, for the case of ISR and FSR respectively. The ISR photons tend to be emitted in the orthogonal direction of the pions ($cos(\theta_{\gamma\pi})$ peaked at 0); the pions go preferentially toward the central plane of the detector. This means that γ_{ISR} tend to be emitted along the beam pipe. The opposite occurs for γ_{FSR}, whose angle with respect the pions is peaked at zero. γ_{FSR} tend to follow the same direction of the pions, which they have been emitted from, namely at large polar angles. Detecting pions at large polar angles and photons at small polar angles, corresponds then to minimize the relative amount of FSR.
The explicit detection of the photon is not required, thus the measurement is performed without photon *tagging*. If the event consists of two pions and only one photon, the polar angle of the photon equals the angle of the missing momentum of the event: $\theta_\gamma = 180^o - \theta_{miss}$, where the missing momentum is $\vec{p}_{miss} = \vec{p}_{\pi^+} + \vec{p}_{\pi^-}$. We have requested θ_{miss} <15^o or θ_{miss} >165^o, while the pions are detected with $50^o < \theta_\pi$ <130^o . This phase space excludes the very low $M_{\pi\pi}$ region, i.e. $M^2_{\pi\pi}$ <0.3 GeV^2, because at small $M_{\pi\pi}$ (high photon energy) the di-pion system recoiling against the small angle photon results in one or both pions to be emitted at small angles, and thus the event is not accepted.
In the following with *small angle* we mean the following cuts:

- $50^o < \theta_{\pi^\pm} < 130^o$
- $15^o < \theta_\gamma$ or $\theta_\gamma > 165^o$

In order to reject the huge Bhabha events contamination (whose cross section is >500 nb to be compared with ∼9 nb for the cross section of $\pi^+\pi^-\gamma$ events within the *small angle* acceptance) a particle ID method based on a likelihood estimator is used. It uses the following information:

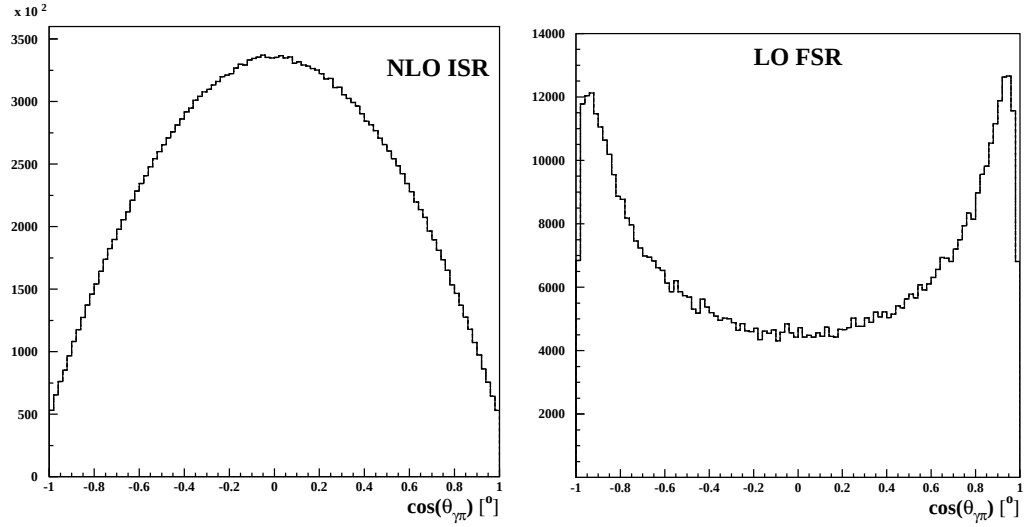

(a) (b)

Figure 3.2: Distribution of the minimum angle between the photon and one of the two pions, in the pion rest frame, for ISR (a) and FSR photons (b).

- the total energy of the cluster and the maximum energy release among the five planes of the calorimeter;
- the energy release in the first and in the last fired calorimeter plane;
- the difference $(t - L/c)$, with t the time of the cluster, l the track length from the interaction point to the centroid of the cluster, c the speed of light.

Each of the just mentioned variables allows to define two probability densities, by fitting the corresponding distributions. Two absolute likelihood estimators are defined as:

$$\begin{aligned} a\,\mathcal{L}(\{x_i\}) &= \prod_i f_i^{\pi}(x_i) \\ a\,\mathcal{L}(\{x_i\}) &= \prod_i f_i^{e}(x_i) \end{aligned} \tag{3.3}$$

where x_i $(i = 1, .., 5)$ are the variables listed above and $\{f_i^{\pi}(x_i)\}$,$\{f_i^{e}(x_i)\}$ are the set of fit function for the control samples of the pion and of the electron tracks respectively.
The two functions $a\,\mathcal{L}^e$ and $a\,\mathcal{L}^{\pi}$ express the probability for the particle to be a pion or an electron.
Details about the particle ID estimator can be found in [72] and [73].
The background from $\phi \to \pi^+\pi^-\pi^0$ is strongly reduced by the acceptance cut. The residual of this kind of process and muon pair events from $e^+e^- \to \mu^+\mu^-\gamma$ are rejected by a cut on the kinematical variable called trackmass, m_{trk}. This latter is obtained by imposing the 4-momentum conservation on events made by two charged particles with the same mass

and one photon, via the relation

$$(m_\phi - \sqrt{|\vec{p}_+|^2 + m_{trk}} - \sqrt{|\vec{p}_-|^2 + m_{trk}})^2 - |\vec{p}_+ + \vec{p}_-|^2 = 0 \tag{3.4}$$

For $e^+e^- \to x^+x^-\gamma$ events, the value of m_{trk} peaks at m_π, m_μ for $x = \pi$, μ, as shown in fig. 3.3(a).

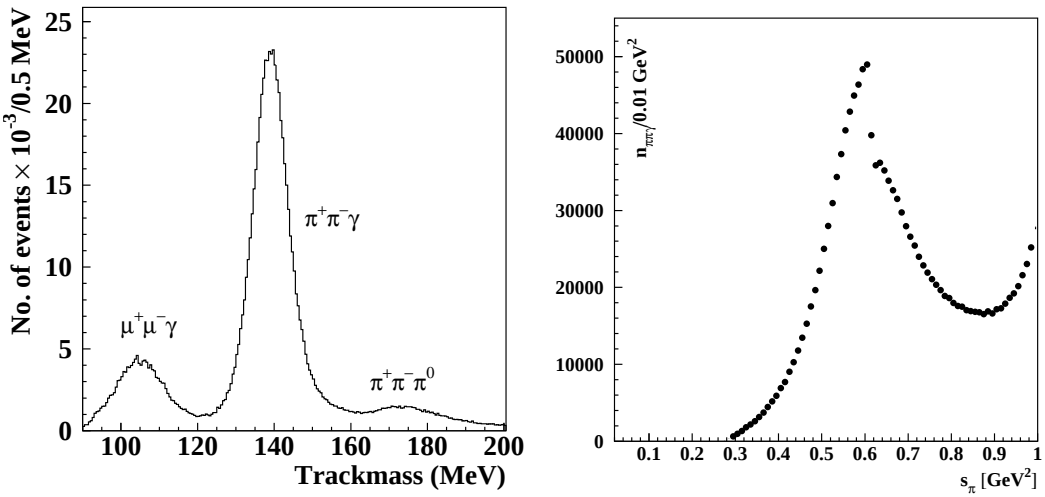

(a) (b)

Figure 3.3: (a) Trackmass distribution for $\mu^+\mu^-\gamma$, $\pi^+\pi^-\pi^0$ and $\pi^+\pi^-\gamma$, after requiring ID as pion for at least one of the two tracks. The particle ID does not effect the $\mu^+\mu^-\gamma$ region. (b) Distribution of $e^+e^- \to \pi^+\pi^-\gamma$ in bins of 0.01 GeV^2 after applying the acceptance and the selection cuts of the *small angle* analysis.

The selection has been applied to the 141 pb^{-1} data sample collected in 2001 [11], obtaining the distribution of events presented in fig. 3.3(b). Due to the high momentum resolution of the drift chamber, the $\rho - \omega$ interference is clearly visible, even before any unfolding procedure. The kinematic suppression of the threshold region is evident as well. In order to obtain the differential cross section $\sigma(e^+e^- \to \pi^+\pi^-\gamma)$ from the spectrum of fig. 3.3(b) one has to subtract the residual background from the sample, to normalize it to the integrated luminosity and finally to correct it for the selection efficiency and the acceptance, according to:

$$\frac{d\sigma_{\pi\pi\gamma}}{dM_{\pi\pi}} = \frac{\Delta N_{Obs} - \Delta N_{Bkg}}{\Delta M_{\pi\pi}} \cdot \frac{1}{\int \mathcal{L}} \cdot \frac{1}{\epsilon_{Sel}\epsilon_{Acc}} \tag{3.5}$$

3.2.1 Residual background subtraction

For the evaluation of the remaining $e^+e^-\gamma$ and $\mu^+\mu^-\gamma$ events the trackmass distributions in slices of $M_{\pi\pi}$ for signal and background have been fitted. From the fitted normalization parameters, one obtains the amount of the single background channel.

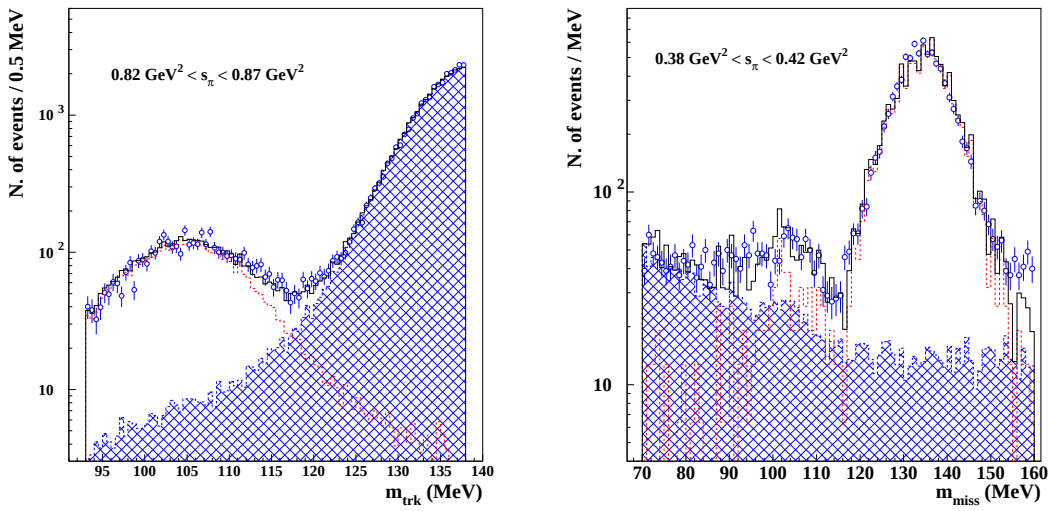

(a) (b)

Figure 3.4: (a) Trackmass distribution in one slice of $M_{\pi\pi}$ for data (points), $\mu^+\mu^-\gamma$ MonteCarlo simulation (dashed line), $\pi^+\pi^-\gamma$ MonteCarlo simulation (hatched area) and the sum of the two MonteCarlo distributions (solid line) after the fitting procedure to estimate the $\mu^+\mu^-\gamma$ contribution. (b) Missing mass distribution in one slice of $M_{\pi\pi}$ for data (points), $\pi^+\pi^-\pi^0$ MonteCarlo simulation (dashed line), $\pi^+\pi^-\gamma$ MonteCarlo simulation (hatched area) and the sum of the two MonteCarlo distributions (solid line) after the fit procedure to estimate the $\pi^+\pi^-\pi^0$ contribution.

For Bhabha events a control sample of $\sim$120 pb^{-1} has been selected according to the analysis selection cuts, however requesting 93 MeV$< m_{trk} <$138 MeV, leaving out the $\pi^+\pi^-\gamma$ peak. Additionally it is required for the same sample that one and only one track is recognised as a pion by the particle ID, in order to increase the sensitivity to Bhabha events. By fitting the trackmass distribution obtained from this data sample with the ones from $e^+e^-\gamma$, $\mu^+\mu^-\gamma$ and $\pi^+\pi^-\gamma$ MonteCarlo, one obtains the absolute $e^+e^-\gamma$ contamination. Subtracting the Bhabha contribution from the data sample, one remains with the hypothesis that within the restriction 93 MeV$< m_{trk} <$138 MeV, the only background comes from muons. By fitting again the trackmass distribution of data (selected with the same selection cuts used for the previous control sample, with the only difference that now at least one particle has to be identified as a pion by the particle ID) with $\mu^+\mu^-\gamma$ MonteCarlo ones, gives us the absolute $\mu^+\mu^-\gamma$ contamination.

The amount of $\pi^+\pi^-\pi^0$ events is obtained with the same procedure, but fitting the missing mass, defined as $m_{miss} = |P_\phi - P_{\pi^+} - P_{\pi^-}|^2$, where $P_{\pi^\pm}$ are the 4-momentum for the charged particles and P_ϕ is the one due to the boost. The variable m_{miss} peaks at m_{π^0} for the three pion final state, differently to the trackmass which has not a peaked structure

for these kind of events (not being made of two charged particles and one photon). The fit has been performed in slices of $M_{\pi\pi}$ in the interval $70 < m_{miss} < 160$ MeV, superimposing data distributions with $\pi^+\pi^-\pi^0$ and $\pi^+\pi^-\gamma$ MonteCarlo, since the $\mu^+\mu^-\gamma$ contribution is negligible in this region. The fig. 3.4(a) and fig. 3.4(b) show two examples of the fit procedure, for muons and $\pi^+\pi^-\pi^0$ respectively. The shapes of the trackmass and of the

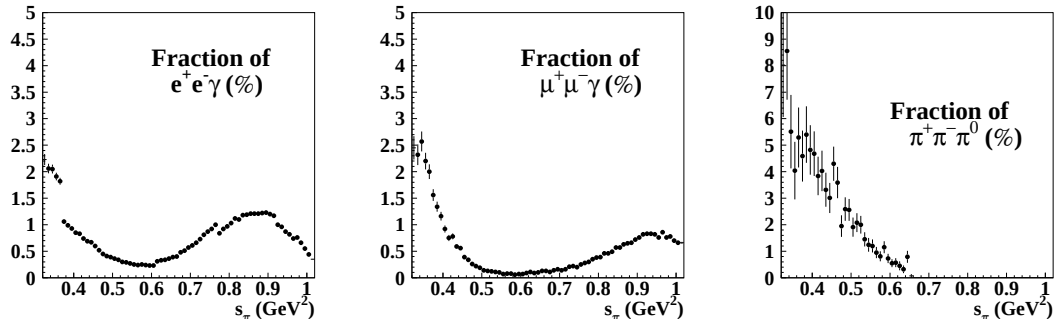

(a) (b) (c)

Figure 3.5: Fraction of $e^+e^-\gamma$ (a), $\mu^+\mu^-\gamma$ (b) and $\pi^+\pi^-\pi^0$ (c) background as a function of the invariant mass squared of the two pions.

missing mass are well reproduced by MonteCarlo, therefore the errors from the fit procedure have been taken as the systematic error for the background evaluation. In fig. 3.5 the fraction of $e^+e^-\gamma$, $\mu^+\mu^-\gamma$ and $\pi^+\pi^-\pi^0$ background as a function of the invariant mass squared of the pions is shown. The total background contamination is smaller then 2% above 0.5 GeV^2 and grows up to 10% at low masses.

3.2.2 Extraction of the pion form factor

A big effort has been spent to evaluate the radiative corrections. In the selected sample both leading-order (FSR-LO) and next-to-leading-order final state radiation (FSR-NLO) are present. In the first case a single photon is emitted by one of the two pions in the final state, as in fig. 3.1(b), and the invariant mass of the virtual photon is not lowered with respect to the center-of-mass energy of the machine. Since the goal of the measurement is to determine the cross section below m_ϕ, this process has to be considered as background, due to the fact that these events originate from a value of $M_{\pi\pi}$ out of the range under study. The acceptance and the trackmass cut reduce the FSR-LO contribution; the residual contamination is estimated from MonteCarlo (PHOKHARA) and subtracted from the spectrum.
Different is the case for FSR-NLO, in which a photon in the initial state and one in the final state are simultaneously emitted, lowering the invariant mass of the intermediate virtual photon. Events of this kind have to be included in the cross section to be put in the dispersion integral. However, as in the case of FSR-LO, the energy of the hadronic system is

lower than the momentum transfer, and this effect has to be corrected for in the differential cross section. An *unshifting* function which corrects for the difference between $\frac{d\sigma_{\pi\pi\gamma}}{dM_{\pi\pi}}$ and $\frac{d\sigma\pi\pi\gamma}{ds^*_\gamma}$ (where s^*_γ is the invariant mass of the virtual photon) has been built from a special version of PHOKHARA, in which ISR- and FSR-photons can be distinguished. Using eq.r̃efeq:masterformula one passes from the event spectrum of fig. 3.3(b) to the differential cross section $d\sigma_{\pi\pi\gamma}/M^2_{\pi\pi}$ as a function of $M^2_{\pi\pi}$.

Applying the efficiencies and acceptance corrections, the *unshifting* function and finally dividing by the radiator function, one obtains the physical cross section.

The efficiencies of the cuts entering the event selection and their systematic error are evaluated individually. Except for the trackmass cut and for the acceptance, all the other have been studied directly from data control samples. The combined total efficiency is almost flat and around 60%. In tab. 3.1 the systematics errors associated to the individual efficiencyies are reported. A detailed description of the evaluation of each of them can be found in [74].

Acceptance	0.3 %
Trigger	0.3 %
Reconstruction Filter	0.6 %
Tracking	0.3 %
Vertex	0.3 %
Particle ID	0.1 %
Trackmass	0.2 %
Background subtraction	0.3 %
Unfolding	0.2 %
Total experimental systematics	0.9 %

Table 3.1: List of experimental systematic errors in the *small angle* analysis.

The radiator function is obtained from PHOKHARA as $d\sigma^{\pi\pi\gamma}(F_\pi = 1)/dM^2_{\pi\pi}$, i.e. the NLO cross section for $e^+e^- \to \pi^+\pi^-\gamma$ with initial state radiation only. The extracted cross section $\sigma(e^+e^- \to \pi^+\pi^-)$ is presented in fig. 3.6(a) as a function of the invariant mass of the intermediate photon s_{γ^*}: it covers the full angular range in θ_π and θ_{miss} and includes final state radiation and vacuum polarization (*dressed* cross section).

The cross section to be put into the dispersion integral has to be corrected for the vacuum polarization of the intermediate photon [59]. This correction is applied to arrive at the pion form factor, and the final state radiation is removed as well. The obtained pion form factor is shown in the plot of fig. 3.6(b)

The cross section $\sigma(\pi^+\pi^-\gamma_{FSR})$, including FSR contribution and corrected for the vacuum polarization, has been used to evaluate the contribution to a_μ from the $\pi^+\pi^-$ channel in the energy range $0.35 < M^2_{\pi\pi} < 0.95$ GeV^2.

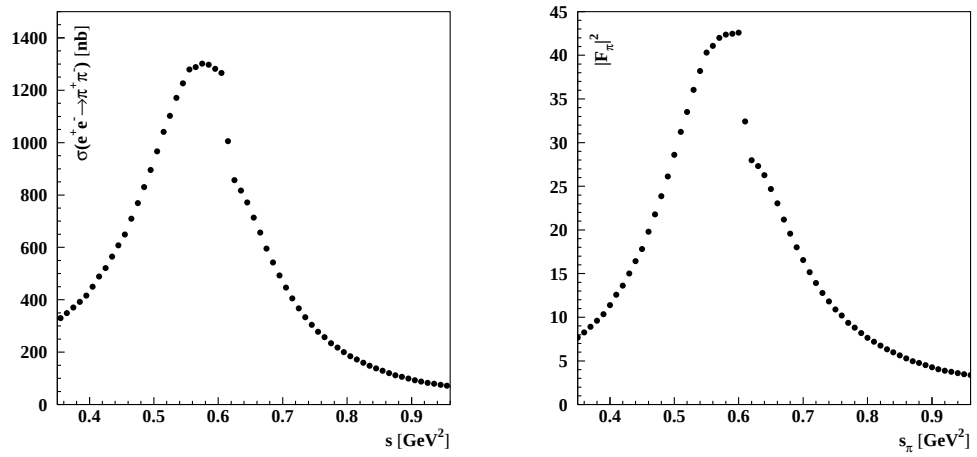

(a) (b)

Figure 3.6: (a) *Dressed* hadronic cross section $\sigma(e^+e^- \to \pi^+\pi^-)$.(b) Pion form factor.

The resulting value is:

$$a_\mu^{\pi\pi}(0.35 - 0.95) = (388.7 \pm 0.8_{stat} \pm 3.5_{syst} \pm 3.5_{th}) \times 10^{-10} \tag{3.6}$$

The statistical error of the measurement is negligible and the error from theory [1] is as big as the experimental one. Thus, an improvement of the determination of $a_\mu^{\pi\pi}$ requires not only a better evaluation of the experimental systematic effects, but also a better knowledge of the theoretical inputs that enter the analysis. For a more detailed discussion on this topic, we refer to the last chapter of this thesis.

3.3 Large angle analysis: the fiducial volume

Besides the analysis presented above, KLOE has performed a complementary determination of the cross section $e^+e^- \to \pi^+\pi^-\gamma$ in a different angular region. This is the main subject of the present thesis. Moving from small to large photon polar angles, also the threshold region $4m_\pi^2 < M_{\pi\pi}^2 < 0.35$ GeV^2 becomes accessible, which was kinematically suppressed at small photon angles. This is shown in fig. 3.7(a), where the spectrum from a MonteCarlo simulation both for $\theta_{miss} < 15^o (> 165^o)$ and $50^o < \theta_{miss} < 130^o$ is presented. While the spectrum towards low $M_{\pi\pi}$ decreases rapidly for $\theta_{miss} < 15^o (> 165^o)$, at large photon polar angles it extends down to the 2π threshold. It is important to underline that this region is measured by only a few experiments and with a precision much worse than the ρ-peak

[1] The total theoretical error comes from different sources: the error claimed for the BABAYAGA generator used in the luminosity measurement, the error of the radiator function, the error of the FSR subtraction and finally the error of the vacuum polarization correction.

region. An improvement is of importance since below $M^2_{\pi\pi}$ <0.5 GeV^2 the channel $\pi^+\pi^-$ adds $\sim 60 \cdot 10^{-10}$ to the value of a_μ.
The most precise and most recent measurement at threshold is from the SND collaboration [8], which has covered the mass range down to $M_{\pi\pi}$ =390 MeV with a systematic error of 3.4% for $M_{\pi\pi}$ <420 MeV and 1.3% for $M_{\pi\pi}$ >420 MeV.
While at large photon angle also the background from $e^+e^-\gamma$ and $\mu^+\mu^-\gamma$ events is reduced

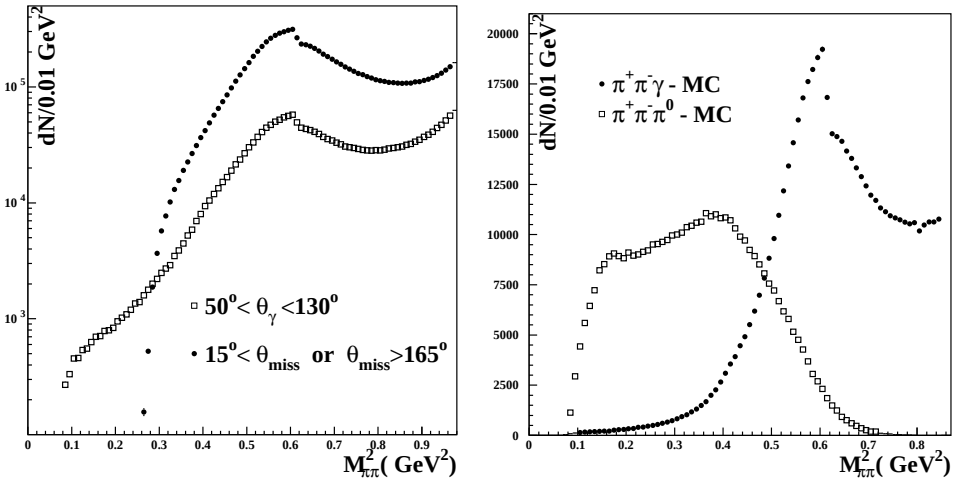

(a) (b)

Figure 3.7: (a) MonteCarlo spectra of the number of $\pi^+\pi^-\gamma$ events for different angular cuts. Both plots correspond to an integrated luminosity of ∼800 pb^{-1} (b) Event distribution after the acceptance cut, $50^o < \theta_{\pi,\gamma} < 130^o$ for MonteCarlo samples of $\pi^+\pi^-\gamma$ and $\pi^+\pi^-\pi^0$, normalized to the integrated luminosity of the 2002 data (∼240 pb^{-1}).

by the requirement for the photon to be between 50^o and 130^o (see fig. 3.8 where the photon polar angle distribution is shown for $\mu^+\mu^-\gamma$ and Bhabha events), this is not the case for the channel $\phi \to \pi^+\pi^-\pi^0$, since the direction of the π^0 is preferably at central values. It populates heavily the region at low $M_{\pi\pi}$, as shown in fig. 3.7(b), where the mass spectrum is plotted for the acceptance region $50^o < \theta_{\pi,\gamma} < 130^o$ for two Monte-Carlo samples of $\pi^+\pi^-\gamma$ and $\pi^+\pi^-\pi^0$. As one can see, the signal-to-background ratio is very low for low $M_{\pi\pi}$ values, illustrating the need for further dedicated cuts. Crucial in this analysis is the detection of the photon (*tagged* analysis), which was not possible in the *small angle* analysis. At large photon polar angles the presence of a π^0 can be established by the two decay photons and building their invariant mass (see §4.2.1 and §4.2.3). A set of cuts constructed by closing the kinematics, allows to suppress almost completely the $\pi^+\pi^-\pi^0$ background (see §4.2).
However the cuts applied do not help to reduce the *irreducible* one, having this latter exactly the same signature as the signal. There are three sources of *irreducible* background at large photon angle:

- the resonant ϕ decay: $\phi \to \rho\pi \to \pi^+\pi^-\gamma$;

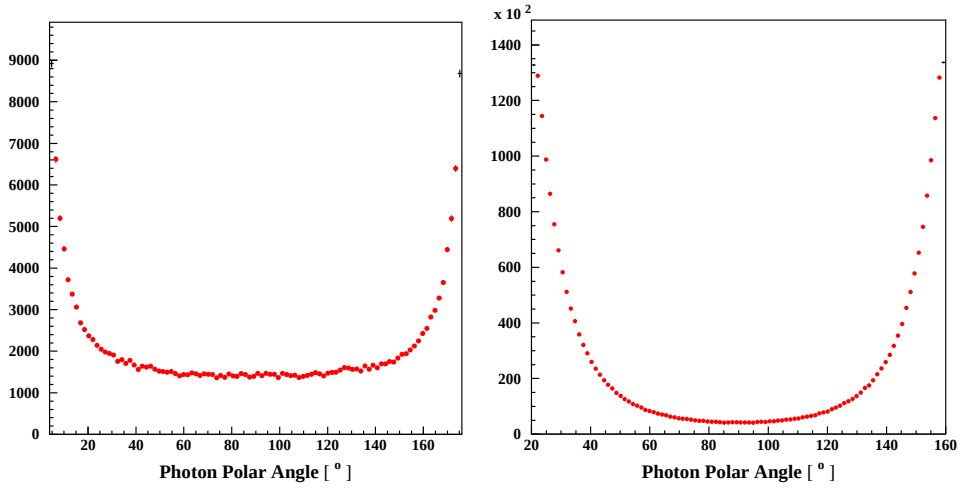

(a) (b)

Figure 3.8: Photon polar angle distribution for $\mu^+\mu^-\gamma$ events in (a) and radiative Bhabha events in (b). Both distributions are obtained from MonteCarlo, PHOKHARA for the muons and NLO-Babayaga for Bhabha events [75].

- Leading-Order Final State Radiation (FSR-LO) where a photon is emitted by one of the pions;
- the radiative ϕ decay to $\pi^+\pi^-\gamma$ through a scalar meson: $\phi \to (f_0(980) + f_0(600))\gamma \to \pi^+\pi^-\gamma$.

A sketch of the three physical processes is given in fig. 3.9.

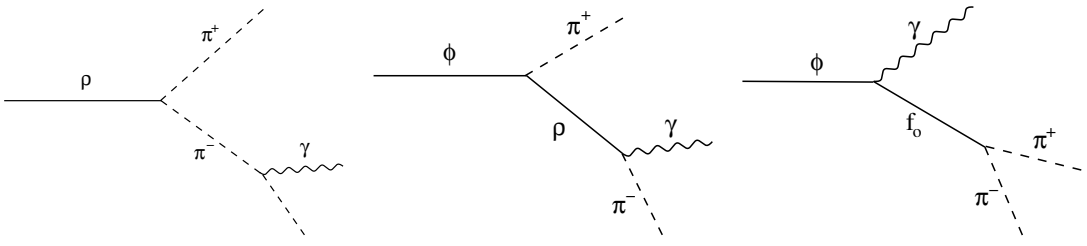

(a) (b) (c)

Figure 3.9: The three sources of *irreducible* background at large photon angle: in (a) Leading-Order Final State Radiation where a photon is emitted from one of the two pions in the final state, in (b) the decay $\phi \to \rho\pi \to \pi^+\pi^-\gamma$ and in (c) the radiative ϕ decay to $\pi^+\pi^-\gamma$ through a scalar meson: $\phi \to (f_0(980) + f_0(600))\gamma \to \pi^+\pi^-\gamma$

Another complication arises from the fact that one needs to know not only the contribution of each individual channel, but also the interference effects.
The first of the three processes listed above is neglected in the analysis. In fact in ref.[64]

the contribution of $\phi \to \rho\pi \to \pi^+\pi^-\gamma$ is not considered, since KLOE has found it to be negligible in the $\phi \to \pi^0\pi^0\gamma$ analysis [76]. The branching ratio $BR(\rho^\pm \to \pi^\pm\gamma)$ and $BR(\rho^0 \to \pi^0\gamma)$ are comparable, hence the same conclusion applies to $\pi^+\pi^-\gamma$ final state. MonteCarlo simulations support this ansatz for $M^2_{\pi\pi}$ >0.5 GeV^2.
The other two processes, the radiative decay $\phi \to S\gamma$ where S is a scalar meson ($f_0(980)$ or $f_0(600)$) with mass below 1 GeV decaying into $\pi^+\pi^-$ and the $e^+e^- \to \pi^+\pi^-\gamma_{FSR}$ (FSR-LO) background are the subjects of §3.3.1 and §3.3.2 respectively.

3.3.1 The scalar mesons contribution

The scalar mesons in this region are the well established $f_0(980)$ and the more controversial $f_0(600)$, called also σ. The radiative decay proceeds with a photon angular distribution $f(\theta) \sim (1 + cos^2(\theta))$ so that its effect is more relevant in the large angle (LA) region rather than in the small angle (SA) one ($\int_{SA} f(\theta)d\Omega / \int_{LA} f(\theta)d\Omega \sim 0.08$). The prediction of the amount of these events is not straightforward, since the properties of these scalar are not completely known, but also because the amplitude of this process gives rise to an interference pattern with FSR that cannot be simply removed by subtraction.
KLOE has recently analyzed the $\pi^+\pi^-\gamma$ final state at large photon polar angle ($45^o < \theta_{\pi,\gamma} < 135^o$) in the 2001-2002 data sample (∼350 pb^{-1}) to evaluate the properties of the scalar mesons. The analysis is described in [77]. Parametrizing the $f_0(980)$ with the so called kaon loop amplitude ([78]), one can reproduce well the data shape between 400 and 1000 MeV(see fig. 3.10). In the kaon loop model the ϕ couples to the scalar through a loop of charged kaons. The formalism allows to include more than one scalar meson. For each scalar meson there are three free fit parameters: the mass and the two couplings to K^+K^- and to $\pi^+\pi^-$. For the scalar meson $f_0(980)$, the kaon-loop amplitude reduces to:

$$A_{KL} = g(m^2)e^{i\delta(m)}\frac{g_{f_0K^+K^-}g_{f_0\pi^+\pi^-}}{(s-m^2)D_{f_0}(m)} \tag{3.7}$$

where s is the invariant mass of the center-of-mass energy, $g_{f_0K^+K^-}$ and $g_{f_0\pi^+\pi^-}$ are the two couplings parameters, $g(m^2)$ is the kaon-loop function ([78]), $\delta(m)$ is the phase relative to $\pi\pi$ scattering and D_{f_0} is the f_0 inverse propagator. The coupling parameters are found by fitting the $\pi^+\pi^-$ invariant mass distribution. The interference between the scalar meson amplitude and the final state radiation amplitude turns out to be destructive. The $f_0(980)$ signal appears as a bump at around 980 MeV in the $\pi^+\pi^-$ invariant mass $M_{\pi\pi}$ spectrum of fig. 3.10.
The decay $\phi \to f_0(980)\gamma$ features a specific E^3_γ behaviour, which leads to the observation that the mass spectrum is not only concentrated around its mass, but it extends down to the 2π threshold. Several models have been proposed to parametrize the dynamics of the decay $\phi \to (f_0(980) + f_0(600))\gamma \to \pi^+\pi^-\gamma$ and its interference with the non-resonant signal $e^+e^- \to \pi^+\pi^-\gamma$. The change in the shape of the spectrum with the model is sizeable and

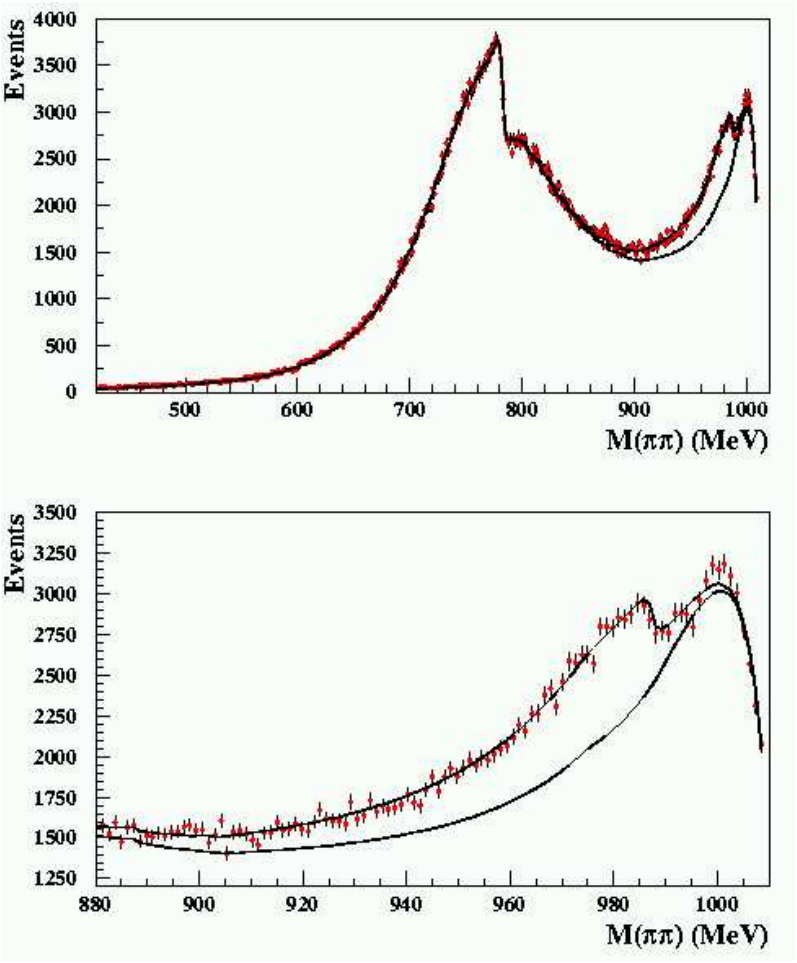

Figure 3.10: $M_{\pi\pi}$ spectrum: the bump around 980 MeV shows evidence for the signal $\phi \to f_0\gamma \to \pi^+\pi^-\gamma$. The upper and the lower curves are fits to the data, assuming the ϕ decays into $f_0\gamma$ through a charged kaon loop, and the background parametrization, respectively. The lower plot shows an enlarged view of the f_0 signal.

within the same model the value of the phase can enhance or not the contribution of the scalar mesons at low masses. A more detailed study of the scalar mesons contribution will be presented in §6.2.2.

3.3.2 Final State Radiation correction

The fraction of $\pi^+\pi^-\gamma_{FSR}$ in the spectrum at large photon angles is shown in fig. 3.11 after acceptance cuts, both in leading and next-to-leading order. The contamination of these events in the large photon angle region can arrive up to 30% (if counted together LO and NLO events) depending on the energy on the second photon (we remind that the acceptance cuts requires that one photon has to have an energy above 50 MeV). Unavoidably, the input for the FSR analysis and Monte-Carlo simulations will be model dependent: in PHOKHARA the model of scalar QED is used, where the pions are treated

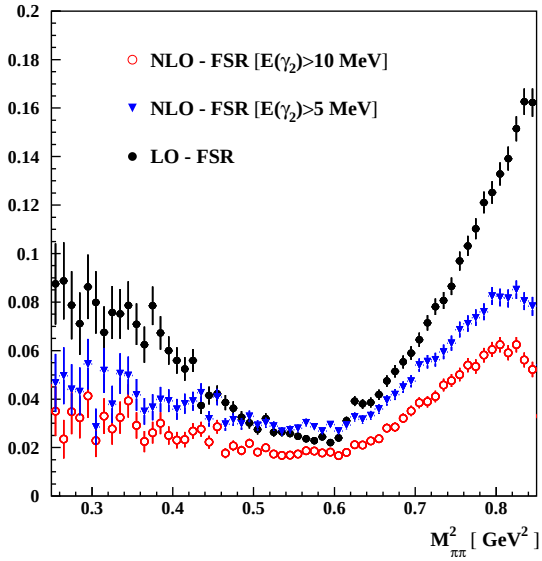

Figure 3.11: Fraction of leading (full points in black) and of next-to-leading order FSR at large photon angles, as a function of $M^2_{\pi\pi}$. The FSR-NLO contribution is estimated requiring for the second photon an energy above 5 MeV in one case (blue triangles) and above 10 MeV (red triangles) in the other case.

as point-like particles and the total FSR amplitude is multiplied by the pion form factor. While this assumption is generally plausible for relatively soft photons (corresponding to high value of $M_{\pi\pi}$), it might fail for lower values of the invariant mass of the hadronic system. In this case a possible extension of FSR beyond sQED has been considered in [79]. The impossibility of a model-independent estimate of the background $\pi^+\pi^-\gamma_{FSR}$ makes it necessary to test the validity of the model used. This is possible in the large photon angle region, because, there is a large amount of FSR. A consequence of the interference between ISR and FSR are the forward-backward and the charge asymmetry of the pion tracks. From the comparison between data and MonteCarlo, an upper limit on the validity of the model can be established, at least in the region where the *irreducible* background is negligible. In such a test, the presence of the scalar mesons cannot be neglected, having a big contribution, which varies according to the model used to parametrize them (see §3.4) The sQED model-dependence enters the analysis also in the estimate of the FSR-NLO contribution. These events cannot be distinguished from the signal, but since the cuts to reject the $\pi^+\pi^-\pi^0$ events are built by closing the kinematics under the hypothesis of being $\pi^+\pi^-\gamma$ events, unavoidably a fraction of signal events is cut out. Therefore the mass spectrum must be corrected for this effect. The only way to evaluate the correction is to rely on Monte-Carlo.

In the presence of FSR-NLO we have also to take into account that the invariant mass of the two pions system is different from the momentum transfer of the virtual photon ($M_{\pi^+\pi^-} < s_{\gamma^*}$), being the quantity at which the cross section has to be determined in order to be put into the $(g-2)_\mu$ integral. This difference (cured by the *unshifting* function in the

small angle analysis) is taken into account according the MonteCarlo prediction, and the mass spectrum will be corrected for it.

3.4 The forward-backward asymmetry as a test of sQED

The forward-backward asymmetry for a π^+ (π^-) is defined as:

$$\mathcal{A}_{\mathcal{FB}}(M_{\pi\pi}) = \frac{M_{\pi\pi}(\theta_{\pi^\pm} > 90^o) - M_{\pi\pi}(\theta_{\pi^\pm} < 90^o)}{M_{\pi\pi}(\theta_{\pi^\pm} > 90^o) + M_{\pi\pi}(\theta_{\pi^\pm} < 90^o)}) \tag{3.8}$$

It arises from the interference between ISR ($\pi^+\pi^-\gamma$ representing an odd charge conjugation state) and FSR and radiative ϕ decays, with $\pi^+\pi^-$ in an even charge conjugation state. The large photon angle region, given the big amount of FSR, is particularly suitable for the study of this variable. The interest in the asymmetry is twofold. As mentioned above it plays an important role in testing the model used to simulate FSR in MonteCarlo. On the other hand, the asymmetry allows powerful tests of models describing radiative ϕ decays via scalar mesons. The asymmetry is very sensitive to the models which describe the reaction $\phi \to S\gamma \to \pi^+\pi^-\gamma$ and within the models to the relative phase between sQED and the direct ϕ decay amplitudes, as is shown in fig. 3.12. In this plot two different models are used to simulate the radiative ϕ decay: the 'no structure' model and the K^+K^- model (see [64] and references there). The models includes both $f_0(980)$ and $f_0(600)$ intermediate states in the radiative chain $\phi \to (f_0(980)+f_0(600)+\gamma) \to \pi^+\pi^-\gamma$. Big effects are predicted according to the model.

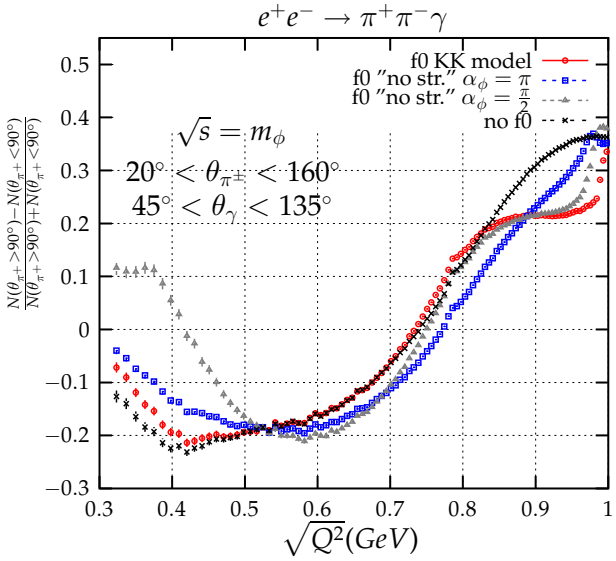

Figure 3.12: Forward-backward asymmetry for different radiative ϕ decay models compared with the asymmetry calculated within the sQED (no scalar mesons). α_ϕ is the phase between the sQED amplitude and the radiative ϕ decay amplitude. The plot is taken from [64].

An issue in studying the asymmetry is to disentangle the various contributions which act

simultaneously. If one takes into account that at low masses except for the effects of the two scalar mesons with their relative phases, some extensions of sQED are predicted ([79]), and that we have assumed that the contribution of $\phi \to \rho\pi \to \pi^+\pi^-\gamma$ is negligible, one understands that the number of parameters which play a role becomes quite big (see §6).

Chapter 4

The signal selection

In this chapter a detailed description of the selection of the data sample is presented. The full statistics of 240 pb^{-1} collected in the year 2002 is analyzed. The contamination of $\pi^+\pi^-\pi^0$ events and muon pairs is studied by means of a comparison between data and MonteCarlo and dedicated kinematical cuts have been worked out in order to reject it. Differently from the *irreducible* background the tail of $\pi^+\pi^-\pi^0$ and $\mu^+\mu^-\gamma$ events which enter the data sample after the whole selection are subtracted according to the MonteCarlo prediction. The data spectrum is obtained at the end of the chapter.

4.1 Selection of the sample

The event selection is based on the presence of two charged tracks with opposite curvature, forming a vertex close to the interaction point, and one photon detected in the barrel of the electromagnetic calorimeter. A particle ID method together with further kinematical cuts allows for an almost background free sample of $\pi^+\pi^-\gamma$ events.
The selection requirements are:

- the event has to satisfy the calorimeter trigger, i.e. at least two trigger sectors should have been fired within the barrel;
- the event has to pass the offline reconstruction filter: it identifies background events after the calorimeter cluster reconstruction has been finished and before the event enters the CPU-intensive pattern recognition and track- and vertex fitting algorithms. The filter acts on cosmic rays, machine background and Bhabha events at small polar angles (Bhabha events with electrons and positrons emitted at large polar angles are retained for measuring the integrated luminosity);
- there has to be one vertex connected to two charged tracks of opposite curvature. The vertex has to be located within a cylinder of $|z_{vtx}|$ <7 cm and radius $|x^2_{vtx} + y^2_{vtx}|$ <8

cm in the transverse plane;

- both tracks have to fulfill the following requirements:
  - a radius ρ_{FH} <50 cm of the first hit in the transverse plane of the drift chamber;
  - a point of closest approach (PCA) of the track fit extrapolation to the beam line $\rho_{PCA} = \sqrt{x^2_{PCA} + y^2_{PCA}}$ <8 cm or z_{PCA} <12 cm. The cut on the position of the PCA is applied to clean the sample from machine background;
  - a transverse momentum $|\vec{p}_T|$ >160 MeV or p_z >90 MeV in order to reject tracks spiralizing in the drift chamber;
- a cut in the plane ΔE_{miss} vs. M_{trk} is applied, being $\Delta E_{miss} = \sqrt{E^2_{miss} - |\vec{P}^2_{miss}|}$, with $E_{miss} = \sqrt{s} - \sqrt{|\vec{p}_{\pi^+}|^2 + m^2_{\pi^\pm}} - \sqrt{|\vec{p}_{\pi^-}|^2 + m^2_{\pi^\pm}}$ and $|\vec{P}_{miss}|^2 = |\vec{p}_\phi - \vec{p}_{\pi^+} - \vec{p}_{\pi^-}|^2$. The requirements on the two variables are: $(-220) < \Delta E_{miss} < 120$ MeV and $80 < M_{trk} < 400$ MeV. This cut prevents that the major part of $\pi^+\pi^-\pi^0$ events enter our data sample, rejecting more than 90% of them.

The events satisfying the requirements above, are requested to have both pions and at keast one photon at large angles ($50^o < \theta_{\gamma,\pi} < 130^o$). Moreover the photon is required to have an energy above 50 MeV and we explicitly require also that $M^2_{\pi\pi}$ <0.85 GeV^2 (given the presence of two or more photon events, there is not a 1:1 relation between the energy of the *tagging* photon and the invariant mass of the pions in the final state). This last request is necessary in order to exclude as much as possible the contribution from the scalar meson $f_0(980)$, which is very prominent in the high mass region (see fig. 3.10).
In the following we will call *large angle* the acceptance cuts:

- $50^o < \theta_{\pi^\pm} < 130^o$
- $50^o < \theta_\gamma < 130^o$
- at least one photon with E_γ >50 MeV
- $M^2_{\pi\pi}$ <0.85 GeV^2.

4.2 Background rejection

Three are the major sources of the *reducible* background of the analysis and for each of them specific kinematic cuts have been worked out in order to get rid of them.
Before entering into the details of each cut, we show the logic of the analysis in the flux diagram of fig. 4.1. The single cuts are applied in the same order as shown in the diagram. In the rest of this paragraph each single cut will be explained in detail.
Radiative Bhabha events $e^+e^- \to e^+e^-\gamma$ are cut by the same particle identification algorithm as used in the *small angle* analysis (§3.2), which distinguishes between pions

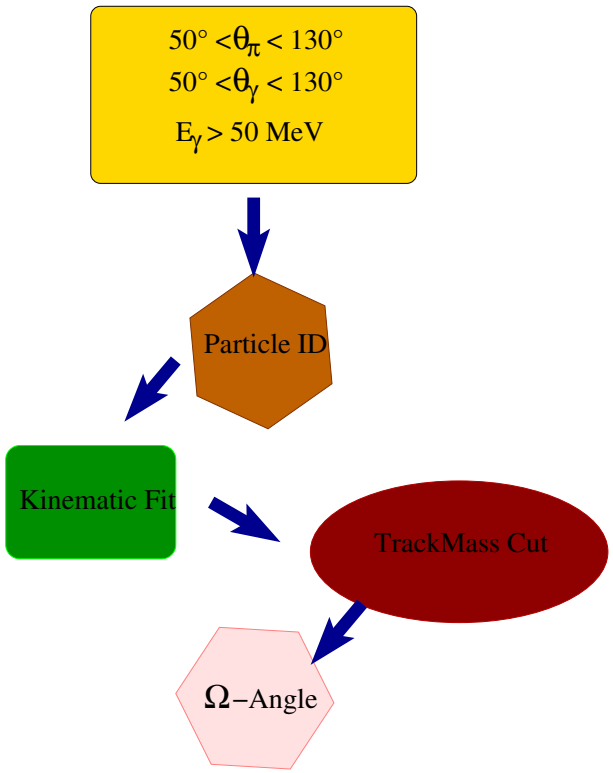

Figure 4.1: Flux diagram showing the logic of the analysis.

and electrons. The probability of the single track to be identified as a pion varies between 97% and 99% depending on the track momentum and on its polar angle (there is actually a drop for low momentum and at polar angles between 50^o and 60^o due to tracks that spiralize in the drift chamber). The event kinematics at *large angle* is such that requiring that only one track is recognised as a pion (as it was used in the *small angle* analysis) the contamination of Bhabha events varies between 1% at threshold and 7% at high masses. Viceversa asking that both tracks are identified as pions the efficiency for the full event decreases by some percent depending on the $M^2_{\pi\pi}$ (see §5.2) but this assures the complete rejection of Bhabha events from the data sample. Details of the particle ID estimation can be found in [72] and [73].

The main difficulty in obtaining a clean sample of $\pi^+\pi^-\gamma$ is to remove the huge $\pi^+\pi^-\pi^0$ contamination, which is concentrated especially at low $M_{\pi\pi}$ where the signal is statistically poorer (see fig. 3.7(b)). While the $\pi^+\pi^-\pi^0$ events need to be cut with a high efficiency, we have to keep a high efficiency for signal events for $M^2_{\pi\pi}$ <0.4 GeV^2. A kinematic fit has been developed for this purpose, and two further kinematic cuts act on the events surviving the fit. All these cuts are highly efficient in rejecting $\pi^+\pi^-\pi^0$, without affecting significantly the signal. They are described in detail in the next paragraphs, in the same order as they are applied in the selection procedure.

4.2.1 Kinematic fit

The kinematic fit has been worked out based on the $\pi^+\pi^-\pi^0$ hypothesis, with the aim to reject events using the $\chi^2_{\pi\pi\pi}$ of the fit. The fit has as inputs the curvature, the cotangent of the polar angle θ and the azimuthal angle ϕ of the two tracks and the three components of the momentum of the two photons. In case of more than two photons, the fit is repeated for each couple, and the minimum value of $\chi^2_{\pi\pi\pi}$ is chosen. Only a fraction of the data sample enters the fit procedure which requires to photons to be present; LO-$\pi^+\pi^-\gamma$ events which have not suffered from reconstruction effects (i.e. cluster splitting producing a second photon) are excluded *a priori* from the fit. It is important to keep under control the inefficiency of the fit on NLO-$\pi^+\pi^-\gamma(\gamma)$ events, which populates mainly the low mass spectrum region.
The twelve input quantities are constrained by 4-momentum conservation and by the fact that the invariant mass of the two photons has to give the π^0 mass, in total five constraints. The covariance matrix of the twelve inputs is also passed to the fit.
The fit uses the least-squares method, according to which, given N experimental points of a physical quantity, exists a theoretical model that predicts its value by some functional dependence. Let be $\underline{\eta}$ the vector of the 12 variables, for which we have the measurements $\underline{y}$, with the errors constrained in the covariance matrix $V(\underline{y})$ and $\underline{f}$ the equations of the constraints. According to the least-squares principle the best estimates of the unknown $\underline{\eta}$ are the ones for which hold simultaneously:

$$\begin{aligned} \chi^2(\underline{\eta}) &= (\underline{y}-\underline{\eta})^T V^{-1}(\underline{y})(\underline{y}-\underline{\eta}) = \text{minimum} \\ \underline{f}(\underline{\eta}) &= 0 \end{aligned} \tag{4.1}$$

Since the 12 input quantities are related to each other, a set of 5 Lagrange multipliers $\underline{\lambda}$ are added and eq. 4.1 becomes:

$$\chi^2(\underline{\eta}) = (\underline{y}-\underline{\eta})^T V^{-1}(\underline{y})(\underline{y}-\underline{\eta}) + 2\underline{\lambda}^T \underline{f}(\underline{\eta}) = \text{minimum} \tag{4.2}$$

We have now 12+5 unknowns. The problem is solved equating to zero the partial derivatives of χ^2 with respect to all the unknowns:

$$\begin{aligned} \nabla_\eta(\chi^2) &= -2V^{-1}(\underline{y}-\underline{\eta}) + 2F_\eta^T\underline{\lambda} = \underline{0} \qquad \text{(12 equations)} \\ \nabla_\lambda(\chi^2) &= 2\underline{f}(\underline{\eta}) = \underline{0} \qquad \text{(5 equations)} \end{aligned} \tag{4.3}$$

where the matrix F_η (of dimension 5×12) is $(F_\eta)_{ki} = \frac{\partial f_k}{\partial \eta_i}$. The solutions of eq. 4.3 is found iteratively: it is possible to show [80] that, if at the ν-th iteration the approximate solution is given by the values $\underline{\eta}^\nu, \underline{\lambda}^\nu$ at the next step the values will be:

$$\begin{aligned} \underline{\lambda}^{\nu+1} &= S^{-1}\left[\underline{f}^\nu + F_\eta^\nu(\underline{y}-\underline{\eta}^\nu\right] \\ \underline{\eta}^{\nu+1} &= \underline{y} - VF_\eta^T\underline{\lambda}^{\nu+1} \end{aligned} \tag{4.4}$$

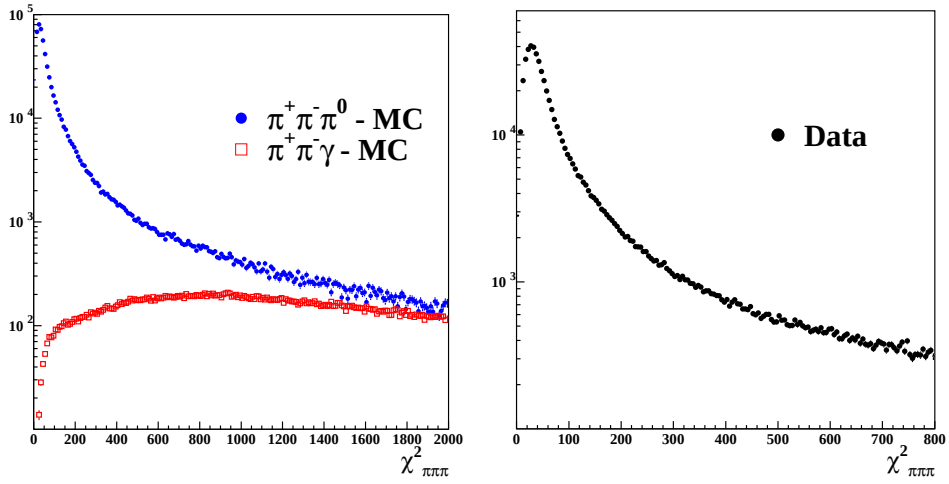

(a) (b)

Figure 4.2: (a) $\chi^2_{\pi\pi\pi}$ distribution for $\pi^+\pi^-\pi^0$ and $\pi^+\pi^-\gamma$ MonteCarlo events normalized to the integrated luminosity of the data sample. (b) $\chi^2_{\pi\pi\pi}$ distribution for the data sample.

where $S = F_\eta^\nu V (F_\eta^T)^\nu$. The iteration stops if for each of the 12 variables the difference between their values at the ν-th step and the ν-th+1 is smaller than 10^{-4}, or in our fit procedure after 20 iterations . At each step the constraints and their derivatives are re-calculated according to the new values of the variables η_i, in order to be minimized together with χ^2, and their variation weighted with the covariance matrix is taken into account in the estimate of the final values of η_i.

A pre-selection is applied to the events before entering the fit: we reject events which are out from the acceptance region $40^o < \theta_{\pi,\gamma} < 140^o$ and without at least one photon with energy above 40 MeV. In 4.2(a) the distribution of $\chi^2_{\pi\pi\pi}$ is shown for two MonteCarlo samples of $\pi^+\pi^-\pi^0$ and $\pi^+\pi^-\gamma$ events, both normalized to the integrated luminosity of the data sample. The fit distinguishes clearly between the signal and the $\pi^+\pi^-\pi^0$ background, given also the fact that only about 20% of the signal enters the fit, which is performed only in the presence of two (or more) photons. In 4.2(b) the distribution of $\chi^2_{\pi\pi\pi}$ for data is presented: at this stage of the analysis, the data sample is still dominated by $\pi^+\pi^-\pi^0$ events, therefore the shape of the distribution at low values of $\chi^2_{\pi\pi\pi}$ is very similar to the one from $\pi^+\pi^-\pi^0$ (fig. 4.2(a)).

The effect of the fit can clearly be visualized by looking at the resolution of the variables which enter in the minimization of the $\chi^2_{\pi\pi\pi}$. In fig. 4.3 the resolution of the curvature of the π^+ and of the photon energy are shown. For the curvature of the track the fit does not have a big effect, since the experimental errors in the detection of charged tracks are very small (see §2.2) and the fit therefore cannot change so much these quantities. The only effect is to center the resolution around the zero (see 4.3(a)).

Completely different is the effect on the photon quantities as shown in fig. 4.3(b), where

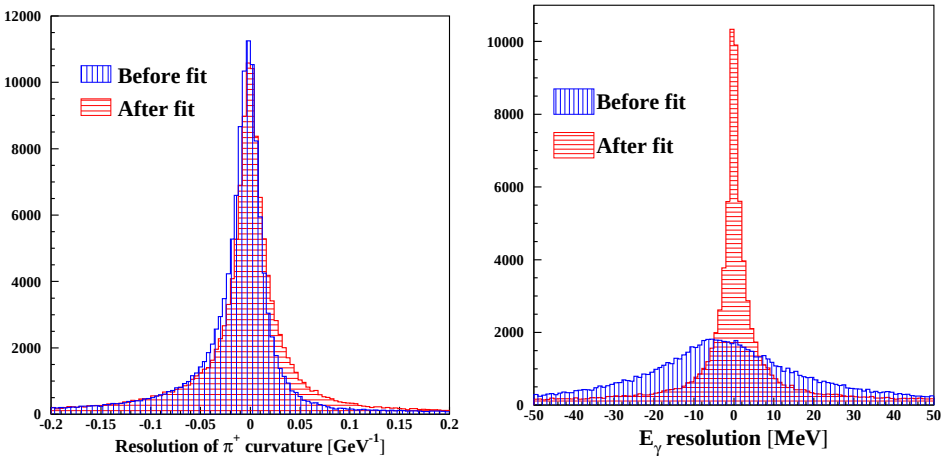

(a) (b)

Figure 4.3: Resolution of the curvature of the charged track (a) and of the photon energy (b) before (vertical blue filling) and after (red horizontal filling) the fit. The two distributions refer to a $\pi^+\pi^-\pi^0$ MonteCarlo sample.

the photon resolution before (vertical blue filling) and after (red horizontal filling) the fit is compared. The experimental error on the momentum of the photon is relatively big (∼20 MeV uncertainty for a photon of 100 MeV) and the fit can change significantly the inputs from the photon in order to satisfy its constrains (closure of the kinematics). The resolution after the fit is not only much more narrow, but it is also centered around the zero, while before the fit it results shifted of some MeV due to some EmC miscalibration.

About 40% of $\pi^+\pi^-\pi^0$ events are cut by rejecting events with a value of $\chi^2_{\pi\pi\pi}$ <200. The signal is almost unaffected by this cut, ecxept at low $M^2_{\pi\pi}$, where a maximum inefficiency of less than 2% is observed (see fig. 4.4(a)). The almost negligible loss of signal due to the cut justifies the chosen value of $\chi^2_{\pi\pi\pi}$. A study has been performed moving sistematically the cut on $\chi^2_{\pi\pi\pi}$ up to 500: the inefficiency of $\pi^+\pi^-\gamma$ events increases up to 6-7% while the rejection of $\pi^+\pi^-\pi^0$ background reaches 80%. We believe that the cut at 200 is a good compromise between the rejection power and the small inefficiency of the signal. Infact it allows to have an almost negligible signal iniefficiency, while it rejects a substantial part of 3 pions events. The surviving $\pi^+\pi^-\pi^0$ backgrond events will be rejected by two further kinematical cuts described in the following.

The small inefficiency of the signal events is explained by the fact that at low masses the emitted photon has high energies (higher than the π^0 mass), and the momentum distribution of the two pions from the signal can simulate pretty well the momentum distribution observed in the $\pi^+\pi^-\pi^0$ channel, as shown in fig. 4.4(b). The momentum distribution of the π^+ from a $\pi^+\pi^-\gamma$ and from a $\pi^+\pi^-\pi^0$ MonteCarlo simulations is plotted here at low $M^2_{\pi\pi}$. The shape of the two distributions is quite similar in this mass spectrum region, while is becomes completely different at higher values of $M^2_{\pi\pi}$.

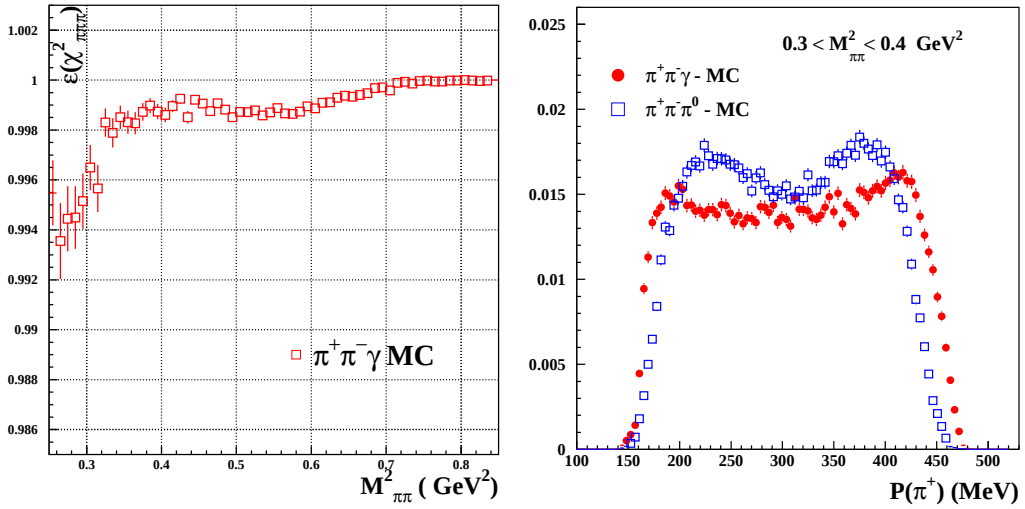

(a) (b)

Figure 4.4: (a) Inefficiency of the cut on $\chi^2_{\pi\pi\pi}$ at 200 for a MonteCarlo sample of $\pi^+\pi^-\gamma$. (b) Momentum distribution of the positive pion for $\pi^+\pi^-\pi^0$ (open blue squares) and $\pi^+\pi^-\gamma$ (full red circles) events, both from MonteCarlo simulations, in the mass range 0.3< $M^2_{\pi\pi}$ < 0.4 GeV^2.

4.2.2 Trackmass

In order to remove the background from the $\mu^+\mu^-\gamma$ channel and from the surviving $\pi^+\pi^-\pi^0$ events, the kinematical variable trackmass defined in eq. 3.4 has been used. In the plane $M^2_{\pi\pi}$ vs. m_{trk} of fig. 4.5(a) several populations are recognisable: around $m_{trk} = m_\mu$ the $\mu^+\mu^-\gamma$ events are concentrated mainly at high and at very low $M^2_{\pi\pi}$. Around $m_{trk} = m_\pi$ the signal is clearly visible, with an increasing number of events around the ρ mass, due to the *radiative return*. The upper left part of the plane appears empty because of the cut on the plane ΔE_{miss} vs. m_{trk} introduced in §4.1. From this region a residual fraction of $\pi^+\pi^-\pi^0$ background survives our cut, which corresponds to the curve superimposed in fig. 4.5(a). Similarly, in the lower part of the plane, a tail from the $\mu^+\mu^-\gamma$ channel contaminates our selected sample. In fig. 4.5(b) the same scatter plot of the data sample is shown: the three contributions, signal plus $\pi^+\pi^-\pi^0$ and $\mu^+\mu^-\gamma$ events, are clearly recognisable in the sample and the curves again describe the cut. The efficiency of the trackmass for muons is $M^2_{\pi\pi}$-dependent, varying from a rejection of ∼80% at high $M^2_{\pi\pi}$ up to more than 90% at threshold; in addition it removes also further ∼45% of $\pi^+\pi^-\pi^0$ events, that have survived the $\chi^2_{\pi\pi\pi}$ cut. For the signal the only effect is to lose a few percent of the sample around $M^2_{\pi\pi}$=0.3 GeV^2. This effect is visible in fig. 4.6, where the inefficiency of the cut evaluated by MonteCarlo is shown.

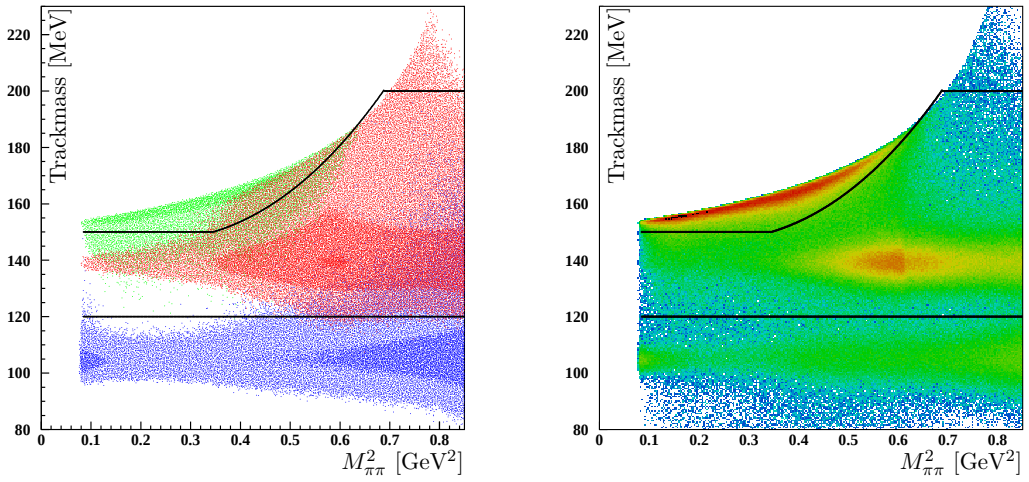

(a) (b)

Figure 4.5: (a) Event distribution in the plane $M^2_{\pi\pi}$ vs. m_{trk} at *large angle* for signal (in red) and $\pi^+\pi^-\pi^0$ (in green), $\mu^+\mu^-\gamma$ (in blue) background from MonteCarlo, after having required the particle ID. The three channels are normalized to the data luminosity. The line shows the cut used to select the signal. (b) The same as in (a) for data.

4.2.3 The Ω angle

Even after the cuts described above, at low $M^2_{\pi\pi}$ the contamination with $\pi^+\pi^-\pi^0$ events in the data sample is still ∼40%. In order to reduce it further, a dedicated cut has been worked out. It uses the angle Ω between the missing momentum and the momentum of the detected photon:

$$\Omega = acos\left(\frac{\vec{p}_{miss}\cdot\vec{p}_{\gamma}}{|\vec{p}_{miss}||\vec{p}_{\gamma}|}\right) \tag{4.5}$$

The Ω distribution peaks at zero for the signal, and it is off-zero for multi-photon events. Therefore it is a very powerful tool to separate signal from $\pi^+\pi^-\pi^0$ events, as can be seen in fig. 4.7(a). Here the Ω-angle distribution is plotted for a MonteCarlo sample of $\pi^+\pi^-\gamma$ (in red) and of $\pi^+\pi^-\pi^0$ events (in yellow). The distribution is obviously broadened for the $\pi^+\pi^-\pi^0$ background, being quite narrow for the signal. It should be emphasized that the width of the signal peak of fig. 4.7(a) is not only due to resolution effects but principally due to NLO signal events. At high values of $M_{\pi\pi}$ this effect becomes larger, due to a bigger impact of the NLO-ISR-photons. To take into account this broadening, a $M^2_{\pi\pi}$-dependent cut has been applied in the plane $M^2_{\pi\pi}$ vs. Ω. The cut has been fixed such as to reject as much $\pi^+\pi^-\pi^0$ events at low $M^2_{\pi\pi}$ as possible (where at this stage of the analysis they are concentrated) with the minimum loss of the signal. The actual cut is shown in the scatter plot of fig. 4.7(b): in black the $\pi^+\pi^-\pi^0$ population is displayed, and in red the signal one. Is is possible to see the radiative tail of the signal, distinguishable by the large value of the

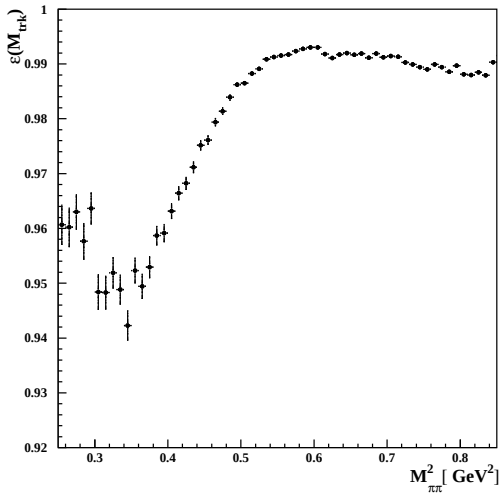

(a)

Figure 4.6: Efficiency of the cut on trackmass as a function of $M^2_{\pi\pi}$ evaluated from a $\pi^+\pi^-\gamma$ MonteCarlo sample.

Ω-angle. In principle, it would be possible to cut harder at low $M^2_{\pi\pi}$ without loosing much of the signal, but in order to avoid large systematic errors due to this cut, we prefer to keep as much as possible of the signal. For more details we refer to §5.3.3.
The cut results in a rejection of more than 90% of the $\pi^+\pi^-\pi^0$ events which survived the previous cuts, with a loss of only a few percent of the signal at the threshold up to a maximum of $\sim$10% at high $M_{\pi\pi}$. In fig. 4.8 the efficiency of this cut on a MonteCarlo sample of $\pi^+\pi^-\gamma$ events is displayed: the drop of the efficiency is due to the already mentioned two-photons events (black points). Using a $\pi^+\pi^-\gamma$ MonteCarlo sample (red full circles) which simulates one-photon $\pi^+\pi^-\gamma$ events (ISR-LO and FSR-LO), the efficiency of the cut is almost flat from 0.5 GeV^2 up to the end of the spectrum. If we include NLO-events in the simulation, the efficiency goes down by a few percent. The reason is that the Ω-angle is built by closing the kinematics under the hypothesis of one photon only. Double photon events have a relative high probability to be rejected, first of all at high $M^2_{\pi\pi}$ where NLO-ISR are quite abundant. Moreover part of the NLO-events at low masses are cut by the trackmass cut, which is more rigid at low $M^2_{\pi\pi}$ (and is applied one step earlier), making the relative concentration of NLO events larger at high $M^2_{\pi\pi}$.

4.3 Estimate of the residual background

The amount of the residual background at the end of the selection procedure is estimated in a first stage from MonteCarlo normalizing the samples to the integrated luminosity of data. In a second stage we will check the validity of the simulation in a detailed comparison

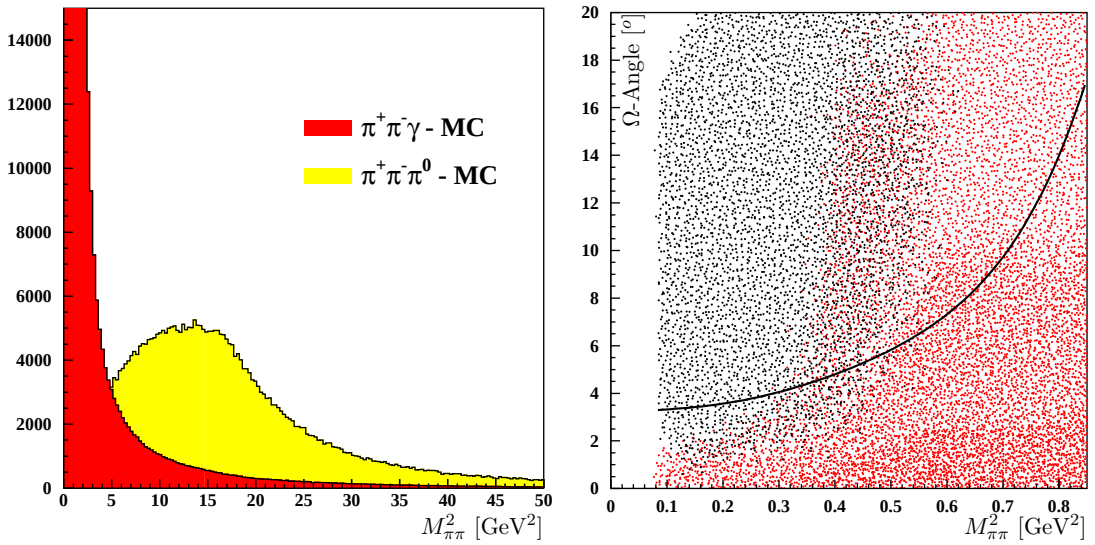

(a) (b)

Figure 4.7: (a) Ω distribution inclusive in $M_{\pi\pi}$ for $\pi^+\pi^-\gamma$ (in red) and $\pi^+\pi^-\pi^0$ events (in yellow), both from MonteCarlo. (b) Event distribution in the plane Ω vs. $M^2_{\pi\pi}$. Red is for $\pi^+\pi^-\gamma$ and black for $\pi^+\pi^-\pi^0$ events (from MonteCarlo). The line represents the cut applied.

data-MonteCarlo for some selected variables and corrections -if needed- will be applied. We anticipate here the results of such checks, i.e. that the MonteCarlo for the $\mu^+\mu^-\gamma$ events describes quite precisely the data (§4.3.2), while the simulation of the $\pi^+\pi^-\pi^0$ events needs to be rescaled in order to give a good prediction (§4.3.1).

For both channels $\mu^+\mu^-\gamma$ and $\pi^+\pi^-\pi^0$ the pollution in the final data sample is evaluated looking at the number of MonteCarlo events which survive the chain of the selection cuts. The contamination from $\pi^+\pi^-\pi^0$ events is maximum at low masses, with a percentage of 13-14% at $M^2_{\pi\pi}$ =0.25 GeV^2 down to the per-mil level at higher masses, while the muon pairs contamination arrives at up to 10% at low and high masses. The two contaminations are shown in fig. 4.9 where the relative amount of $\pi^+\pi^-\pi^0$ and $\mu^+\mu^-\gamma$ after the whole selection are plotted respectively.

An overall check of the background subtraction can be done looking at the trackmass distribution for data and MonteCarlo at the end of the selection and comparing the two. This variable is particularly suitable for this kind of controls, since the signal and the several background channels are differently distributed. More significant is the comparison if done in slices of $M^2_{\pi\pi}$ in such a way to take into account the different populations of background in the different $M^2_{\pi\pi}$ regions. Some examples are shown in fig. 4.10, for different slices of $M^2_{\pi\pi}$. Both the muon-peak and the $\pi^+\pi^-\pi^0$ tail (above the π mass) are well reproduced by MonteCarlo.

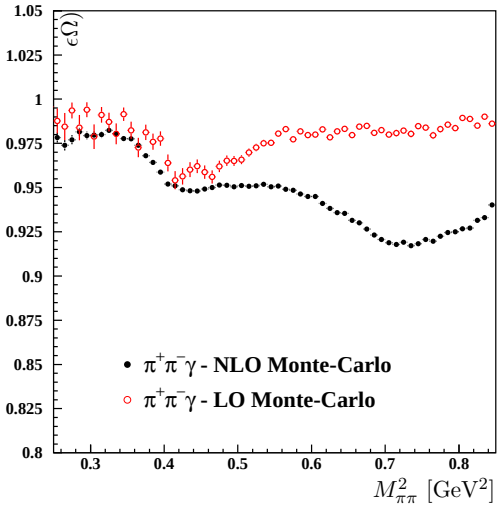

Figure 4.8: Efficiency of the Ω-angle cut evaluated for two different $\pi^+\pi^-\gamma$ MonteCarlo samples. In full black points a FSR-NLO MonteCarlo production is used while in full red circles the efficiency is evaluated with FSR-LO MonteCarlo production.

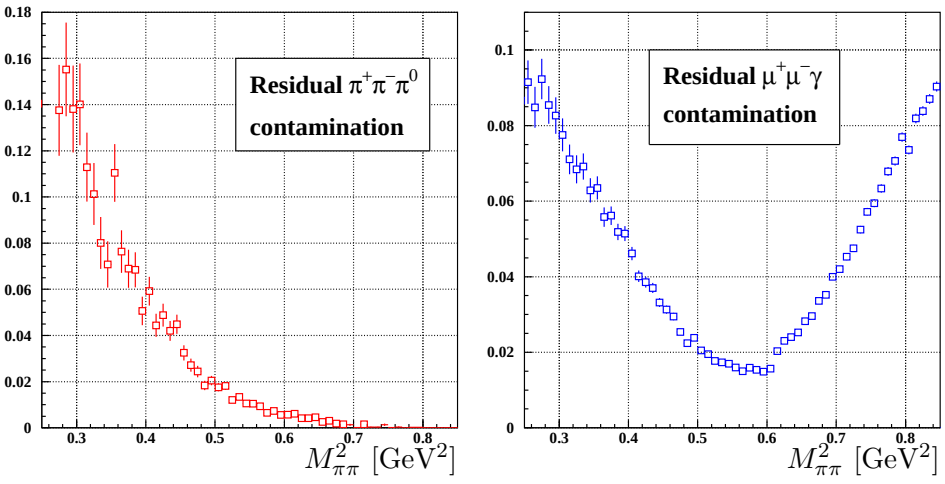

(a) (b)

Figure 4.9: Contamination in the final data sample of $\pi^+\pi^-\pi^0$ (a) and of $\mu^+\mu^-\gamma$ (b) background at the end of the selection.

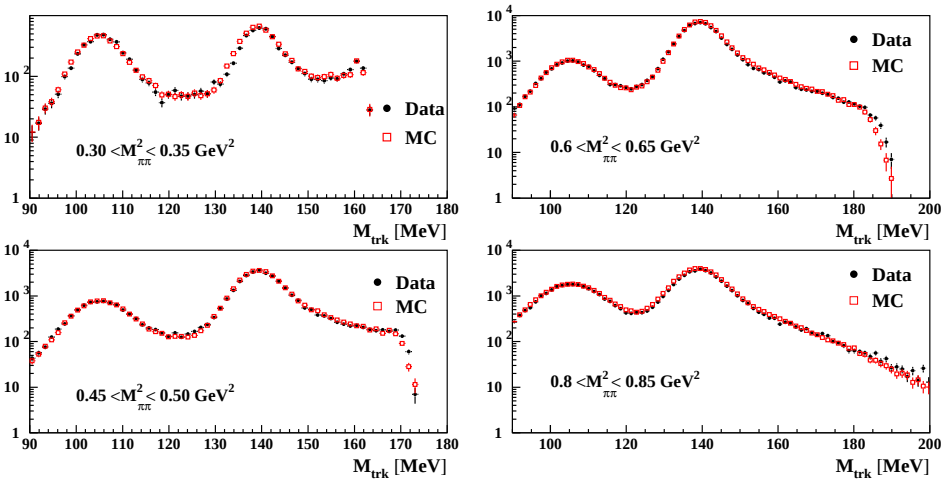

(a) (b)

Figure 4.10: Trackmass distribution in slices of $M^2_{\pi\pi}$ for data and MonteCarlo (signal and residual background). Both background and signal MonteCarlo are normalized to the integrated luminosity of data.

4.3.1 $\pi^+\pi^-\pi^0$ contamination

As anticipated in the introduction the $\pi^+\pi^-\pi^0$ MonteCarlo sample needs to be rescaled. For estimating the scale factor, in a first step we select a sample of data dominated by $\pi^+\pi^-\pi^0$ events, and in a second stage we rescale our $\pi^+\pi^-\pi^0$ MonteCarlo in order to reproduce the data.

The region of trackmass above the π-peak is populated by the tail of $\pi^+\pi^-\gamma$ events (NLO-events where the emission of the second photon tends to shift the value of the trackmass towards the right with respect to $m_{\pi^\pm}$) and in bigger amount by $\pi^+\pi^-\pi^0$ events. In fig. 4.11(a) the trackmass distribution from $m_{\pi^\pm}$ up to ∼160 MeV is shown for $\pi^+\pi^-\gamma$ data and MonteCarlo normalized to the luminosity of data (for a bin of $M^2_{\pi\pi}$). It is evident that in the region M_{trk} >150 MeV there is an excess to events of data due to $\pi^+\pi^-\pi^0$ events, which becomes dominant above 155 MeV. The fact that the M_{trk} distribution decreases rapidly at ∼160 MeV is due to the the ΔE_{miss} cut, a variable which is highly correlated with M_{trk}.

Under the assumption that the excess in data in the region 150< M_{trk} <160 MeV is due to $\pi^+\pi^-\pi^0$ events only, subtracting the $\pi^+\pi^-\gamma$ events from the data sample we should remain with the $\pi^+\pi^-\pi^0$ contamination still present in the data. We can check then the prediction of the $\pi^+\pi^-\pi^0$ MonteCarlo by comparing the M_{trk} distribution in the range 150÷165 MeV with data. The comparison is shown for two different bins on $M^2_{\pi\pi}$ in the two lower plots of fig. 4.11(a). The black full points represent the data spectrum after the $\pi^+\pi^-\gamma$ subtraction and in blue (triangles) the MonteCarlo prediction for $\pi^+\pi^-\pi^0$ events normalized to the luminosity of data. In both the examples shown here, we observe that the

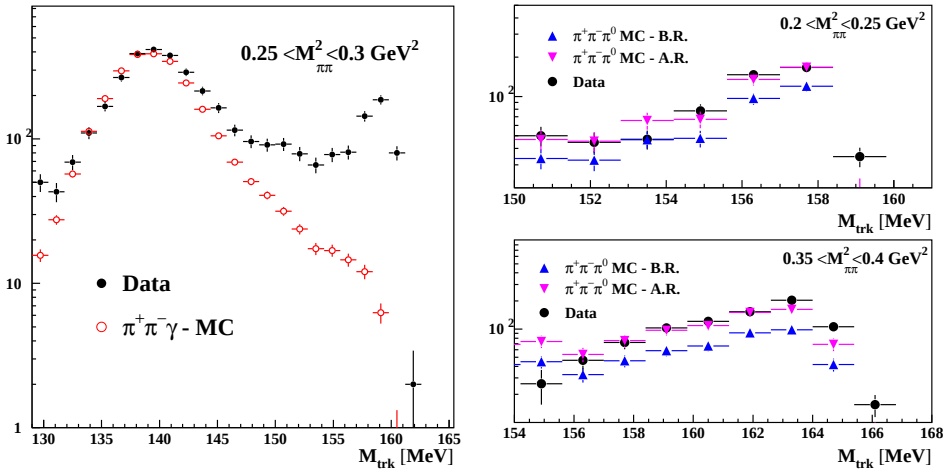

(a) (b)

Figure 4.11: (a) Comparison between data (full black points) and $\pi^+\pi^-\gamma$ MonteCarlo (open red circles) in the trackmass distribution between 130 and 165 MeV. (b) Trackmass distribution above 130 MeV for data subtracted from $\pi^+\pi^-\gamma$ events (full black points) compared with the $\pi^+\pi^-\pi^0$ MonteCarlo without the rescaling (pink triangles, 'B.R.') and after the rescaling (blue triangles, 'A.R.').

$\pi^+\pi^-\pi^0$ MonteCarlo prediction underestimates the amount of these events which populate the final data sample. In order to have a realistic estimate from MonteCarlo, we rescale this latter to reproduce the data points of fig. 4.11(b). The rescaled MonteCarlo is shown in pink triangles, which are in a reasonable agreement with data. The scale factor is evaluated for each bin of $M^2_{\pi\pi}$: it is almost flat in $M^2_{\pi\pi}$ (with the exception of one bin) and is equal to about 60%. The values for each bin of $M^2_{\pi\pi}$ are listed in the tab. 4.1. In this procedure all the selection cuts are applied except the m_{trk} cut. Part of the events which have been used in the estimate of the scale factors are cut by the m_{trk} cut (fig. 4.5). The procedure is then based on the assumption that the tail of $\pi^+\pi^-\pi^0$ events which enters the final sample behaves as the sub-sample used for evaluating the scale factor.

In order to evaluate the systematic error associated to the $\pi^+\pi^-\pi^0$ subtraction we have again used the sub-sample in the plane M_{trk} >150 MeV and $M^2_{\pi\pi} < 0.45$ GeV^2. By comparing the Ω-Angle distribution obtained from data (subtracted the tail of the $\pi^+\pi^-\gamma$ events) and from the $\pi^+\pi^-\pi^0$ scaled-MonteCarlo [1] we find a limit in the MonteCarlo description. The comparison (shown in fig. 4.12) is done at the end of the analysis cuts, included the cut on the Ω-Angle. This explains the drop at 4^o of the distribution which is not sharp because the Ω-cut is $M^2_{\pi\pi}$-dependent. In the lower plot of fig. 4.12 the ratio between data and MonteCarlo is shown. Even if statistically limited the agreement is good. The ratio has

[1]The Ω-Angle distribution here refers to events with $M^2_{\pi\pi} < 0.45$ GeV^2: the scale factor to correct the $\pi^+\pi^-\pi^0$ MonteCarlo is the average of the scale factors for the single bins (tab. 4.1) up to 0.45 GeV^2

$M^2_{\pi\pi}$ [GeV^2]	Scale Factor
0.085÷0.2	1.65
0.2÷0.25	1.4
0.25÷0.3	1.6
0.3÷0.35	1.6
0.35÷0.4	1.65
0.4÷0.45	1.7
0.45÷0.5	1.6
0.5÷0.55	1.6

Table 4.1: Scale factor applied to the $\pi^+\pi^-\pi^0$ MonteCarlo for different bins of $M^2_{\pi\pi}$.

been fitted with a straight line and the result of the fit (2%) multiplied by the contamination of the $\pi^+\pi^-\pi^0$ events in the data sample (fig. 4.9(a)), gives the systematic error associated to the $\pi^+\pi^-\pi^0$ background subtraction. The biggest $\pi^+\pi^-\pi^0$contamination is ∼15% at low $M^2_{\pi\pi}$ where an error of 0.3% on this background channel is estimated. The $\pi^+\pi^-\pi^0$ background decreases up to become negligible on the ρ-peak. Tab. 4.2 reports the systematic error associated to the $\pi^+\pi^-\pi^0$ subtraction.

$M^2_{\pi\pi}$ range [GeV^2]	$\pi^+\pi^-\pi^0$ contamination	Systematic error
0.25÷0.3	15%	0.3%
0.3÷0.35	10%	0.2%
0.35÷0.4	7%	0.1%
0.4÷0.45	5%	0.1%
0.45÷0.5	3%	0.06%
0.5÷0.55	2%	0.04%
0.55÷0.6	<1%	<0.02%

Table 4.2: For the different $M^2_{\pi\pi}$ intervals (first column) the contamination of $\pi^+\pi^-\pi^0$ events in the data sample (second column) is listed together with the its systematic error (third column).

4.3.2 $\mu^+\mu^-\gamma$ contamination

For the evaluation of the muon pairs background a similar work has been done. As in the case of $\pi^+\pi^-\pi^0$ background, firstly we have selected a sample of $\mu^+\mu^-\gamma$ events from data, then we have compared it with the MonteCarlo simulation.

Being the trackmass peaked at m_μ for $\mu^+\mu^-\gamma$ and at m_π for $\pi^+\pi^-\gamma$, it allows to separate $\mu^+\mu^-\gamma$ from $\pi^+\pi^-\gamma$ events in the data (neglecting the tails of the two which overlap each other). Running the full analysis requiring M_{trk} <120 MeV, we can select a sample of $\mu^+\mu^-\gamma$ from the data sample. After subtracting the tail of $\pi^+\pi^-\gamma$ events, we have compared the $M^2_{\mu\mu}$ spectrum with the one from MonteCarlo (both $\mu^+\mu^-\gamma$ and $\pi^+\pi^-\gamma$ MonteCarlo are normalized to the integrated luminosity of the data). In the upper plot of fig. 4.13(a) we see

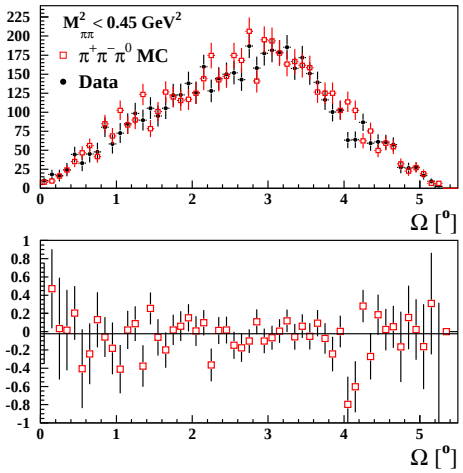

Figure 4.12: Ω-angle distiution for data and MonteCarlo selected with $M^2_{\pi\pi}$ <0.45 GeV^2 and m_{trk} >150 MeV in the upper plot and their ratio in the lower plot.

the comparison of $M^2_{\mu\mu}$ between data and MonteCarlo in the region M_{trk} <120 MeV and in the lower one is the ratio between the two. The agreement data-MonteCarlo is excellent up to 0.55 GeV^2, while we observe discrepancies of up to 5% at higher masses. Such a discrepancy might be due to some differencies in efficiencies between data and the $\mu^+\mu^-\gamma$ MonteCarlo simulation.

In order to give a systematic uncertainty of the subtraction of this background, we have looked again at the trackmass distribution (from 80 to 120 MeV) in the different slices of $M^2_{\pi\pi}$ and for each of them we have counted the number of events in data and in MonteCarlo. The relative difference in the i-th bin multiplied by the $\mu^+\mu^-\gamma$ contamination in the particular bin gives the systematic error (in that bin of $M^2_{\pi\pi}$):

$$\epsilon_i^{\mu\mu\gamma}(M^2_{\pi\pi}) = \frac{N_i^{Data} - N_i^{MC}}{N_i^{Data}} \times F_i(\mu\mu\gamma) \tag{4.6}$$

where N_i^{Data} and N_i^{MC} are the number of events in the μ-peak for data and MonteCarlo in the i-th bin and $F_i(\mu\mu\gamma)$ is the contamination of $\mu^+\mu^-\gamma$ events in the data sample.

In fig. 4.13(b) some examples of the trackmass distribution for data and MonteCarlo are presented. As for the mass spectrum, the tail of $\pi^+\pi^-\gamma$ according to MonteCarlo prediction, has been subtracted. These plots confirm the result shown in fig. 4.13(a), i.e. looking at the trackmass distribution a good agreement is observed at low masses while a difference of few percent is present at high masses.

For each bin of $M^2_{\pi\pi}$ the relative difference observed in the muon peak between data and MonteCarlo is listed in tab. 4.3, together with the $\mu^+\mu^-\gamma$ contamination in the data sample at the end of the selection and the resulting systematic errors. The estimate of the systematic error of the muons subtraction is the product of the total contamination times the difference data-MonteCarlo. In this procedure there is implicitly the assumption made

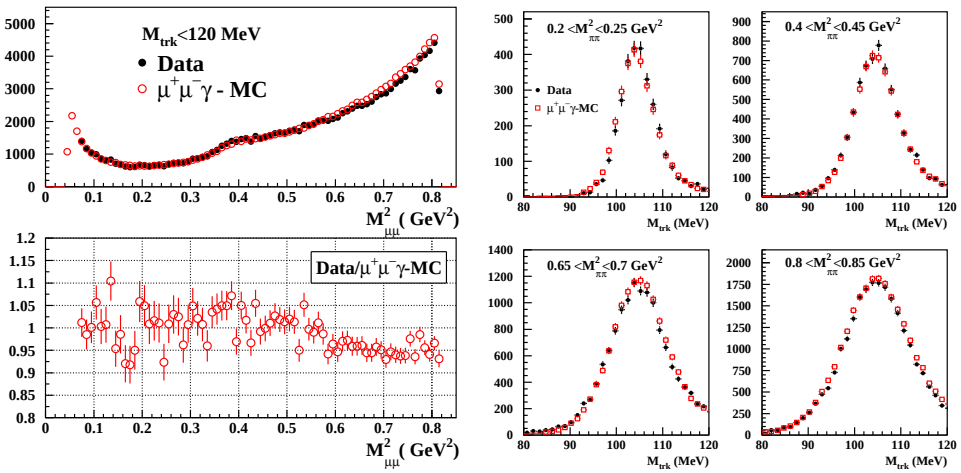

(a) (b)

Figure 4.13: (a) Mass spectrum distribution at *large angle* for $\mu^+\mu^-\gamma$ MonteCarlo (open red squares) compared with one from data (full black points) for M_{trk} <120 MeV (upper plot) and their ratio (lower plot). (b) Trackmass distribution for $\mu^+\mu^-\gamma$ MonteCarlo (open red squares) and for data (full black points) for M_{trk} <120 MeV in different slices of $M^2_{\pi\pi}$. Both in (a) and in (b) the residual $\pi^+\pi^-\gamma$ events have been subtracted from the data sample.

$M^2_{\pi\pi}$ range (GeV^2)	Difference data-MC	$\mu^+\mu^-\gamma$ contamination	Systematic error
0.25÷0.3	0.6%	6.0%	4×10^{-4}
0.3÷0.35	1.0%	5.0%	5×10^{-4}
0.35÷0.4	1.3%	4.0%	5×10^{-4}
0.4÷0.45	0.3%	3.0%	9×10^{-5}
0.45÷0.5	0.2%	2.0%	4×10^{-5}
0.5÷0.55	2.0%	1.5%	3×10^{-4}
0.55÷0.6	1.0%	1.3%	1×10^{-4}
0.6÷0.65	1.0%	1.8%	2×10^{-4}
0.65÷0.7	1.3%	3.0%	4×10^{-4}
0.7÷0.75	5.0%	5.0%	3×10^{-3}
0.75÷0.8	5.0%	7.0%	4×10^{-3}
0.8÷0.85	5.0%	8.0%	4×10^{-3}

Table 4.3: For different $M^2_{\pi\pi}$ intervals the systematic error on the $\mu^+\mu^-\gamma$ events subtraction (third column) is obtained as the relative difference between data and MonteCarlo estimated on the $\mu^+\mu^-\gamma$ peak of the trackmass (first column) multiplied by the muon contamination (second column).

that in the tail of the muon distribution the same difference between data and MonteCarlo is present as for m_{trk} <120 MeV. In order to check the validity of this assumption we have selected a different sample of data, by applying all the analysis cut with the only difference in the m_{trk} cut. Instead of requiring the standard m_{trk} cut (the curves of fig. 4.5) we have selected events with trackmass between 115 and 130 MeV. This subsample is populated both by muon pairs and by $\pi^+\pi^-\gamma$ events with roughly the same

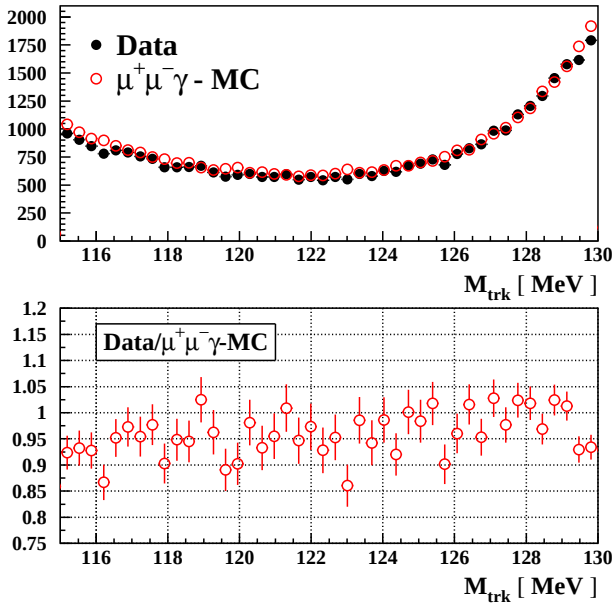

Figure 4.14: Comparison of the trackmass distribution between data and MonteCarlo for events with $115 < M_{trk} < 130$MeV. The data (full black points) have been subtracted from $\pi^+\pi^-\gamma$ and $\pi^+\pi^-\pi^0$ (according to MonteCarlo). The ratio between data and MonteCarlo is shown in the lower plot.

weight and a big part of it passes our selection. By subtracting the $\pi^+\pi^-\gamma$ events according to the MonteCarlo prescription and the small tail of $\pi^+\pi^-\pi^0$ events, we remain with a sample of $\mu^+\mu^-\gamma$ events selected by data, that can be compared directly with the $\mu^+\mu^-\gamma$ MonteCarlo. Such a comparison is shown in fig. 4.14: the full black points represent the data subtracted of $\pi^+\pi^-\gamma$ and $\pi^+\pi^-\pi^0$ events and the open red circles stand for the $\mu^+\mu^-\gamma$ MonteCarlo. The lower plot, showing the ratio between data and MonteCarlo of the trackmass distribution, confirms the difference of few percent observed in the complementary sub-sample (M_{trk} <120 MeV, lower plot of fig. 4.14).

4.4 Large angle spectrum

Applying the selection of §4.1 and §4.2 to the 242.7 pb^{-1} of data collected during the year 2002, the distribution of $\pi^+\pi^-\gamma$ events shown in fig. 4.15 is obtained. The background events surviving the analysis cuts (see description above), are subtracted from the data sample. The background rejection (first of all of the $\pi^+\pi^-\pi^0$ channel) is performed using both drift chamber and calorimeter information. The trackmass cut (built only with information from the drift chamber), which cleans the data sample in the *small angle* analysis, has to be supplemented in the *large angle*. It is the *tagging* of the photons, namely the use of the calorimeter information, which allows to perform the kinematic fit and to cut on the Ω angle, and consequently to remove the $\pi^+\pi^-\pi^0$ contamination from the data.
This argument obviously does not apply to the *irreducible* background, which is still included

in the spectrum of fig. 4.15. The distribution shows the event yield after the application of the acceptance cuts ($50^o < \theta_{\pi,\gamma} < 130^o$). The ρ peak and the $\rho - \omega$ interference are clearly visible, even without any unfolding for experimental effects, demonstrating the high momentum resolution of the KLOE drift chamber.

It is also clearly visible that the spectrum reaches the threshold 2π. We have illustrated in §3.3.2 and §3.4 which are the issues for a precise measurement down to the $2m_\pi$ threshold. Several effects act simultaneously in this region, which are very difficult to disentangle. This effects are more easily understandable using the data that KLOE has collected in 2006 at center-of-mass energy $\sqrt{s} < m_\phi$ (off-peak data, see §7.2). The scalar contribution is very much suppressed in this sample as well as the $\pi^+\pi^-\pi^0$ contamination (reduced to more than 90%). With this data it will be easier to explore the threshold region, and it is very likely that a more precise measurement can be performed.

The *large angle* analysis on-peak, as described above, allows however to repeat the pion form factor measurement in the same energy range covered by the *small angle* analysis, namely in ρ-peak region. Additional data in this region are needed, given the discrepancy between the e^+e^-- and the τ-data and the not perfect agreement among the different e^+e^- experiments.

During the development of this work the theoretical knowledge of the scalar mesons has improved considerably. The data sample presented here becomes indeed important to check models which have been developed for these processes. A work in this direction has been already started and it will be described in §6.2.2.1. We limit ourselves in the context of this thesis to the mass region where the contribution of the scalar mesons is small, i.e. in the mass range $0.5 \div 0.85$ GeV^2. The experimental work, such as the study of the efficiencies, evaluations of the systematic errors, have been performed in the wider region $0.25 \div 0.85$ GeV^2.

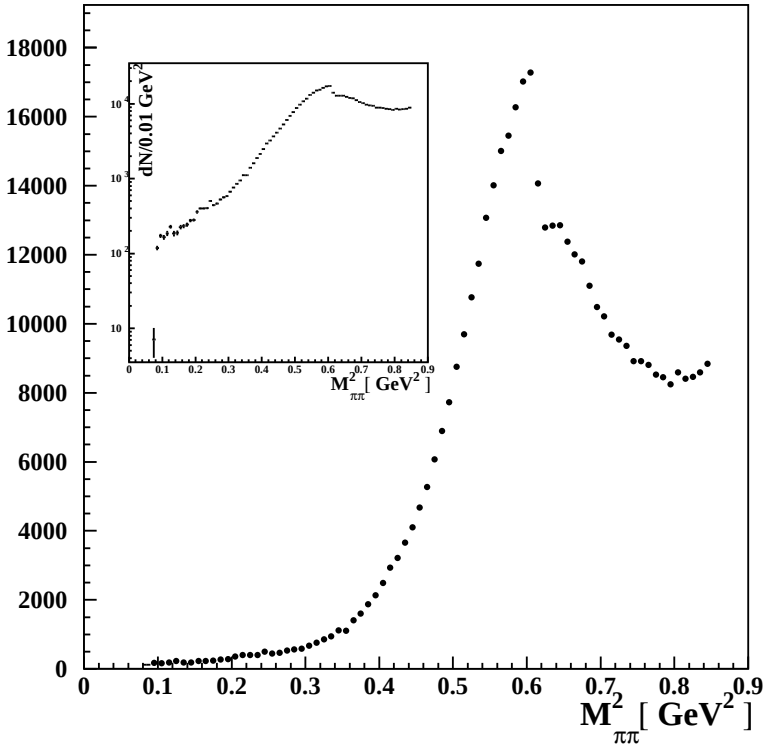

Figure 4.15: $\pi^+\pi^-\gamma$ event yield as a function of $M^2_{\pi\pi}$ in bins of 0.01 GeV^2 in the fiducial volume and after the selection cuts and the subtraction of the *reducible* background. The integrated luminosity of the data sample is $\mathcal{L} = 242.7$ pb^{-1}.

Chapter 5

Evaluation of efficiencies and associated systematics errors

In the present chapter the evaluation of the total analysis efficiency is presented. The aim is to correct the mass distribution for the signal efficiency of each individual cut applied in the analysis and for potential losses during the event reconstruction, such as tracking and EmC clustering.
The strategy is to use an *effective global efficiency* taken from MonteCarlo and in case of differences between data and the simulation, we correct for such a difference. In the *effective global efficiency* we take into account several effects:

- the loss of signal events due to the selection cuts;
- the correction for the geometrical acceptance;
- the efficiency for the FSR-NLO events;
- the correction for the shifting due to FSR-NLO events;
- the rejection of the FSR-LO events;
- the correction for reconstruction effects.

This strategy is possible thanks to the a special version of the PHOKHARA (Ω version) event generator, in which is possible to recognise whether a photon is from an ISR- or from an FSR-process. We remind the reader of the presence of two kinds of Final State Radiation: FSR-LO where a single photon is emitted in the final state and FSR-NLO where simultaneously a photon in the initial state and another one in the final state are radiated. The first process represents a background, with $s_{\gamma^*} = m_\phi^2$ not lowering the center-of-mass energy of the hadronic system. The second kind of events contributes to the signal, because the invariant mass of the intermediate photon is lowered with respect to the center of mass energy. Therefore we need to evaluate the inefficiency of the analysis cuts for these events

and to correct for it. The loss of this kind of events is shown in fig. 5.1(a). In this plot the spectrum for NLO-events is plotted, after the acceptance (red points) and after the whole selection cuts (open blue circles). The difference between the two distributions (that reaches up to 20%) is due to the cuts to reject the background.
In both cases of FSR (-LO and -NLO) the experimental quantity that we measure $M^2_{\pi\pi}$ is shifted with respect to the transfer momentum of the virtual photon ($M^2_{\pi\pi} \neq s_{\gamma^*}$), and the shift is related to the energy of the photon in the final state. Since in the Ω version of PHOKHARA we know whether the photons come from the initial or the final state, we can build directly the quantity s_{γ^*} and evaluate the ratio between the $M^2_{\pi\pi}$ distribution and the one in the variable s_{γ^*}. This is done in the lower plot of fig. 5.1(b): we observe that the effect is relatively large, due to the big amount of NLO events at large angles.
Correcting for such a shift we automatically cut out the FSR-LO events. In fact if one looks at the spectrum as a function of s_{γ^*} rather than of $M^2_{\pi\pi}$ after the correction, the FSR-LO events are peaked at m^2_ϕ, which is beyond the region of our interest ($M^2_{\pi\pi}$ <0.85 GeV^2).
The correction for the reconstruction effects are also taken from MonteCarlo. The event generator PHOKHARA-Ω has been inserted into the KLOE detector simulation. For each event we have both the *true* information and the reconstructed ones for pions and photons. Technically the *effective global efficiency* has been obtained according to the formula:

$$\epsilon(i) = \frac{dN^{rec}(i)/dM^2_{\pi\pi}[50^o < \theta_{\gamma,\pi^\pm} < 130^o, \text{end of analysis}]}{dN^{true}(i)/ds_{\gamma^*}[0^o < \theta_{\gamma,\pi^\pm} < 180^o]} \tag{5.1}$$

for the i-th bin.
The result of this procedure is shown in the upper plot of fig. 5.1(b), where the *effective global efficiency* is plotted as a function of $M^2_{\pi\pi}$.
For each single analysis cut k we have compared the efficiency from data and MonteCarlo; in case they are the same, no correction is needed, because the correction for that specific step k is automatically included in the *effective* total efficiency. If a difference is found at step k, we have to correct the *effective global efficiency* from MonteCarlo with the ratio data over MonteCarlo of the efficiency of the step k. In this way we correct for the effects which are not so precisely reproduced by MonteCarlo.
In the next paragraphs the evaluation of the individual efficiencies will be described, while the rest of the chapter is dedicated to the evaluation of the systematic errors of the several cuts applied.
In the following when we will refer to *standard analysis*, we mean the full set of cuts described in the previous chapter, i.e. as shown in the flux diagram of fig. 4.1.

5.1 The evaluation of the efficiencies

In the next paragraphs we will present the evaluation of the trigger, of the tracking and of the vertex efficiency. For the tracking we use a control sample of $\pi^+\pi^-\pi^0$ events while the

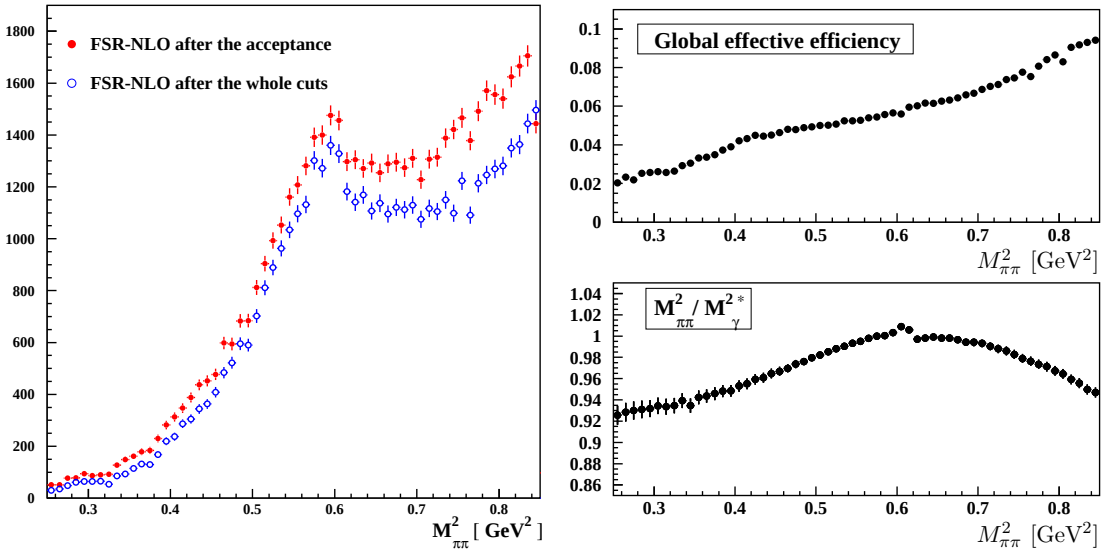

(a) (b)

Figure 5.1: (a) Spectrum distribution for FSR-NLO events (only) after the acceptance cuts (full red points) and after all the analysis cuts (open blue points). (b) Upper plot: *effective global efficiency* for $\pi^+\pi^-\gamma$ events; lower plot: radiative correction due to to the shift from $M^2_{\pi\pi}$ to s_{γ^*}. All three plots are evaluated from MonteCarlo (PHOKHARA-Ω).

trigger and the vertex efficiency are evaluated directly on a $\pi^+\pi^-\gamma$ sample. In all the three cases however a set of cuts will be applied in order to clean the sample as much as possible. These cuts are chosen in a way not to introduce any bias in the selected sample, and in case some small ones are introduced their effect is taken into account in their systematic error. As mentioned above an *effective global efficiency* by MonteCarlo will be used to obtain the final spectrum. For all three cases we compare the efficiency evaluated by MonteCarlo with the one obtained by data and we correct the *effective global efficiency* accordingly.

5.1.1 The trigger efficiency

During the data acquisition of the sample that has been used in the present analysis, only the calorimeter trigger was used. As said in 2.2.3 an event to be acquired has to fire at least two trigger sectors. They have to be located either both in the barrel, or in the two endcaps or one in the barrel and the other in one of the endcaps.

We use directly $\pi^+\pi^-\gamma$ events for the evaluation of the trigger efficiency with both pions and photons at large polar angles and at least one photon with an energy above 40 MeV. The events have to pass all the *standard analysis* cuts, to obtain a clean sample of $\pi^+\pi^-\gamma$. Since the events are detected at large angles the two endcaps are not involved. We have checked that selecting events with the polar angles of the tracks in the range 50^o-130^o,

the fraction of events that fire clusters in the endcaps due to the track bending is on the sub-per-mil level.

The strategy for the evaluation of the trigger efficiency of the entire event, is in a first step to estimate the trigger efficiency of a single particle. Once evaluated the single particle trigger efficiency, we can combine them to obtain the efficiency for the entire event.

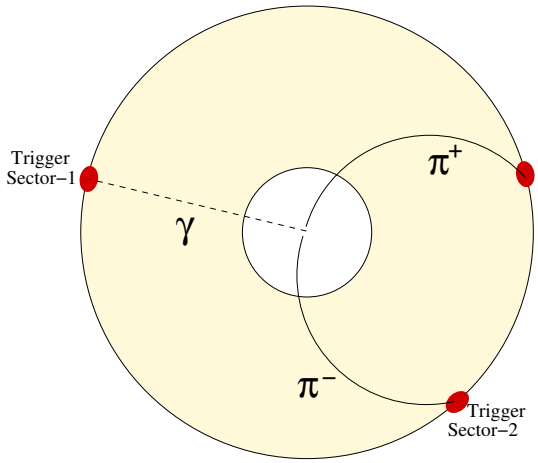

Figure 5.2: Sketch of the method for the evaluation of the trigger efficiency: a π^- and a γ are shown triggering the event, giving us the possibility to look for the trigger sector fired from the π^+.

The final state is made out of three particles, π^+, π^- and γ; we use two of them in order to obtain an unbiased sample for the third. For example, to evaluate the efficiency for the π^+, we look at a sample in which the event has been triggered by the π^- and the γ. In this sub-sample we check whether one or more trigger sectors are fired by the π^+. A sketch is presented in fig. 5.2, where a π^- and a γ have fired one trigger sector respectively. The event is therefore triggered by them, and we can look in an unbiased way at the sector triggered by the π^+. The procedure is repeated using a MonteCarlo sample, in order to look for differences with respect to data. The study has been done with $\sim$40 pb^{-1} of 2002 data and $\sim$50 pb^{-1} of MonteCarlo. The probability that one single particle fires at least one trigger sector (under the condition that the other two have triggered the event) is presented, both for data and MonteCarlo in fig. 5.3. We obtain an overall good agreement between the two samples, being the data efficiencies in some cases even higher that MonteCarlo. The different trigger response for π^+ and π^- is due to their different interaction in the electromagnetic calorimeter.

The same comparison has been done in bins of the tracks polar angle: the result is presented in fig. 5.4(a) for the π^+ and in fig. 5.4(b) for the γ. Again a good agreement between data and MonteCarlo is found. From data we obtain an efficiency for the π^+ above 96% for $P(\pi^+)$ >270 MeV. Only in the very first bin, for $50^o < \theta_{\pi^+} < 60^o$ (and the complementary slice on the other side of the detector), the efficiency has a drop down to 80% for low momenta ($P(\pi^+)$ <250 MeV). This is due to the bending by the magnetic field of low momentum charged particles towards the intersection barrel-endcaps , a less efficient region.

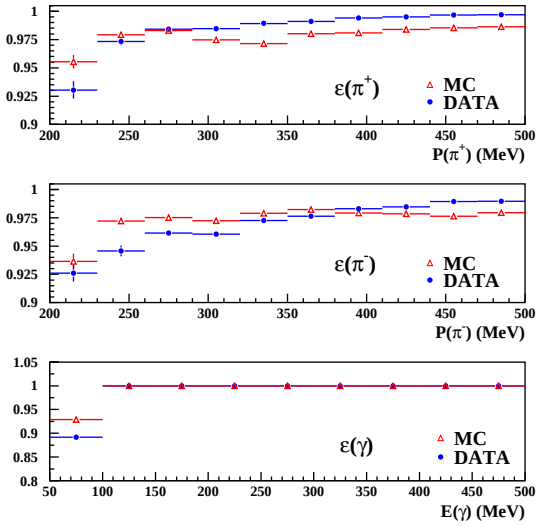

Figure 5.3: Probability that a third single particle π^+, π^- and γ has fired at least one trigger sector, if the other two have triggered the event, both from data (close blue circles) and MonteCarlo (open red triangles).

For the photon this study confirms that the trigger efficiency is always above 99%, in each angular region.

In order to obtain the trigger event efficiency, we combine the single particle efficiencies of fig. 5.3. For the charged particles this probability is never below 96% for momenta bigger than 270 MeV, while for the photon it is above 99% in almost the whole range. We can conclude as a very conservative estimate that the individual probabilities for π^+, π^- and γ are above 95%. Applying binomial statistics, we find that the probability that two out of three particles with probabilities bigger than 95% each, fail is below 0.1%. This estimate is even conservative, since for each of the three particles the trigger probability is higher than 95% in most of the range. Only for very low energy photons and low momenta pions the individual probabilities are lower, but the dynamics of the event makes this combination extremely unlikely. From a MonteCarlo simulation we have estimated that the probability to have simultaneously both pions with $P(\pi^{\pm})$ <250 MeV and the photon with $E(\gamma)$ <200 MeV is at the sub-per-mil level, i.e. negligible.

We can conclude that the trigger inefficiency for $\pi^+\pi^-\gamma$ events at large polar photon angle is below 10^{-3}. No correction on the final spectrum for the trigger is therefore required. The negligible inefficiency of the trigger selection on the data is due to the use of a third level of trigger (see §2.2.3), which was absent in 2001. This recovers almost all the signal events lost due to the cosmic ray veto.

5.1.2 The tracking efficiency

As for the trigger efficiency, the strategy is to evaluate firstly the single track efficiencies, and to combine them in a second step to get the tracking efficiency for the whole event.

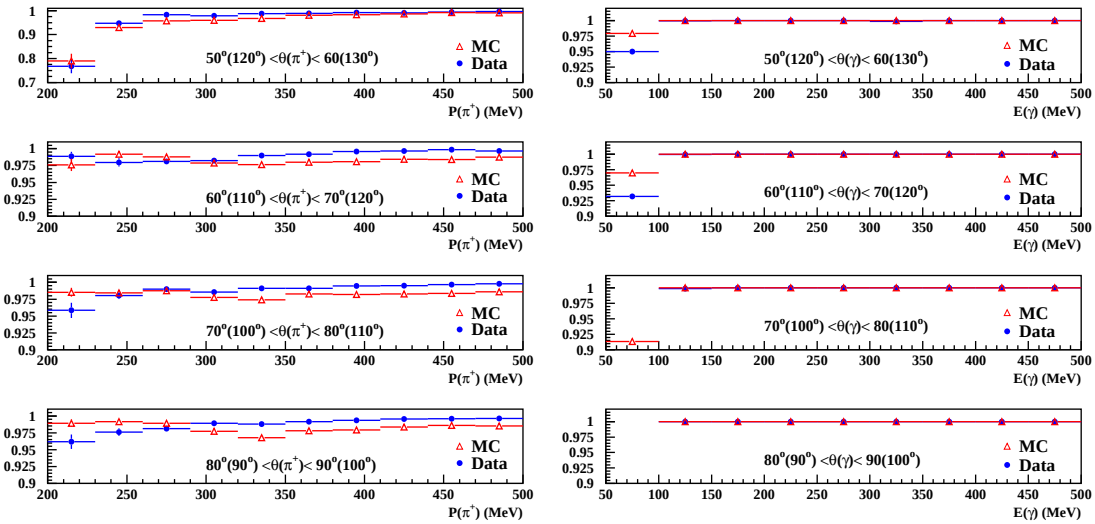

(a) (b)

Figure 5.4: Probability that the π^+ (a) and the γ (b) fires at least one trigger sector. The probability is shown both for data (closed blue circles) and MonteCarlo (open red triangles).

For the evaluation of the single track efficiency, a control sample of $\pi^+\pi^-\pi^0$ has been selected, in which only one track is required. Then we look for the presence of a second track, the so-called *test track*. The first part of the present paragraph describes the selection of the control sample, in the second one we derive the tracking efficiency using such a sample. The kinematic fit described in §4.2.1 is used for the $\pi^+\pi^-\pi^0$ selection. It is applied on a sample of data sample of $\sim$2 pb^{-1} (the cross section of the decay $\phi \to \pi^+\pi^-\pi^0$ is 480 nb). This sample is composed by runs taken in different periods of 2002, in order to take into account eventual variations of the run conditions. Since we explicitly require only one track (called *tagging track* in the following), we compute the missing momentum as an input for the kinematic fit using the momentum of the *tagging track* and the momenta of the two photons from the π^0 decay. The sketch of fig. 5.5 represents the topology of the events that we want to select. The fit is performed only if both the *tagging track* and the missing momentum have a polar angle between 40^o and 140^o, while the two photons are required to be detected either in the barrel or in the endcaps of the calorimeter (between 21^o and 159^o); only events with $\chi^2_{\pi\pi\pi}$ <5 are accepted in order to have a very clean sample of $\pi^+\pi^-\pi^0$ events. Since this efficiency is used to correct the final spectrum, exactly the same cuts which are asked for in the *standard analysis* have to be applied also here. The set of these cuts is listed below:

- ρ_{FH} >50 cm in order not to accept tracks originating far away from the interaction point;
- ρ_{PCA} <8 cm and $|z_{PCA}|$ <12 cm: a sizable fraction of tracks which have been split

during the tracking algorithm have the Point of Closest Approach (PCA) outside this cylinder. The real length is short in such a case and for this reason the procedure of extrapolation works less precisely;

- association of the *tagging track* with the calorimeter clusters, since this request in the *standard analysis* is done at the level of the particle ID;
- $|p_z|$ >90 MeV or p_T >160 MeV, as in the standard analysis to reject low momenta tracks which spiralize within the drift chamber.

In the standard analysis the cut on $|p_z|$ >90 MeV and p_T >160 MeV is applied to both tracks. For the tracking efficiency evaluation we also apply it to the missing momentum, which is supposed to have the same momentum as the *test track*, if this latter exists. Demanding the cuts mentioned above is not enough to clean completely the sample from background.

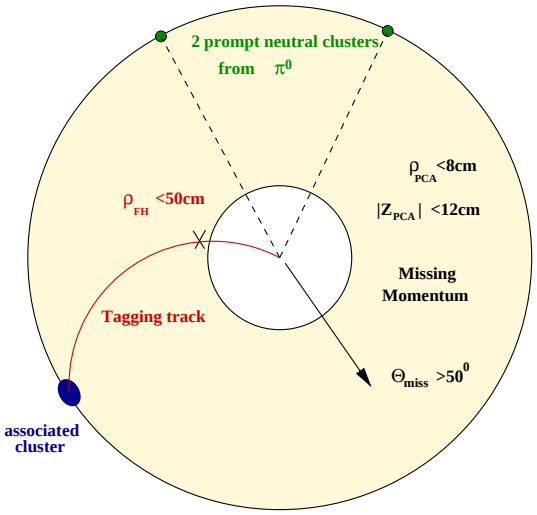

Figure 5.5: Scheme of the selection of the data sample used to evaluate the tracking efficiency.

We then apply two further cuts in order to arrive at a background-free sample of $\pi^+\pi^-\pi^0$ events. These cuts must be chosen not to introduce a bias to the tracking efficiency. In the following such cuts are listed:

- the maximum difference between the invariant mass of the two photons before the fit and the mass of the π^0 has to be 12 MeV: $|M_{inv}(\gamma\gamma) - m_{\pi^0} < |12$ MeV. The reason for this cut is that the 3π-fit works in this case with only one track, instead of two, and the errors on the missing momentum are less rigid than the ones for the detected track. Therefore in some cases the fit can converge and give a good value of $\chi^2_{\pi\pi\pi}$ even if the event is not a clear $\pi^+\pi^-\pi^0$. The events cut out by this request (few percent of the sample) have one of the two photon at low energy. The error on the z component of the photon momentum is energy dependent ($\sim 1/E$) and the lower is the energy, the worse is its determination;

- cut in the plane $E_{EmC}/|\vec{p}|$ vs.β: a part of the events with a good $\chi^2_{\pi\pi\pi}$ are radiative Bhabha events. The likelihood particle ID which is used in the standard analysis cannot be used, since it requires the existence of a vertex, implying therefore the presence of two tracks. The cross section of Bhabha is so high that the probability that some of these events survive the full chain of cuts is non zero. In order to reject them we profit from the fact that β and the ratio $E_{EmC}/|\vec{p}|$ (with E_{EmC} the energy of the most energetic cluster associated to the track and $|\vec{p}|$ the momentum of the track measured by the drift chamber) are peaked at 1 for an electron, while it is smaller and broader for a pion. In fig. 5.6 the distribution of events in the plane $E_{EmC}|\vec{p}|/$ vs. β is shown, after the cuts described above: one can see that for the data the region with β >0.9 and $E_{EmC}/|\vec{p}|$ around 1 is populated even having applied a very tight cut in $\chi^2_{\pi\pi\pi}$. These events are rejected by the cut whose shape is also shown.

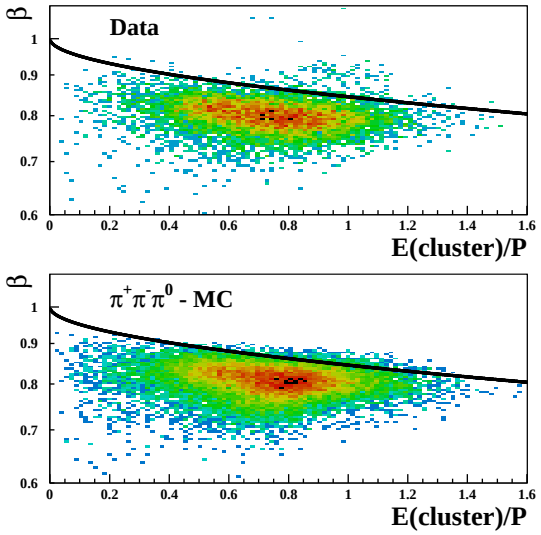

Figure 5.6: Distribution of the event in the plane $E_{EmC}/|\vec{p}|$ vs. β for the *tagging track*, for data (upper plot) and $\pi^+\pi^-\pi^0$ MonteCarlo (lower plot). The shape of the cut applied on the data sample is also shown.

At the end of this selection, the data sample is very clean, as can be seen in fig. 5.7(a), where the momentum and the angle of the *tagging track* is plotted and compared to the simulation, as well as the missing momentum and the missing angle. The comparison data-MonteCarlo shows good agreement between the two samples.

The next step is to look for the *test track* in the selected sample. In the case the *test track* exists, we expect that it has a momentum close to the missing momentum, unless further effects, e.g. pion decay, hadronic interaction in the drift chamber walls, play a role. We have checked for this effect, by plotting the difference between the momentum (the angle) of the *test track* and the missing momentum (missing angle). Fig. 5.7(b) shows that the two differences are well peaked around zero, both for data and MonteCarlo, and that the agreement data-MonteCarlo is excellent, even in the tails.

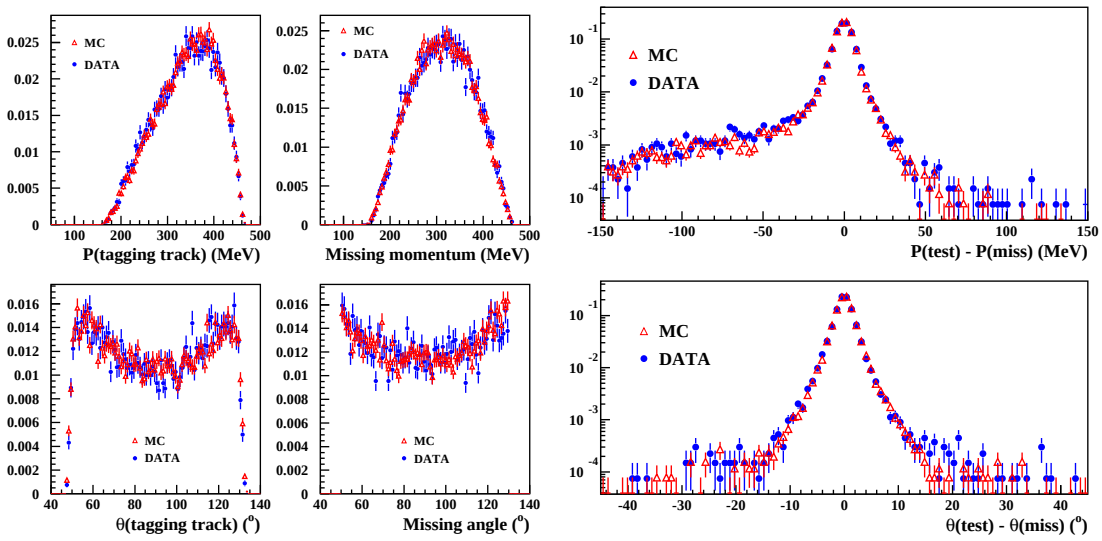

(a) (b)

Figure 5.7: (a) Comparison data-MonteCarlo of the momentum and of the polar angle of the *tagging track* and the missing momentum. The two samples are compared after the whole set of cuts described in the text. (b) Difference, if the *test track* exists, between the momentum (angle in the lower plot) of the *test track* and missing momentum (angle). Data and MonteCarlo are superimposed.

The *test track*, if existing, has to satisfy the same requests that it has to fulfill in the *standard analysis*:

- ρ_{FH} >50 cm, ρ_{PCA} <8 cm, $|z|_{PCA}$ <12 cm;
- opposite curvature with respect to the one of the *tagging track*;
- $50^o < \theta_{test} < 130^o$.

The tracking efficiency has been evaluated as a function of the missing momentum and in slices of the polar angle and compared with MonteCarlo. In fig. 5.8(a) the result is presented. The efficiency is higher than 95% in the whole range of momentum and for each bin of polar angle and the agreement data-MonteCarlo is at the per-mil level. For each slice of the polar angle the double ratio of the efficiency from data and MonteCarlo has been built: one sees from fig. 5.8(b) that there is no dependance on the polar angle. By fitting the ratios with a straight line one observes that the agreement between data and MonteCarlo is good, varying between 0.3% and 0.5%. In fig. 5.8(b) the results of the fits and the values of χ^2 are reported for each slice. The total single track efficiency as a function of missing momentum and missing angle are presented in 5.9(a), inclusively in $P(miss)$ (upper plot) and in $\theta(miss)$ (lower plot). The lower plot confirms the result obtained in the study in the different angular region: the efficiency as a function of θ_{miss} is flat both for data and MonteCarlo, and so is their ratio. The efficiency as a function of $P(miss)$ varies between

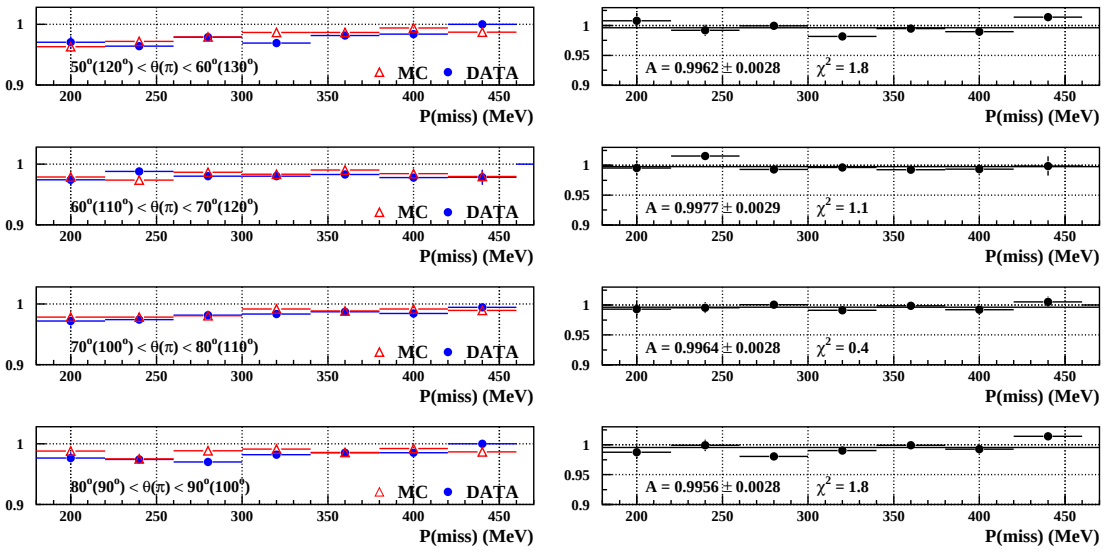

(a) (b)

Figure 5.8: Single track efficiency as a function of the missing momentum in slices of the polar angle for data (full blue circles) and MonteCarlo (red open triangles). (b) Ratio data-MonteCarlo of the curves in (a). For each angular range a fit with a straight line has been performed and the result of the fit as well as the value of the χ^2 of the fit are reported.

97% at low momenta up to 99% at high momenta; however, MonteCarlo follows pretty well the behaviour of the data, as their ratio shows in fig. 5.9(b) in which a flat behaviour with a difference of 0.4% is observed.

We have performed a detailed study on the nature of the inefficient events. The main causes for the inefficiency are the splitting of the tracks and the pion decay within the beam pipe. In the first case the track is split close to the beam pipe fulfilling the request ρ_{FH} <50 cm, but the mother track is so short that the procedure of extrapolation to the point of closest approach gives a poor result. Therefore these tracks are cut from the requests of the PCA for the *test track*. In the second case, the pions decay within the beam pipe $\pi^{\pm} \to \mu^{\pm}\nu_{\mu}$. These are part of the events in the tail of fig. 5.7(a) and fig. 5.7(b), being the momenta of muons lower than the missing momentum, as well as its polar angle is different from the missing angle. The track from the muon does not point into the direction of the interaction point and even if it is close to it, it does not fulfill the cuts on ρ_{PCA} and/or on $|z|_{PCA}$.

The momentum distribution of a pion from $\phi \to \pi^+\pi^-\pi^0$ events ends at ∼450 MeV, due to the kinematics of the decay , while it reaches ∼550 MeV for the reaction $e^+e^- \to \pi^+\pi^-\gamma$ (see fig. 5.10). In the *small angle* analysis in order to cover the high momenta region, a sample of $e^+e^- \to \pi^+\pi^-$ has been selected, and the efficiency obtained from such a sample has been evaluated by a comparison data-MonteCarlo. Since it is a two-body decay the energy of the emerging $\pi^{\pm}$ is fixed at $M_{\phi}/2$ and consequently the momentum of the two will be equal to 490.2 MeV, allowing to determine the single tracking efficiency up to 490

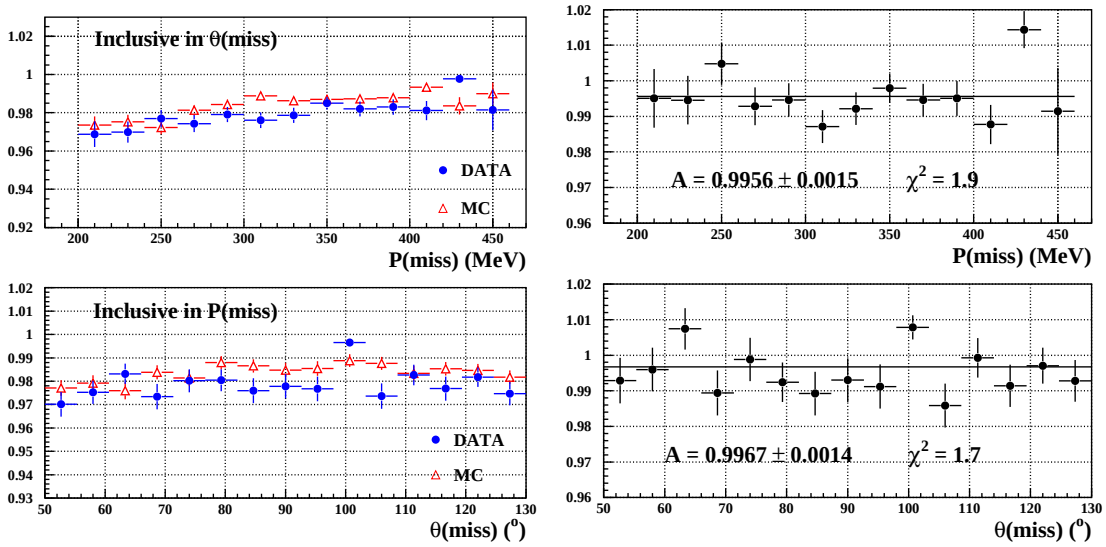

(a) (b)

Figure 5.9: (a) Single track efficiency as a function of the missing momentum integrated over the polar angles for data (full blue circles) and MonteCarlo (red open triangles). (b) Ratio data-MonteCarlo of the curves in (a). A fit with a straight line has been performed and the result of the fit as well as the value of its χ^2 are reported.

MeV. The update of the *small angle* analysis (see §7) with the 2002 data uses the same method. In both cases the single track efficiency in the last bin (at 490 MeV) has the same average value as in the whole momentum range. This has been checked with different slices of the polar angle also. The single particle efficiency that we have evaluated in the *large angle* analysis between 200 and 450 MeV, is in perfect agreement with the one obtained in the *small angle* analysis (with 2002 data), we have no reason to suppose that the ratio of the efficiency data-MonteCarlo has a drop or a rise for momenta above 450 MeV. Therefore we prolong the fit of fig. 5.9(a) up to 500 MeV, covering the whole momentum range of interest.

We need the correction expressed as a function of $M^2_{\pi\pi}$; since no dependence of the difference data-MonteCarlo on momentum and polar angles has been found, we can apply a global correction of 0.4% in the $M^2_{\pi\pi}$ spectrum.

In order to evaluate the systematic error for the tracking efficiency, we shift systematically each selection cut, independently from the others. For each fixed set of cuts, the tracking efficiency is evaluated both for data and MonteCarlo and their ratio is computed as

$$R_{\epsilon(trk)} = \frac{\epsilon^{Data}(trk)}{\epsilon^{MC}(trk)} \tag{5.2}$$

and fitted with a straight line. In fig. 5.11(a) and fig. 5.11(b), the values of the fits are plotted as a function of the variable the value of which has been moved. The other variables

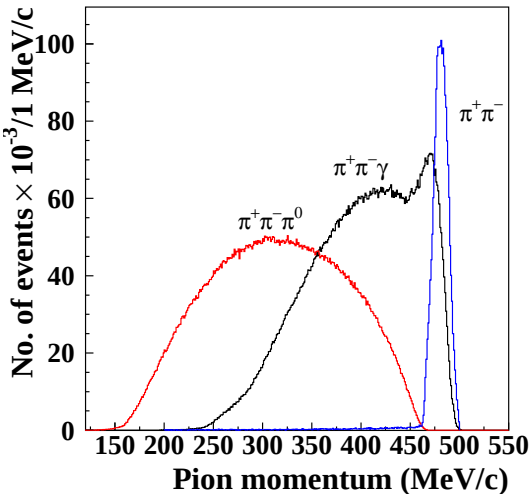

Figure 5.10: Pion momentum distribution for $\pi^+\pi^-\pi^0$, $\pi^+\pi^-$ and signal events.

are not changed. Moving the cut on $M_{inv}(\gamma\gamma)$ we see no effect in the difference data-MonteCarlo, while we observe a decrease of ∼0.2% when we shift the cut of $\chi^2_{\pi\pi\pi}$ toward higher values. This is due to the fact that a tighter cut on $\chi^2_{\pi\pi\pi}$ cleans the control sample from background, which enters when we start widening the cut. We have also studied the ratio data-MonteCarlo directly for the *test track* using other variables and we see small variations of the tracking efficiency. Moving systematically around the values $|z_{PCA}|$=12 cm we see a total variation of ∼0.2%; the same variation of ∼0.2% is observed moving the cut of ρ_{PCA}, while the effect is only ∼0.1% for the shift of ρ_{FH}. Since $|z_{PCA}|$ and ρ_{PCA} are correlated, being two coordinates of the same point, we take into account the error of 0.2% only once, summing it up in quadrature with the other two contributions giving a total systematic error of 0.3%.

5.1.3 Vertex efficiency

As for the two previous efficiencies, the ones for trigger and for tracking, also for the vertex we evaluate the efficiency for data and MonteCarlo and we correct the data spectrum for the difference between the two.

The vertex efficiency has been evaluated using directly $\pi^+\pi^-\gamma$ events. For each event we look for two *candidate* tracks, i.e. tracks whose origin is close to the IP. More precisely the *candidate* tracks have to have a point of closest approach (PCA) of the track fit extrapolation within the cylinder around the IP defined by $\rho_{PCA} = \sqrt{x^2_{PCA} + y^2_{PCA}}$ <8 cm and $|z_{PCA}|$ <12 cm. The radius ρ_{FH} of the first hit in the transverse plane of the drift chamber has to be ρ_{FH} <50 cm. Each *candidate track* has to be associated to one (or more) EmC cluster. The requests for the two *candidate tracks* are shown in fig. 5.12. The association of the two tracks to the calorimeter cluster is present also in the analysis, being

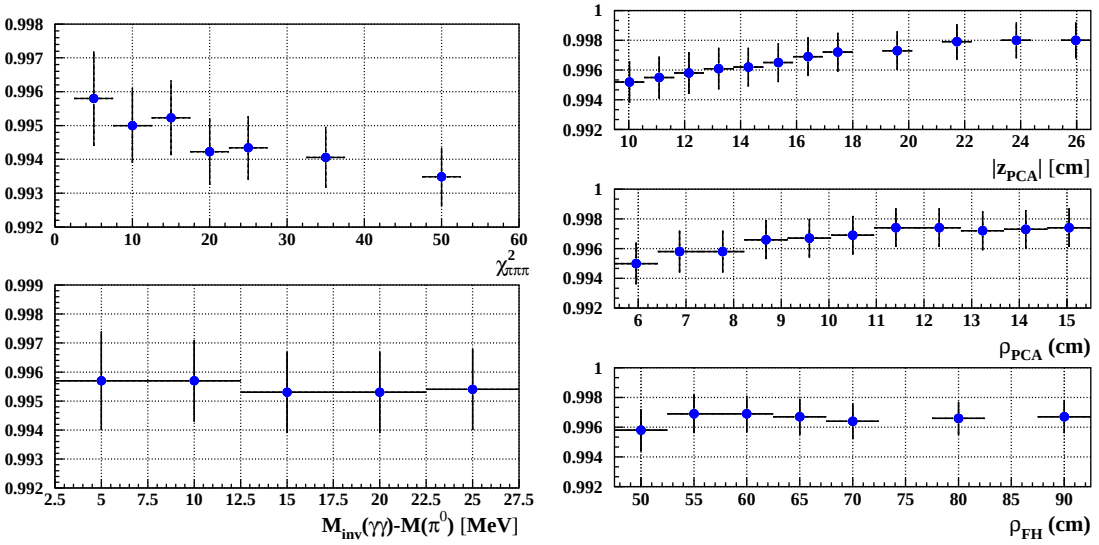

(a) (b)

Figure 5.11: Values of the fit of the ratio $R_{\epsilon(trk)}$ for different values of the selection cuts. In (a) the cut on the $\chi^2_{\pi\pi\pi}$ and the one on the invariant mass of the two photons have been systematically shifted; in (b) the position of the point of closest approach and the one in the transverse plane of the first hit have been moved.

one of the requirements of the particle ID (for the pions-electrons separation). As in the

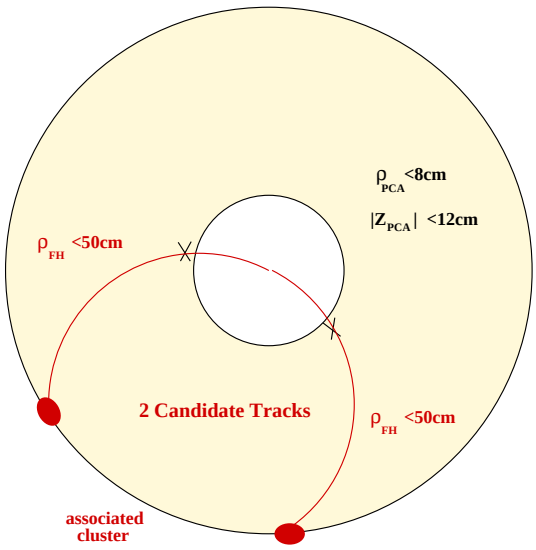

Figure 5.12: Sketch of the request for the *candidate tracks*, used to evaluate the vertex efficiency.

tracking efficiency evaluation, we cannot use the particle ID, since it requires a vertex. The same cut in the plane $E_{EmC}/|\vec{p}|$ vs.β for the $\pi - e$ separation described in §5.1.2 is applied, as shown in fig. 5.13(a) and fig. 5.13(b). In the data distribution Bhabha events are clearly distinguishable in the concentration of events centered at $\beta \sim 1$ and $E_{EmC}/|\vec{p}| \sim 1$.

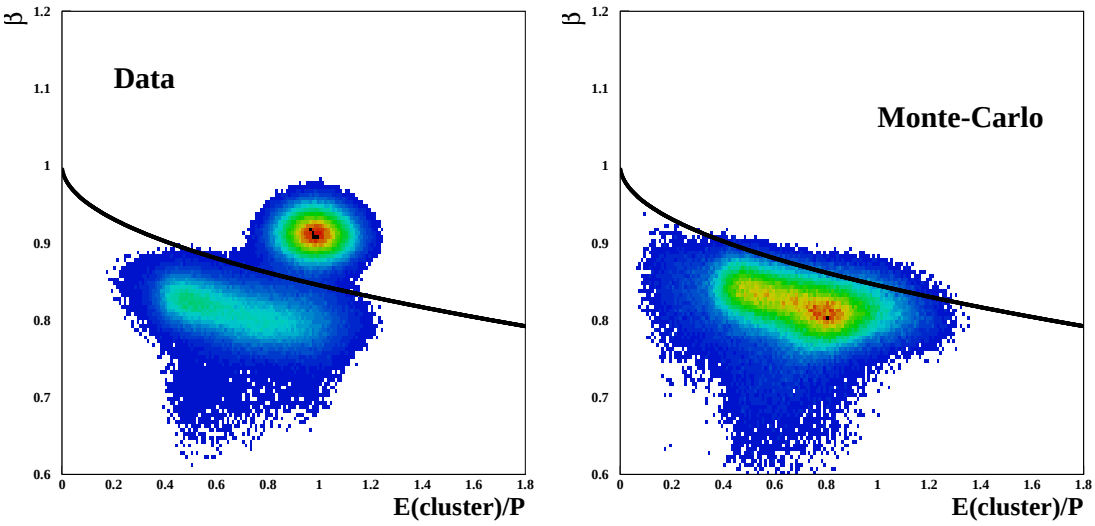

(a) (b)

Figure 5.13: Distribution of events in the plane $E/|\vec{p}|$ vs. β for *candidate* tracks, for data in (a) and MonteCarlo $\pi^+\pi^-\gamma$ simulation in (b). The cut to remove Bhabha events is also shown as.

The whole standard analysis (except the vertex requirement and the $\chi^2_{\pi\pi\pi}$) is repeated to remove the background from the sample. We ask for two tracks (with the usual request on p_T and $|P_z|$) without requiring that the two have formed a vertex. The trackmass variable is built with two tracks (no need of a vertex) and the same for the Ω angle. There is however a difference in the use of Ω with respect to the standard analysis: in order to remove completely the background from $\pi^+\pi^-\pi^0$ contamination, we apply a very rigid cut here ($\Omega < 1^o$).

The procedure is applied both to data and MonteCarlo: the fig. 5.14(a) shows the comparison between them for the mass spectrum. The agreement between the two spectra indicates that the procedure provides a clean sample of $\pi^+\pi^-\gamma$ events. We determine the vertex efficiency by looking if two *candidate* tracks are connected by one vertex within the cylinder $\rho_{vtx} = \sqrt{x^2_{vtx} + y^2_{vtx}} < 8$ cm $|z_{vtx}| <$12 cm. The events found to have one vertex in the cylinder, are normalized to the sample of events having at least two *candidate tracks* (the sample used for the spectrum of fig. 5.14(a)). In this way we obtain the probability that we find in the event a vertex. This probability is plotted in fig. 5.14(b) (upper plot) both for data (in blue) and MonteCarlo (in red). For both samples it is higher than 99%; in the lower plot the ratio of the two $R_{\epsilon(vtx)} = \epsilon^{data}_{vtx}/\epsilon^{MC}_{vtx}$ is reported. It is flat in $M^2_{\pi\pi}$ and by fitting the ratio $R_{\epsilon(vtx)}$ with a straight line, we obtain a difference data-MonteCarlo of 0.3%. This difference is the value we have to correct the final mass spectrum for.

The systematic error on the vertex efficiency is evaluated by shifting systematically the single cuts ($\rho_{PCA}, |z_{PCA}|$ and Ω) independently from each other, and by looking at the variation of the ratio of the efficiency $R_{\epsilon(vtx)}$. We take as a systematic error the difference

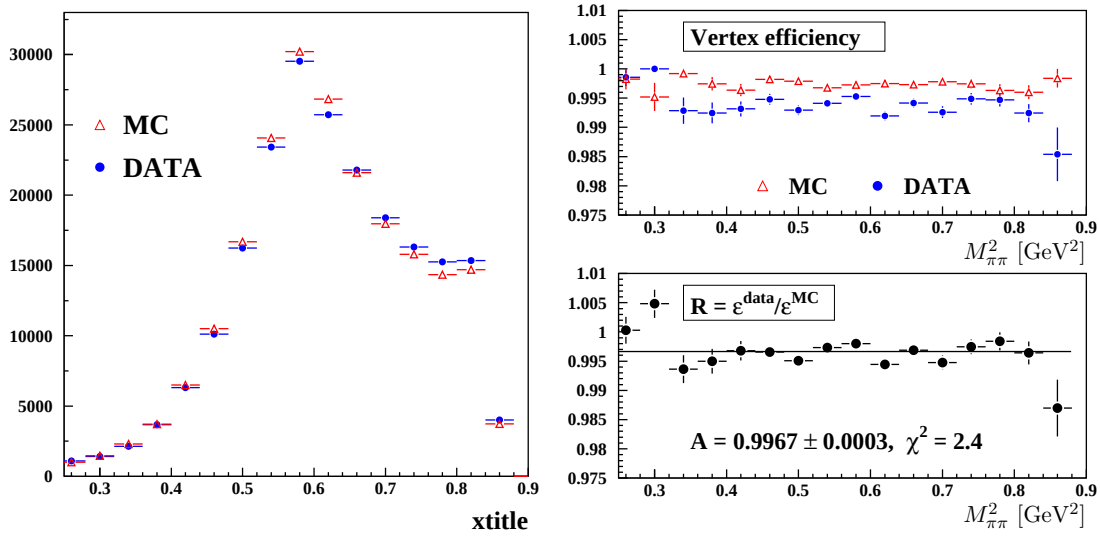

(a) (b)

Figure 5.14: (a) Mass distribution for data (in blue) and MonteCarlo (in red) for the $\pi^+\pi^-\gamma$ sample used for looking at a vertex. (b) Probability to find a vertex in a sample of $\pi^+\pi^-\gamma$ at large polar angles evaluated both with data and with MonteCarlo (upper plot). The ratio $R = \epsilon^{data}_{vtx}/\epsilon^{MC}_{vtx}$ is plotted in the lower plot.

between the minimum and the maximum value obtained for $R_{\epsilon(vtx)}$, which has an average value of 0.2%.

5.2 Further efficiency evaluations

5.2.1 Offline reconstruction filter efficiency

An offline filter identifies and rejects background events after the calorimeter reconstruction in order to save CPU time since the rejected events do not pass through the time-consuming track fitting and pattern recognition algorithms. Events recognized by the filter as background are saved with a downscaled factor of 1/64 in a separated data stream. The efficiency of the filter, evaluated using such a sample, is shown in fig. 5.15(a); the inefficiency on the signal is 0.3% on the whole range of interest. Details of the offline filter can be found in [81]. We would like to stress that the filter has undergone major modifications from the version used in the *small angle* analysis (2001 data) to the actual one. The new version, used in the present analysis, is less sensistive to the run condition of the machine. This improvement, together with the better quality of 2002 data with respect the sample collected in 2001, makes the systematic error on the filter less than 0.1%, while it was the dominant one (0.6%) in the *small angle* analysis (see tab. 3.1).

5.2.2 Particle ID efficiency

The particle ID, which does the $\pi - e$ separation, is very efficient for pions. This has been evaluated with data control samples of $\pi^+\pi^-\pi^0$ and $\pi^+\pi^-\gamma$ events. Using one track as the *tagging track* and testing the other with respect to the particle ID, an efficiency for one single (pion) track being identified as a pion is $> 98\%$ [72]. The single track efficiency is evaluated as a function of p_π and θ_π. The kinematics of the event simulated by MonteCarlo is used to combine the single track efficiencies in order to evaluate the efficiency for the full event as a function of $M^2_{\pi\pi}$. Since in the analysis the selection criteria are such that both charged particles have to be identified as pions, the inefficiency on the signal is not negligible, mainly in the low mass region. In fig. 5.15(b) both the intrinsic particle ID inefficiency is shown (in open black circles) and the one obtained by including the track-to-cluster association efficiency (full red points). The big drop below 0.6 GeV^2 is due to the fact that the momentum distribution of large angle events decreases below 150 MeV and at this value the probability that a particle is associated to a calorimeter cluster is $\sim$90%. Since we ask in the selection that the two charged tracks are associated with the calorimeter clusters, the final spectrum is corrected for the red curve. The systematic error associated to the particle ID is 0.3% in our range of interest.

5.2.3 Calorimeter efficiency for photons

The photon efficiency was measured in [82] for a sample of $\pi^+\pi^-\pi^0$ events, selected from data by asking for events with two opposite charged tracks from the IP, having the missing mass around the mass of π^0. One of the two photons is selected as the *tagging photon*, with the expected energy and time. The efficiency is evaluated by counting the events with a photon matching the cone around the expected direction. Photon counting is performed in bins of the polar angle and of the expected energy. As in the cases of the tracking and the vertex efficiency, what is relevant for our purposes is the ratio between the efficiency observed in data and in MonteCarlo. Such a ratio has a drop of some per-cent for low energy photons (i.e. at high $M^2_{\pi\pi}$), which starts above 0.9 GeV^2. Our region of interest ends at 0.85 GeV^2 (corresponding to a photon energy of 920 MeV). This means that we cover fully the range where we do not need any correction for the photon detection efficiency, which is well described by the MonteCarlo simulation.

5.3 Systematic errors evaluation

As mentioned at the beginning of the chapter, all efficiencies for the cuts applied to reject background are evaluated by MonteCarlo. They are automatically included in the *effective global efficiency*. Here we look for systematic differences between data and MonteCarlo for each individual analysis cut. If found we take such differencies as the systematic error for that specific cut. In the following sections, the procedure for each single cut is described.

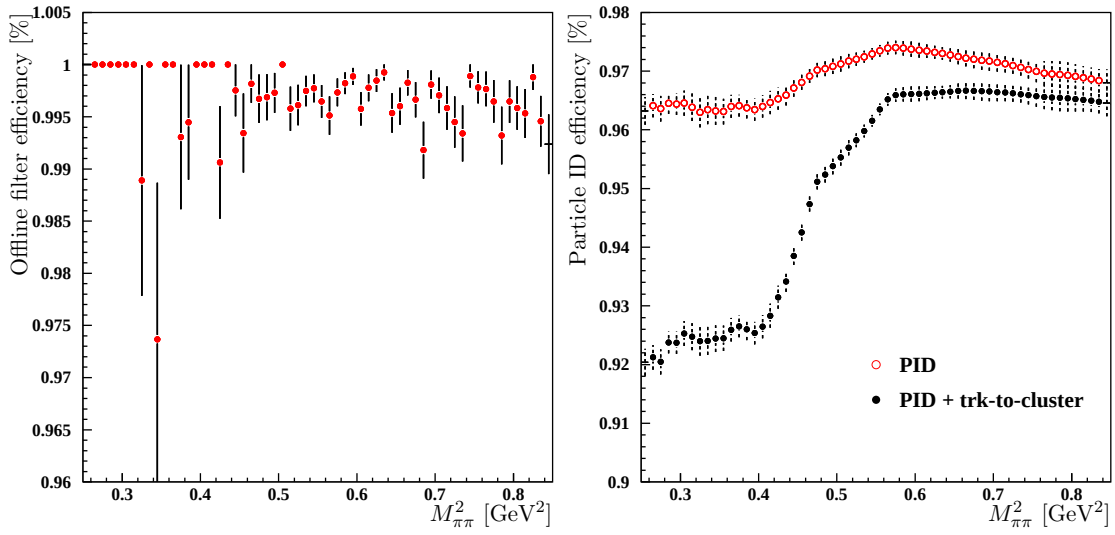

(a) (b)

Figure 5.15: (a) Efficiency of the offline filter reconstruction for $\pi^+\pi^-\gamma$ events. (b) Efficiency of the particle ID for $\pi^+\pi^-\gamma$ events at large angles, if both tracks are identified as pions. Open circles are obtained combining the single track selection efficiency of the particle ID only, full circles include also the track-to-cluster efficiency. The plot is taken from [73].

There is however a common strategy which applies to each cut studied, which can be summarized as follows:

- to shift systematically one single cut with respect its nominal value, i.e. the value fixed in the analysis, leaving unchanged all the others;
- to run the full selection on data, $\pi^+\pi^-\gamma$, $\mu^+\mu^-\gamma$ and $\pi^+\pi^-\pi^0$ MonteCarlo;
- to subtract the residual $\mu^+\mu^-\gamma$ and $\pi^+\pi^-\pi^0$ background from the data sample and build the ratio between data and $\pi^+\pi^-\gamma$ MonteCarlo;
- to normalize such a ratio to the ratio between data and MonteCarlo obtained if one applies the standard selection (all the cuts fixed at their nominal value):

$$R_{cut}(M^2_{\pi\pi}) = \frac{N(data)/N(MC)|_{shifted\ cut}}{N(data)/N(MC)|_{nominal\ cuts}}(M^2_{\pi\pi}) \tag{5.3}$$

The double ratio $R_{cut}(M^2_{\pi\pi})$, which is generally flat, is fitted with a straight line. The variation of the values of the fits, as a function of the shifts of the cut under study, gives us the systematic error on that specific cut.

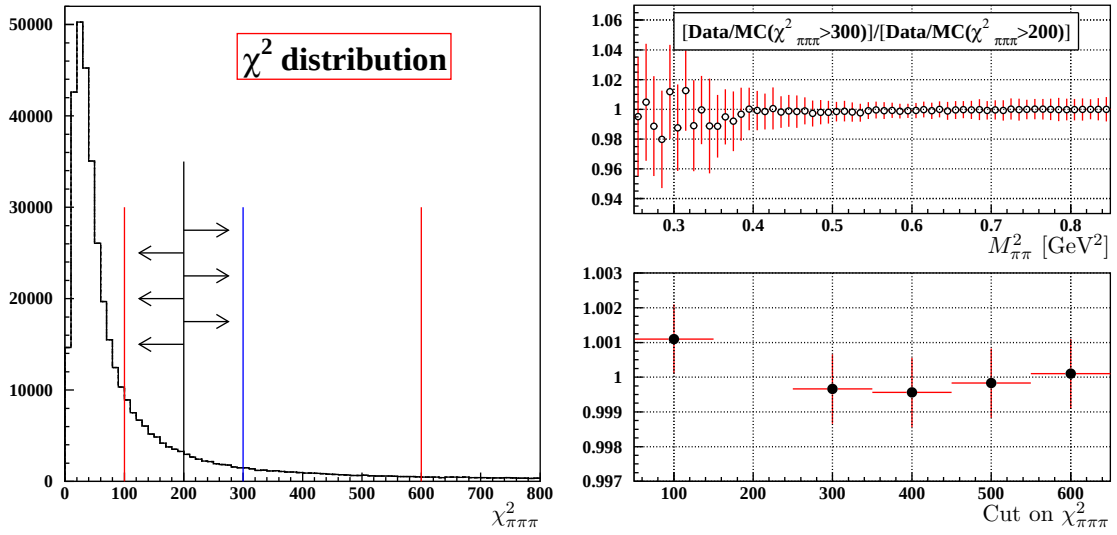

(a) (b)

Figure 5.16: (a) Shift of the cut on $\chi^2_{\pi\pi\pi}$ in the procedure to evaluate the systematic error introduced by this cut. The black line shows the nominal cut at 200, the two red lines the two extremes of the variation and the blue one intermediate step. (b) Upper plot: example of $R_{\chi^2_{\pi\pi\pi}}$ for $\chi^2_{\pi\pi\pi}$=300. Lower plot: effects of the shift of the cut on $\chi^2_{\pi\pi\pi}$ on $R_{\chi^2_{\pi\pi\pi}}$.

5.3.1 Cut on $\chi^2_{\pi\pi\pi}$

Particular attention has been paid to find a compromise between the rejection power of the cut on $\chi^2_{\pi\pi\pi}$ and the inefficiency on the signal (see §4.2.1). The reason is the difficulty to evaluate possible systematic errors of this cut on the data sample. We remind the reader that fixing the cut on $\chi^2_{\pi\pi\pi}$ at 200, the inefficiency (evaluated from MonteCarlo) of the signal is at most 1% (see fig. 4.4(a)).

In order to estimate the systematic error introduced by this cut, we have evaluated the double ratio $R_{\chi^2_{\pi\pi\pi}}$ moving the cut on $\chi^2_{\pi\pi\pi}$ between 100 and 600, in steps of 100. In fig. 5.16(a) the shifting of the cut is shown: the nominal cut at 200 (black line) is superimposed to the $\chi^2_{\pi\pi\pi}$ of a $\pi^+\pi^-\pi^0$ MonteCarlo. The double ratio $R_{\chi^2_{\pi\pi\pi}}$ is evaluated between the two red lines ($\chi^2_{\pi\pi\pi}$=100 and 600 respectively) in 6 steps, one example of which is given by the blue line ($\chi^2_{\pi\pi\pi}$=300) One example of the double ratio $R_{\chi^2_{\pi\pi\pi}}$ is shown in the upper plot of fig. 5.16(b); namely the ratio data-MonteCarlo for $\chi^2_{\pi\pi\pi}$ >300 normalized to the reference one ($\chi^2_{\pi\pi\pi}$=200). $R_{\chi^2_{\pi\pi\pi}}$ is completely flat above 0.4 GeV^2; below some discrepancies appear, hardly recognisable due to the poor statistics. In order to evaluate such an effect, we have fitted with a straight line corresponding to the several shifts on $\chi^2_{\pi\pi\pi}$ shown in fig. 5.16(a). The values of the fits are presented in the lower plot of fig. 5.16(b) as a function of the cut on $\chi^2_{\pi\pi\pi}$. Since an effect smaller than 0.2% is observed, we estimate that the cut on $\chi^2_{\pi\pi\pi}$ introduces a systematic error of 0.2%.

5.3.2 Cut on trackmass

The study of the systematic error of the trackmass cut is divided into three parts:

1. comparison between data and MonteCarlo of the trackmass distribution;
2. study of the resolution of the trackmass variable;
3. evaluation of the systematic error introduced by the trackmass cut.

The comparison between data and MonteCarlo of the trackmass distribution (point 1 in the list above) shows a very good agreement between the two. The plot (shown in fig. 5.17(a)) is obtained by running the full selection (except the trackmass cut) on data and MonteCarlo, subtracting the residual background from the data sample and by looking at the trackmass distribution. We observe some deviations only in the tails of the distribution, probably due to the limited description of the background by MonteCarlo. In the two next points we will quantify the effect that this small discrepancy has in the $M^2_{\pi\pi}$ spectrum.
A study of the resolution of the trackmass variable (point 2) has been performed with the aim of defining the range of variation of the m_{trk} cut in the evaluation of the systematic error. For each event of the MonteCarlo simulation we have looked at the difference between the *true* value of the trackmass and the reconstructed one. The distribution of this difference has been fitted with two gaussians, with the purpose to understand whether the variable has some not-gaussian tail. The fit is shown in fig. 5.17(b). From the fit we see that only less than 3% of the events requires a broader gaussian (with σ=13.3 MeV). All the rest is well described by a single core gaussian distribution centred at zero with a σ of 3.5 MeV. Given the small fraction of events which needs a second gaussian, we neglect them assuming that the shape of fig. 5.17(b) is well described by a single gaussian, whose σ represents the resolution of the trackmass variable.
We remind that the cut in m_{trk} (fig. 4.5) consists of

(i) a $M^2_{\pi\pi}$dependent curve which cleans from $\pi^+\pi^-\pi^0$ background that we will refer to as $f(m_{trk}, M^2_{\pi\pi})$ in the following;

(ii) a fixed cut m_{trk} >120 MeV to reject $\mu^+\mu^-\gamma$ events.

The possible effects from the two requests (i) and (ii) have been studied separately.
The procedure for estimating the systematic error for case (i) is shown in fig. 5.18(a): the curve $f(m_{trk}, M^2_{\pi\pi})$ (the one used in the selection of events is shown in black) is moved in steps of 1 MeV up to the maximum value of $\pm$4 MeV, corresponding to $sim1\sigma$ of the trackmass resolution. Two intermediate curves (corresponding to $\pm$1 MeV with respect the nominal black curve) are shown in blue in the zoom of the same figure. The double ratio $R_{m_{trk}}$ is evaluated for each step. One example of $R_{m_{trk}}$ is given in the upper plot of fig. 5.18(b) where the effect on the maximum variation in the trackmass ($f(m_{trk}, M^2_{\pi\pi} + 1\sigma$ corresponding to the upper red curve of fig. 5.18(a)) cut is shown. In order to quantify the

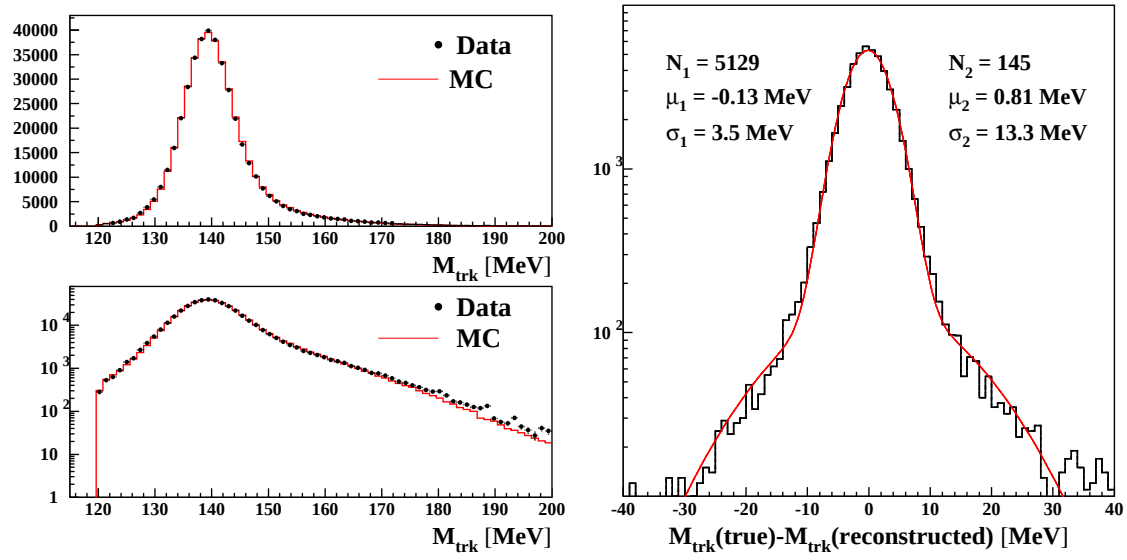

(a) (b)

Figure 5.17: (a) Trackmass distribution for data (black points) and MonteCarlo (red line). All the analysis cuts are applied and from data the background is subtracted. The distribution is shown both in linear (upper plot) and logarithmic scale (lower plot). (b) Resolution on the m_{trk} variable. The fit with two gaussian distributions is superimposed, and the parameters of the fit are shown.

small deviation from the one that we observe, each double ratio $R_{m_{trk}}$ is then fitted with a straight line. The results of the these fits are shown in the lower plot of fig. 5.18(b) as a function of the shifted cut in trackmass. From this plot we associate a systematic error of $\pm 0.2\%$ to the trackmass cut of case (i).

Now we describe the systematic error evaluation for case (ii). The agreement between data and MonteCarlo at $\sim$120 MeV is not as good as it is on the π-peak (fig. 5.17(a)). Looking closely in the region between 116 and 124 MeV (i.e. about $\pm 1\sigma$ around the cut) we find some discrepancies between data and MonteCarlo up to 5%. However this region contributes to less than 1% to the full sample; the systematic error therefore introduced by the cut is neglibible (5×10^{-4}).

We conclude then that the only contribution to the systematic error on the trackmass cut comes from the curve in the upper part of the plane m_{trk} vs. $M^2_{\pi\pi}$ and it is equal to 0.2%.

5.3.3 Cut on the Ω angle

As done for the trackmass cut, before evaluating the systematic error of the Ω-angle cut, we look at the comparison between data and MonteCarlo of the distribution, which is shown in fig. 5.19. All the analysis cuts have been applied except the Ω-cut and from data the residual background has been subtracted from data. The agreement is not excellent on the peak while the tail of the distribution (where the residual $\pi^+\pi^-\pi^0$ are concentrated) is nicely

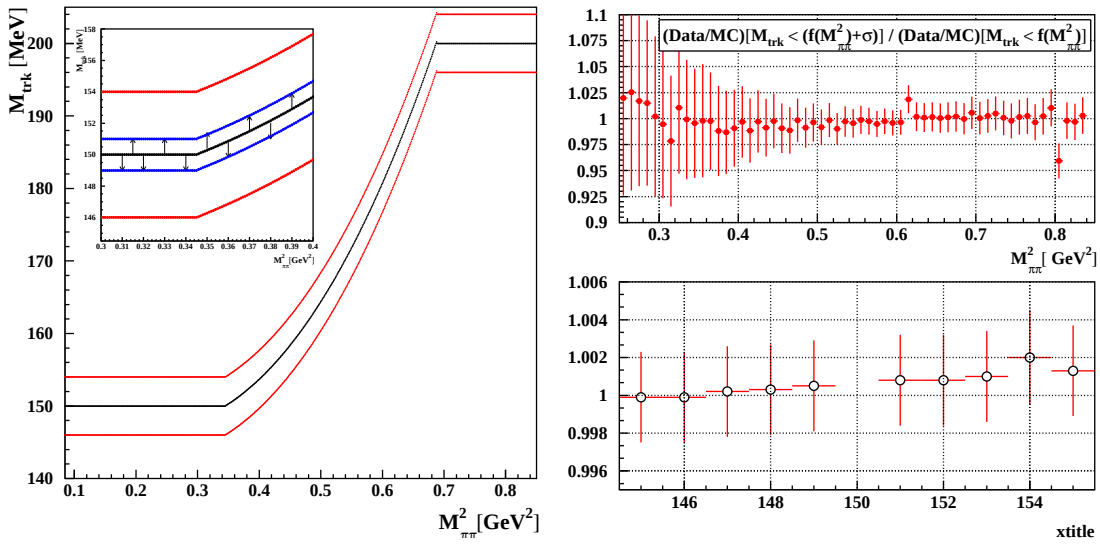

(a) (b)

Figure 5.18: (a) Systematic shift of the trackmass cut to evaluate the systematic error of the trackmass cut. The black line represents the nominal cut, the two red the maximun variation of the m_{trk} cut and blue lines two intermediate steps. (b) Upper plot: example of one double ratio $R_{m_{trk}}$. Lower plot: results of the fits of $R_{m_{trk}}$.

reproduced from MonteCarlo. All the checks done in order to explain such a discrepancy have excluded that it is due to background. Therefore we have concluded that the observed difference is due to some systematic tracking effect not fully understood. This argument justifies the choice of the Ω cut shown by the curve of fig. 4.7(b). A tighter could have been possible in principle, with a higher rejection power for $\pi^+\pi^-\pi^0$ events, but our choice minimizes the systematic effect introduced by the cut. In order to estimate the systematic error we have shifted the cut in Ω by half a degree as shown in the red curves of fig. 5.20(a). In the same plot the black curve indicates the cut on the Ω-angle applied in the analysis and in the insert the blue curves are two examples of the intermediate 1^o steps. For each step the double ratio R_Ω has been evaluated: from fig. 5.20(b), where two examples of R_Ω are shown, we see that there is no visible effect above 0.4 GeV^2. Even at low energies where there could be a systematic effect (hardly distinguishable from statistical fluctuation) the error is small: let us consider a 2% variation of the double ratio R_Ω between 0.25 and 0.4 GeV^2. The maximum inefficiency in this interval is 4% (see fig. 4.8), for a systematic error smaller than 0.1%. We conclude then that the systematic error introduced by the Ω-cut is $<$0.1% in the whole mass range.

5.3.4 Acceptance

As always in the cross section measurements the geoetrical acceptance efficiency is taken from MonteCarlo.

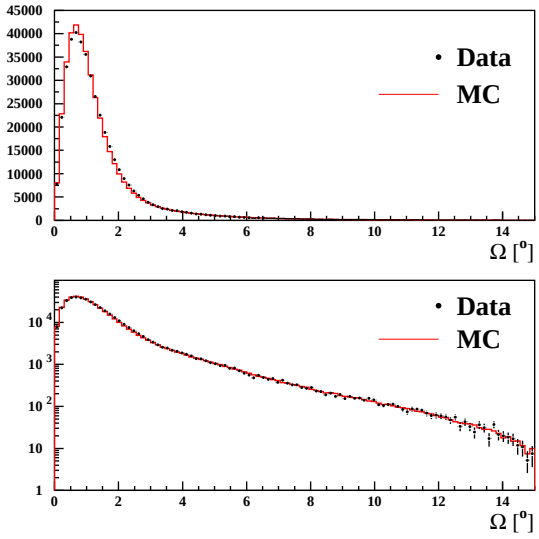

Figure 5.19: Ω-angle distribution for data (black points) and MonteCarlo (red line). The distribution is shown in linear (upper plot) and logarithmic scale (lower plot).

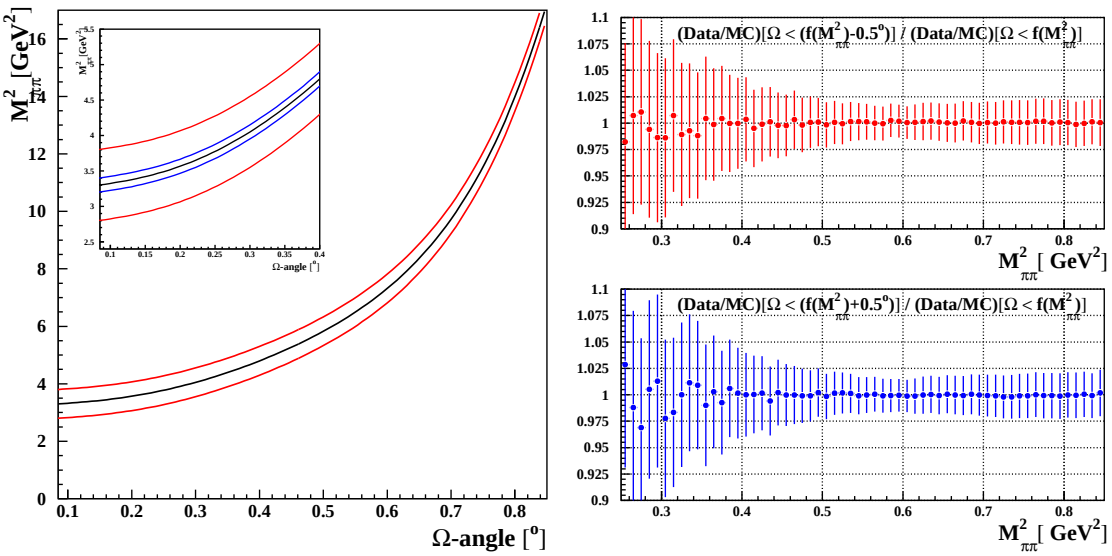

(a) (b)

Figure 5.20: (a) Systematic shift of the Ω to evaluate the systematic error of the Ω-angle cut. The black line represents the nominal cut, the two red the maximun variation of the Ω cut and blue lines two intermediate steps.(b) R_Ω for the maximum and the minimum variations of Ω.

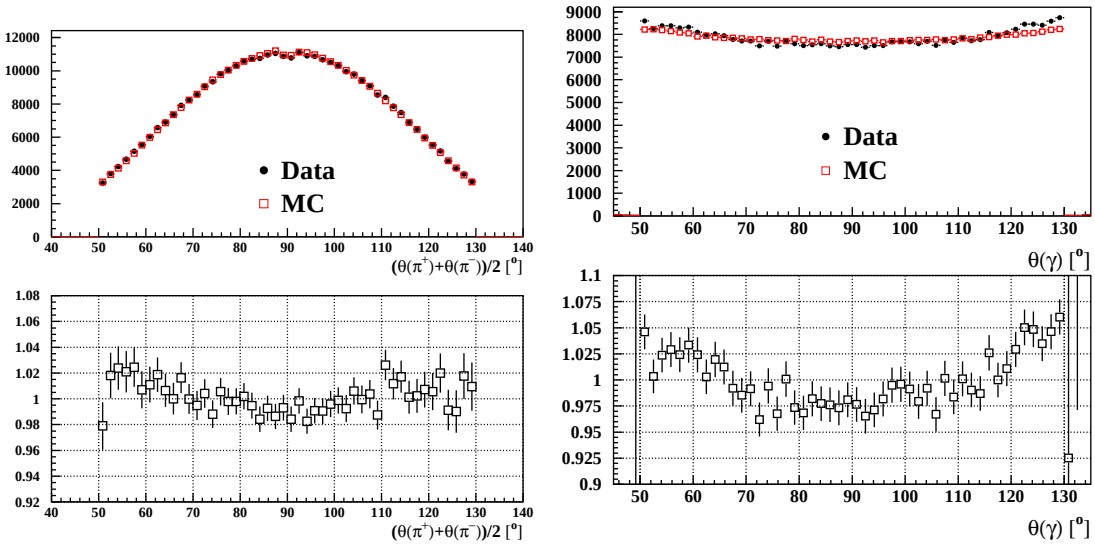

(a) (b)

Figure 5.21: Comparison between data (full points) and MonteCarlo (open squares) of the average of pions polar angle and its ratio (a) and of the photon polar angle and its ratio (b).

The interference between FSR (up to 20% in this angular region) and ISR events gives rise to an asymmetry in the distribution on the pion polar angle (see §3.4 for more details). This asymmetry vanishes if symmetric cuts on the pion polar angle are applied, as it is the case in this analysis.
As for the previous cuts, the study of the acceptance is performed in two steps:

1. comparison between data and MonteCarlo of the polar angle of the pions and of the photon;

2. evaluation of the systematic error introduced by the acceptance cuts.

The comparison mentioned in point 1 is shown in fig. 5.21, for the average of the polar angles of the two tracks and for the photon. In this plot the residual background has been subtracted from the data and the two samples, data and MonteCarlo, are normalized to the same number of events. In the case of the pions some small discrepancies are observed, but they become much bigger for the polar angle of the photon. The possible explanations that we have tested do not seem to be responsible for such a discrepancy. We describe them in the following list:

- as mentioned in §1.5 the $\pi^+\pi^-\gamma$ MonteCarlo simulation depends on the parametrization of the pion form factor. In fig. 5.22 the pion and the photon polar angle computed from two different MonteCarlo generations are compared; in one of the two the pion form factor was parametrized according to Kühn-Santamaria [61] (full black points), in the other according to Gounari-Sakurai [60] (open triangles).

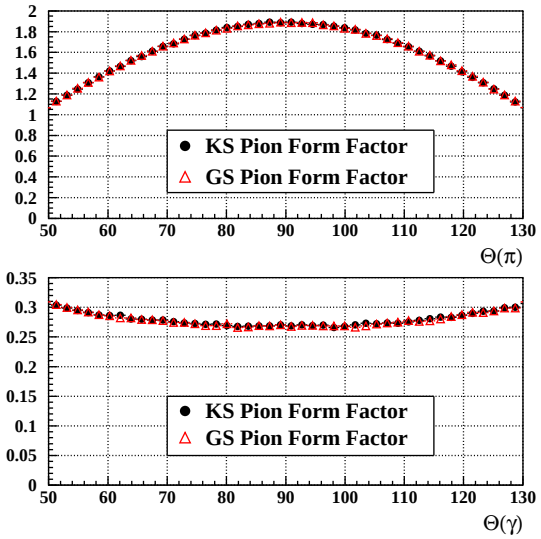

Figure 5.22: Comparison of the polar angle of the pions and of the photon for two different parametrization of the pion form factor.

The excellent agreement between the distributions excludes that the parametrization of the pion form factor can explain the differences observed in fig. 5.21;

- the background from $\mu^+\mu^-\gamma$ and $\pi^+\pi^-\pi^0$ events is well under control and from checks done in different regions of $M^2_{\pi\pi}$ and using several cuts on trackmass (to allow different percentage of background in the data sample), we exclude that the background contamination (at least the *reducible*) is the reason for the discrepancy data-MonteCarlo;

- we have observed that cutting tighter in the Ω-angle the discrepancies between data and MonteCarlo increases at high $M^2_{\pi\pi}$. Since the cut on the Ω-angle is the one that affect mostly the efficiency for NLO-events (see fig. 4.8), one possible explanation is the limited description of MonteCarlo of the NLO-events.

In the next step (point 2 of the list at the beginning of the paragraph) we try to quantify the effect of the observed discrepancies in the mass spectrum.
For this purpose we have evaluated the double ratio R_{θ_π} and R_{θ_γ}, defined as

$$R_{\theta_\pi,\theta_\gamma} = \frac{N(data)/N(MC)|\ shifted\ \theta_\pi,\theta_\gamma}{N(data)/N(MC)|\ nominal\ \theta_\pi,\theta_\gamma} \tag{5.4}$$

In order to understand how much to enlarge and restrict cuts in $\theta_{\pi^\pm}$ and θ_γ a study on the resolution of the two variables $\theta_{\pi^\pm}$ and θ_γ has been done. The two angles are treated separately.

1. Effect of the cut on θ_π on the $M^2_{\pi\pi}$ spectrum:
   the resolution of θ_π is shown in fig. 5.23(a). It has been fitted with three gaussians:

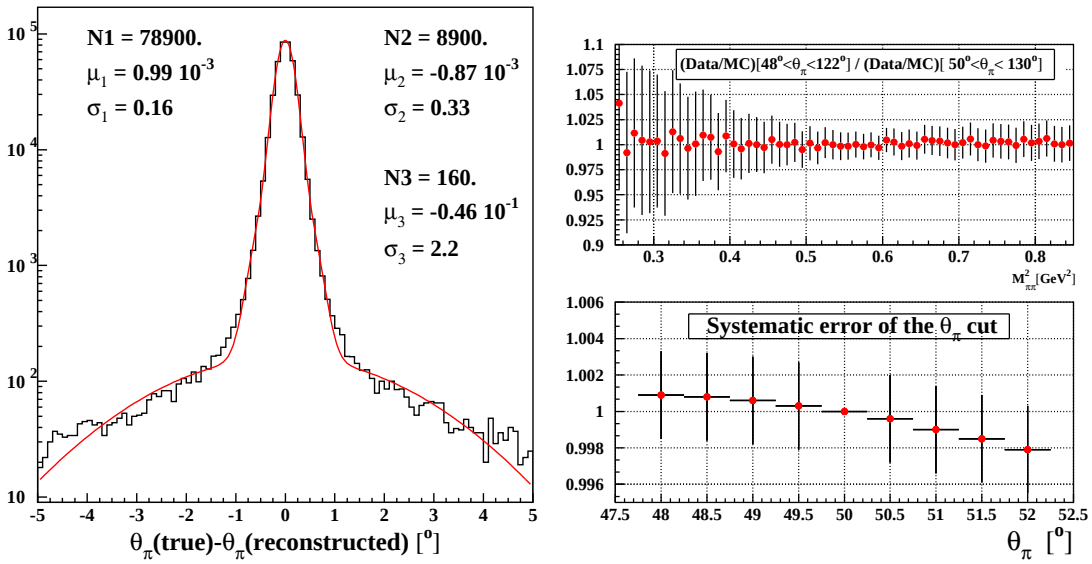

(a) (b)

Figure 5.23: (a) Resolution of the variable θ_π fitted with three gaussians. (b) Upper plot: double ratio R_{θ_π} evaluated with the request $48^o < \theta_\pi < 122^o$. All the other cuts are as in the *standard selection*. (b) Systematic error of the cut on θ_π.

since the third gaussian is necessary only for less than 1% of the events, we restrict ourselves to two gaussian only. The core gaussian (∼90% of the events) has a σ of 0.16 MeV, the second, necessary to describe the remaing 10% of the events has a σ of 0.33 MeV. We take for the resolution of the variable θ_π the sum of the two gaussians with σ =0.5 MeV. In order to quantify the effect of this cut on the mass spectrum we have looked at the double ratio R_{θ_π} where all the standard cuts of the analysis are applied ($\chi^2_{\pi\pi\pi}$, M_{trk}, Ω) and moving the cut on θ_π between 48^o and 52^o (corresponding to 132^o and 128^o on the other side) in steps of 0.5^o (for a total shift of 4 times the resolution). One example of double ratio R_{θ_π} is shown in the upper plot of fig. 5.23(b). For each steps of θ_π we have fitted R_{θ_π} with a straight line. The result of the fits is shown in the lower plot of fig. 5.23(b). The variation that we observe is 0.3%.

2. Effect of the cut on θ_γ on the $M^2_{\pi\pi}$ spectrum :
exactly the same approach as above has been followed. The resolution on θ_γ (fig. 5.24(a)) is well described if we fit it with three gaussians. Let us neglect the ∼5% of the events which need a third gaussian: under this assumption the resolution on θ_γ is given by the sum of the standard deviations of the remaining two gaussians, with $\sigma = 1.6^o$.
We have then evaluated the double ratio R_{θ_γ} enlarging and restricting the cut on θ_γ of 5^o, i.e. 3 times the resolution on this variables, in steps of 1^o (from 45^o to 55^o on one side and from 125^o and 135^o on the other). One example of the ratio R_{θ_γ} is given

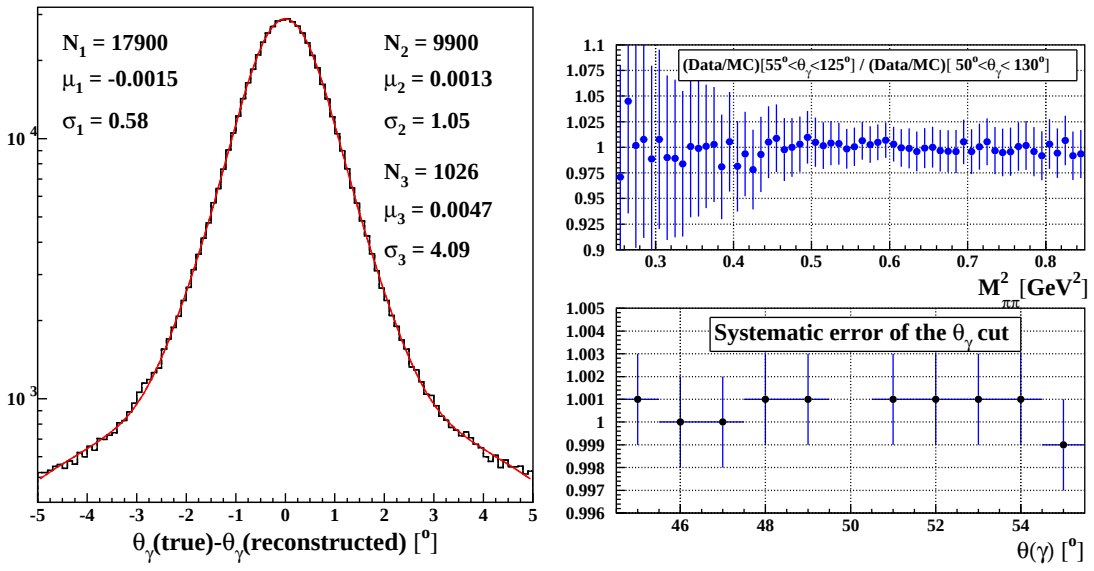

(a) (b)

Figure 5.24: (a) Resolution of the variable θ_γ fitted with three gaussians. (b) Upper plot: double ratio R_{θ_γ} evaluated requiring $55^o < \theta_\gamma < 125^o$ and leaving all the other cuts as in the *standard selection*. Lower plot: systematic error on the cut on θ_γ.

in the upper plot of fig. 5.24(b). As usual the double ratios R_{θ_γ} have been fitted with straight lines, as shown in the lower plot of fig. 5.24(b), where the results of the fit as a function of the θ_γ is plotted. From this plot we conclude that the systematic error introduced by the cut on θ_γ is 0.1%.

Given a 0.3% systematic error introduced by the cut on θ_γ and a 0.1% from the cut on θ_γ, we conclude that the total systematic error on the acceptance is 0.3%.

Chapter 6

Extraction of the pion form factor

In this chapter we will derive the pion form factor in the interval $0.5 \div 0.85$ GeV^2, related to the hadronic cross section via the formula:

$$\sigma(e^+e^- \to \pi^+\pi^-) = \frac{\pi\alpha^2}{3s}\beta_\pi^3 |F_\pi|^2 \tag{6.1}$$

where the cross section $\sigma(e^+e^- \to \pi^+\pi^-)$ for $0^o < \theta_{\pi,\gamma} < 180^o$ is obtained from the experimental $M^2_{\pi\pi}$ distribution shown in fig. 4.15 using the formula:

$$\frac{d\sigma_{\pi\pi}}{ds_\pi} = \frac{\Delta N_{obs} - N_{bkg}}{\Delta M^2_{\pi\pi}} \cdot \frac{1}{\epsilon_{tot}\Delta\epsilon} \cdot \frac{1}{\int \mathcal{L}\, dt} \cdot H(s_\pi) \tag{6.2}$$

ϵ_{tot} indicates the *effective global efficiency* and with $\Delta\epsilon$ the difference between the efficiency from MonteCarlo and data, both evaluated in §5.
The measurement of the integrated luminosity, which enters explicitly in eq. 6.2, is briefly presented.
Finally we will discuss the background subtraction due to *irreducible* backgroun from the scalar mesons; using the forward-backward and the charge asymmetry we will select the model among the available ones which fits best to data and we will subtract the background from scalar mesons. A preliminary estimate of the systematic error of the subtraction of the scalar mesons is presented.

6.1 Luminosity measurement

The integrated luminosity is measured with the KLOE detector looking at Bhabha events at large polar angles, $55^o < \theta < 125^o$ (Very Large Angle Bhabha,VLAB). At the DAΦNE energy the cross section for such events is $\sim$430 nb, big enough to make the statistical error negligible. The residual background, δ_{bkg}, is subtracted from the sample and the number of Bhabha candidates N_{BHA} is normalized to the effective Bhabha cross section evaluated

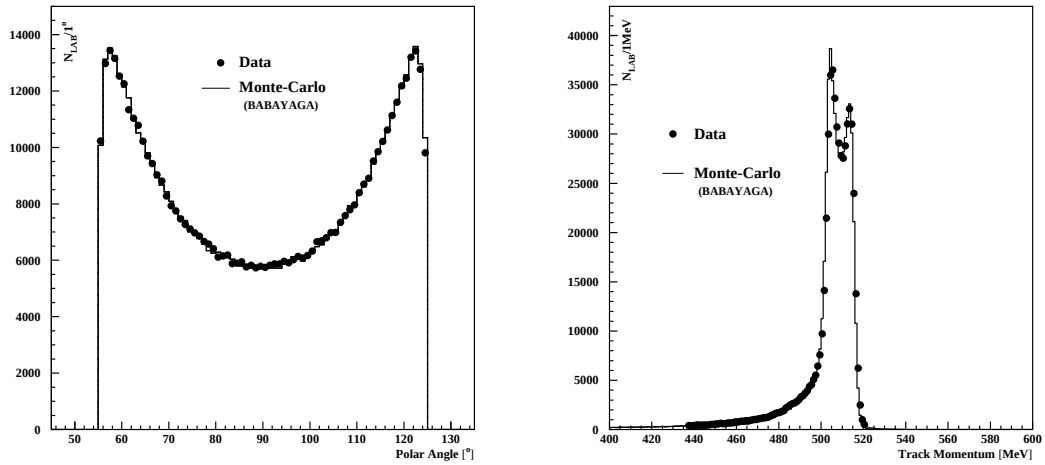

(a) (b)

Figure 6.1: Comparison between data and Monte-Carlo simulation for θ_{e^+,e^-} (a) and track momentum (b) for Bhabha events.

from Monte-Carlo, according to:

$$\int \mathcal{L}\, dt = \frac{N_{BHA}}{\sigma^{MC}_{BHA}}(1 - \delta_{bkg}) \tag{6.3}$$

The cross section is obtained from the Monte-Carlo generator BABAYAGA [83], which simulates QED processes with the parton-shower approach. The result has been compared with the one obtained from BHAGENF ([84], [85]), a generator to full order α. The authors of both generators declare a precision of 0.5% and comparisons between the two show an agreement at the 0.2% level.

An excellent agreement between data and Monte-Carlo is shown for the θ_{e^+,e^-} and $|\vec{p}_{e^+,e^-}|$ distributions in fig. 6.1(a) and 6.1(b). The background from $\mu^+\mu^-$ and $\pi^+\pi^-$ is well below 1% and has been subtracted. The polar angle values are based on calorimeter clusters fired by charged particles with an energy above 400 MeV. The efficiencies for trigger, drift chamber and clustering have been evaluated from Monte-Carlo to be >99% confirmed by data. A run-by-run correction has been applied to account for the fluctuations of the center-of-mass energy of the machine and for the EmC calibration. The total experimental error has been evaluated to be 0.3%; taking into account the theoretical error from the Monte-Carlo generator equal to 0.5%, the total systematic error assigned to the luminosity measurement is $\delta\mathcal{L} = 0.5\%_{th} \oplus 0.3\%_{exp} = 0.6\%$.

A different measurement has been performed using $e^+e^- \to \gamma\gamma$ events; an agreement within 0.2% was found. More details on the luminosity measurement can been found in [86].

6.2 The contribution of the *irreducible* background

The background channels with the same final state as the signal have been introduced already in §3.3. We remind that the three processes which we call *irreducible* background are:

- Leading-Order Final State Radiation (FSR-LO) where a photon is emitted by one of the pions;
- the resonant ϕ decay: $\phi \to \rho\pi \to \pi^+\pi^-\gamma$;
- the radiative ϕ decay to $\pi^+\pi^-\gamma$ through a scalar meson: $\phi \to (f_0(980) + f_0(600))\gamma \to \pi^+\pi^-\gamma$.

Of the three channels the FSR-LO contribution has been already taken into account by means of the unshifting from $M^2_{\pi\pi}$ to $M^2_{\gamma^*}$ in the *effective global efficiency* (§5). In the next two sections we will explore the remaining two.

6.2.1 The decay $\phi \to \rho\pi \to \pi^+\pi^-\gamma$

In order to check whether events from background channels different from $e^+e^-\gamma$, $\mu^+\mu^-\gamma$ and $\pi^+\pi^-\pi^0$ events end up in the final data sample, we have used a MonteCarlo production which simulates all the resonant physical processes occurring at our energy. We have run the full selection procedure on this sample and looked at the MonteCarlo information of the events that survive. As expected some events from the decay $\phi \to \rho\pi^\pm \to \pi^+\pi^-\gamma$ pass the selection. The spectrum of this events is shown in fig. 6.2(a), superimposed on the data spectrum, while in 6.2(b) its contamination in the data sample is presented. The $\rho\pi$ contribution reaches the level of 10% at 0.3 GeV^2, but it is negligible above 0.5 GeV^2. Even if simulated by MonteCarlo, the subtraction of this background is quite a delicate point. The simulation assumes a certain model and the interference with the FSR events is not considered. Very recently a new version of the MonteCarlo code EVA has been released [79], including the $\rho\pi$ channel and its interference with FSR. This code will be used in the next future to further study the $\rho\pi$ background §7.1).

6.2.2 The scalar mesons and the asymmetries

In orded to quantify the effects of the scalar mesons in the data sample we have used the last version of the PHOKHARA event generator (version 5.1). In this version three different models for radiative ϕ-decays into scalar mesons are implemented:

- the kaon-loop inclusive of the $f_0(980)$ described in §3.3.1 used for fitting the KLOE data [77]. We will call this model as KL-$f_0(980)$;
- a kaon-loop-like model taking into account both the $f_0(980)$ and $f_0(600)$ [87], which will be called KL-$f_0(980) + f_0(600)$ in the following;

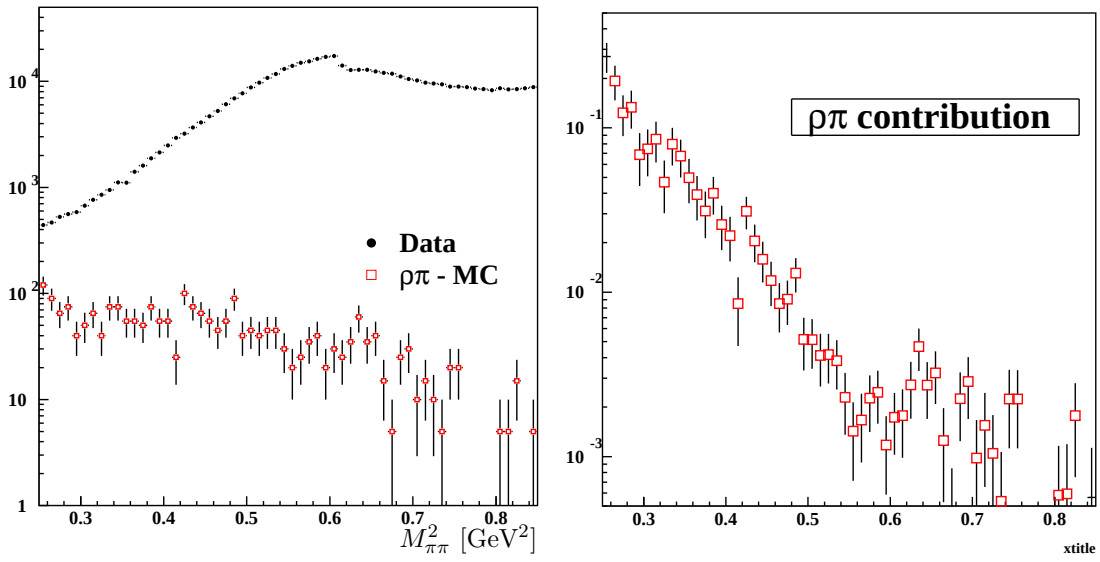

(a) (b)

Figure 6.2: (a) $\rho\pi$ spectrum from MonteCarlo (open red squared) superimposed to the data spectrum (black points) after the full selection. (b) Contamination of the $\rho\pi$ process in the data sample.

- the so-called 'no structure' model, which accounts both for $f_0(980)$ and $f_0(600)$ [88]. We will refer to this last model as 'NS'.

The description of two models KL-$f_0(980)+f_0(600)$ and NS can be found in [64] and in the references there. In [64] a fit to $\pi^0\pi^0$ invariant mass obtained from the analysis $\phi \to \pi^0\pi^0\gamma$ at KLOE [76] and SND [89] is performed using both these two models and the results of the fits are reported. Our tests on the KL-$f_0(980)+f_0(600)$ and NS models are performed with the parameters found there.
The study of the scalar mesons is divided into two parts:

1. choice of the model among the three mentioned above;

2. tuning of the parameters of the model (couplings of the $f_0(980)$) within this model.

Before starting the procedure just described, we show in fig. 6.3 the scalar mesons contribution at large polar angle as estimated from the models introduced above. The four predictions give results completely different one from the other. The blue and the green curve refer to the same model. What changes is the phase α between the amplitude of the process $\phi \to f_0(980)+f_0(600) \to \pi^+\pi^-\gamma$ and the one of the non-resonant FSR events. The effect of such a phase becomes even more evident in the forward-backward asymmetry.

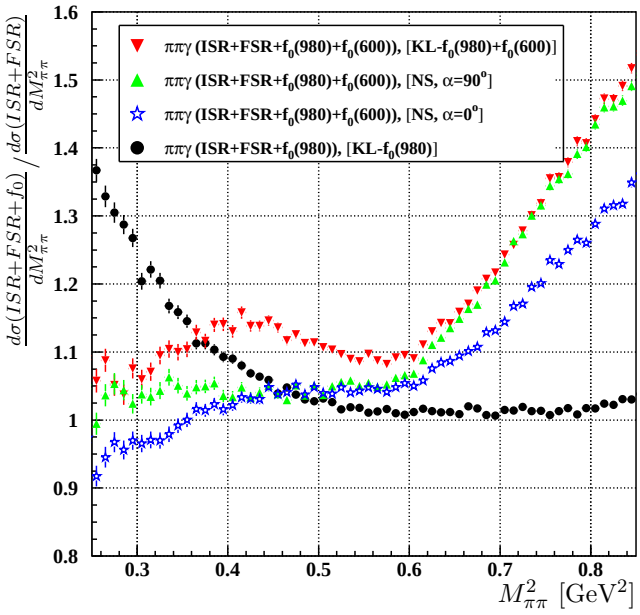

Figure 6.3: Scalar mesons contribution according to different models. In the text α if the phase related to the interference between the amplitude of the resonant process and the amplitude of the FSR events.

6.2.2.1 Choice of the model for the scalar mesons

In this paragraph we will select the model for the scalar mesons which later we will use as part of the correction for the pion form factor. Two variables, the forward-backward asymmetry and the charge asymmetry, are very powerful in enhancing the differences among the various models. By comparing the data with the different models in the two asymmetries, some models are automatically excluded.

In this part of the study, for the KL-$f_0(980)$ we will use the parameters obtained in [77].

Looking at the forward-backward asymmetry (fig. 6.4), already two over the four cases considered are excluded. The data (full black points) present a clear bump around the $f_(980)$ mass and below the ρ-peak there is a rise. The discrepancy with pure (ISR+FSR) MonteCarlo prediction (green asterisks) is huge either at low and high masses. In the low mass region the different models for the scalar mesons tested here also present different behaviors: two of them (empty magenta and full pink squares) tend to follow the same shape of (ISR+FSR) prediction, being then very far from the data. The same two present at high masses a bump in a different position with respect to data. We remain then with only two models to be tested, i.e. the ones corresponding to the red and the blue triangles of fig. 6.4. For choosing between these two we introduce the charge asymmetry defined as:

$$\mathcal{A}_{charge}(\theta_\pi) = \frac{N(\pi^+) - N(\pi^-)}{N(\pi^+) + N(\pi^-)}(\theta_\pi). \tag{6.4}$$

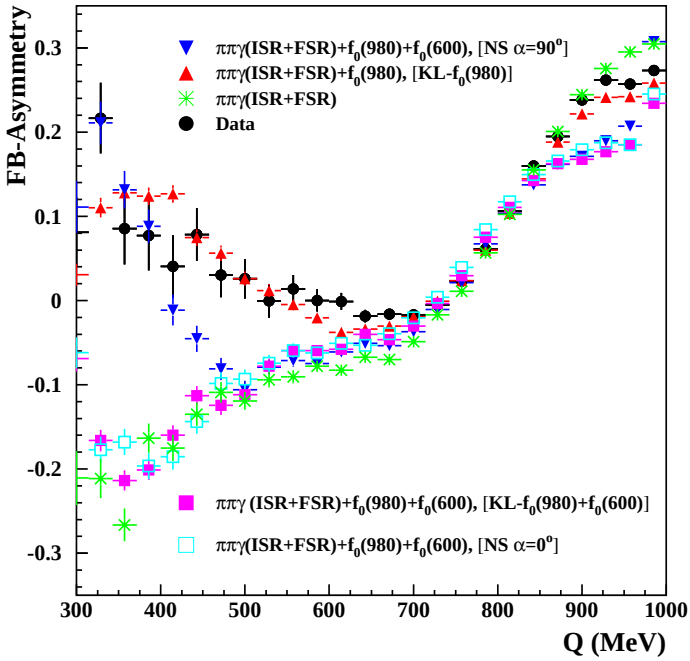

Figure 6.4: Forward-backward asymmetry evaluated from data (full black points) and compared to several MonteCarlo predictions.

The charge asymmetry is not independent from the forward-backward asymmetry, but it can be used in a complementary way. We have looked at it in bins of $M^2_{\pi\pi}$, comparing the data and the two remaining models of scalar mesons. In fig. 6.5 such a comparison is shown in two $M^2_{\pi\pi}$ bins, at high and at low masses. The KL-$f_0(980)$ (the red triangles) is clearly favoured with respect to the NS model (blue triangles). To be more quantitative a χ^2 has been evaluated according to the formula:

$$\chi^2 = \frac{Asy^{Data} - Asy^{MC}}{\sqrt{\sigma^2(Data) + \sigma^2(MC)}} \tag{6.5}$$

The values of the χ^2 for the two models for all the $M^2_{\pi\pi}$ bins are shown in fig. 6.5. Except in one single bin, the χ^2 for the KL-$f_0(980)$ model is always smaller than for NS model. We exclude therefore the NS model and in the following the KL-$f_0(980)$ model will be our reference model for the scalar mesons.

6.2.2.2 Tuning of the parameters

In the KL-$f_0(980)$ model, three parameters enter for the $f_0(980)$ (we remind that it does not include the $f_0(600)$): the $f_0(980)$ mass and the two couplings g_{f_0KK} and $g_{f_0\pi\pi}$. The strategy is to change systematically the two couplings and to compare for each set the forward-backward asymmetry between data and MonteCarlo.
Since at low $M^2_{\pi\pi}$ the statistics of data is limited, we have firstly averaged the forward-backward asymmetry measured with the π^+ and the π^-. In order to enhance as much as

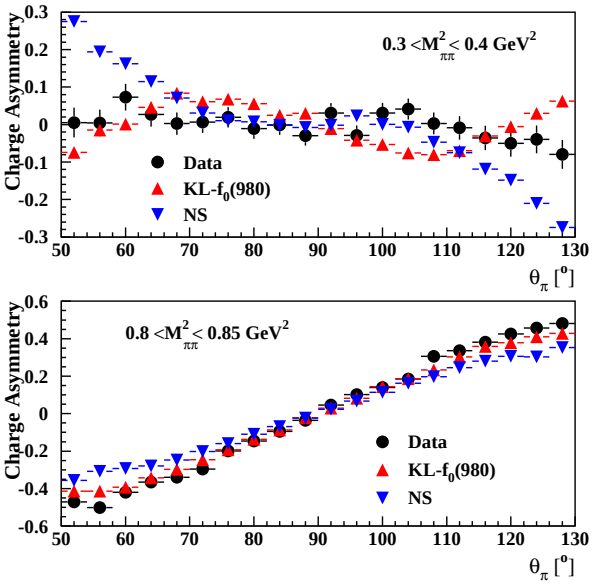

$M^2_{\pi\pi}$ bin [GeV^2]	χ^2 KL-$f_0(980)$	χ^2 NS
0.3÷0.4	86	155
0.4÷0.5	62	172
0.5÷0.6	26	42
0.6÷0.7	70	28
0.7÷0.8	90	207
0.8÷0.85	74	444

Figure 6.5: Right: charge asymmetry for data and MonteCarlo including two different models for the scalar mesons in two different bins of $M^2_{\pi\pi}$. Left: χ^2 data-KL-$f_0(980)$ and data-NS.

possible the effect of the $f_0(980)$ we have enlarged the mass spectrum up to 1 GeV^2 (in the analysis it arrives up to 0.85 GeV^2). The averaged forward-backward asymmetry from data is then compared with the averaged one from MonteCarlo. In order to make the comparison quantitative we have built the quantity:

$$\chi^2 = \sum_{bin} \frac{A^{Data} - A^{MC}}{\sqrt{\sigma^2(A^{Data}) + \sigma^2(A^{MC})}} \tag{6.6}$$

where A is the value of the forward-backward asymmetry for each bin and $\sigma(A)$ is its error. The value of the χ^2 is evaluated in the full range $M^2_{\pi\pi}$ ($4m^2_\pi \div 1$ GeV^2). In fig. 6.6(a) some examples of the charge asymmetry of good χ^2 values are shown. The behavior at high $M^2_{\pi\pi}$ is nicely reproduced by MonteCarlo, while even with the couplings that give the best χ^2 some discrepancies are visible a low masses. The values of χ^2 are around 100 for these cases (the number of degree of freedom is 34). Some examples of bad χ^2 are shown in fig. 6.6(b): the value of χ^2 is big for these cases either because of a relatively small discrepancy at high $M^2_{\pi\pi}$ (g_{f_0KK}=4.14 and $g_{f_0\pi\pi}$=3.85 in the plot) or of a strong disagreement between 0.2 and 0.5 GeV^2 (g_{f_0KK}=4.39 and $g_{f_0\pi\pi}$=3.85 in the plot). The value of χ^2 has been evaluated over a wide range of couplings, to find a plateau of minima. In tab. 6.1 the values of χ^2 are shown for the tested couplings. The plateau is reached for values of χ^2 around 100 and values of couplings $g(f_0KK) = 4.39$ and $g(f_0\pi\pi) = 3.6$. With this procedure we have tuned the parameters of the model describing the $f_0(980)$ directly on our data. One set of couplings which falls in the plateau of minima are fixed in order to have a reference MonteCarlo for the description of the $f_0(980)$. We have taken as reference $g(f_0KK) = 4.39$ and $g(f_0\pi\pi) = 3.6$.

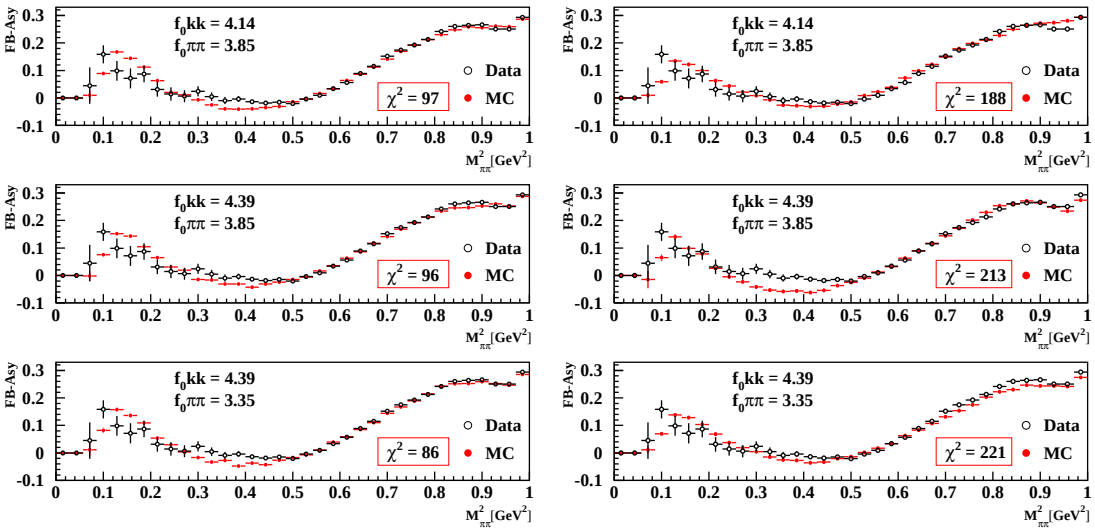

(a) (b)

Figure 6.6: Comparison of the forward-backward asymmetry between data and MonteCarlo with different couples of couplings for the $f_0(980)$. Some examples of good agreement are shown in (a) while in (b) couples of couplings which give bad results of χ^2 can be seen.

Some tests have been performed to check the procedure:

- in the KL-$f_0(980)$ model the pion form factor parametrization enters. We have checked varying the parameters within the Kühn-Santamaria parametrization that it does not affect the χ^2 minimization procedure;
- in §6.2.1 we have seen that the low $M^2_{\pi\pi}$ region is contaminated by the presence of the direct decay $\phi \to \rho\pi \to \pi^+\pi^-\gamma$ up to some percent. If this process has an effect on the forward-backward asymmetry, the plateau of minima could be biased by the presence of this background. Since the spectrum of $\phi \to \rho\pi \to \pi^+\pi^-\gamma$ becomes negligible above ∼0.5 GeV^2, we have repeated the full χ^2 minimization procedure at high masses ($M^2_{\pi\pi}$ >0.75 GeV^2). We find the plateau of minima in the same position.

Very recently a new version of the EVA MonteCarlo has been released [79]. This generator includes the scalar mesons contribution according to a more sophisticated kaon loop model, with respect the one inserted in PHOKHARA, and the Vector Meson Dominance for the $\phi \to \rho\pi \to \pi^+\pi^-\gamma$. The interference effects are simulated also. The parameters for the $f_0(980)$ and the $f_0(600)$ are those coming from the analysis $e + e^- \to \pi^0\pi^0\gamma$ performed by KLOE [90]. More details concerning the new version of EVA can be found in §7.1.
A very preliminary comparison between the scalar mesons contribution predicted by EVA and by PHOKHARA is shown in fig. 6.7. The difference at the moment is huge below 0.5 GeV^2 but we are confident that the two predictions can become closer when the procedure of tuning of the parameters of the scalar mesons will also be applied to EVA. Our strategy

$g(f_0KK) \rightarrow$	2.89	3.39	3.89	4.14	4.39	4.64	4.89	5.39	5.89	6.39	6.89
$g(f_0\pi\pi) \downarrow$											
2.6			175		214		234		297	324	383
3.1		150	129	120	134	131	149	190	219	213	277
3.35				102	86	108					
3.6	156		89	105	98	107	138	171	184	230	
3.85				98	95	134					
4.1		134	104	114	126	112	140	171	221		
4.6	183				129		150			271	
5.1					129		150			271	
5.6	231	188									

Table 6.1: Value of χ^2 for each couples of couplings tested.

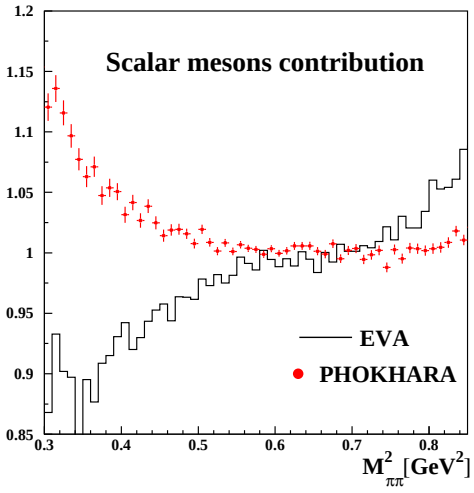

Figure 6.7: Contribution of $f_0(980)$ at large angle predicted by PHOKHARA (full red points) compared with the contribution of $f_0(980) + f_0(600) + \rho\pi$ predicted by EVA (black line).

is to use both the generator, PHOKHARA and EVA, to give an estimate of the systematic error of the subtraction of the scalar mesons.
For the time being we take as the systematic error for the scalar mesons subtraction the difference between the prediction of the two generators, i.e. the difference between the two curves of fig. 6.7.

6.3 The pion form factor

The quantities which enter in eq. 6.1 to evaluate the pion form factor have all already been presented in §4 and §5. What remains is the correction for the vacuum polarization effects in the photon propagator.
The cross section which appears in the dispersion integral (eq. 6.1) is the *bare* cross section [1]; therefore we have to apply a correction according to

$$\sigma_{\rm bare}(s) = \sigma_{\rm dressed}(s) \left(\frac{\alpha(0)}{\alpha(s)}\right)^2 = \sigma_{\rm dressed}(s)/\delta(s) \tag{6.7}$$

The hadronic contribution $\Delta\alpha^{hadr}(s)$ of eq. 1.29 has been evaluated using existing measurements of $\sigma(e^+e^- \to hadrons)$ (which do not yet contain the KLOE measurement). The correction factor $\delta(s)$ ([91]) is shown in fig. 6.8(a).
In fig. 6.8(b) the radiator function $H(M^2_{\pi\pi})$ (eq. 6.2) is presented. It is evaluated by PHOKHARA for the full phase space ($0^o < \theta_{\gamma,\pi} < 180^o$), being applied to the spectrum after the acceptance correction.
Before presenting the pion form factor we summarize in tab. 6.2 the systematic errors for the various efficiency corrections that enter in the final result. The evaluation of each of them has been discussed in §5. The table anticipates also the estimate of the systematic error on the FSR events, which will be presented in §6.4 and it does not contain the one of the scalar mesons. Some systematic errors are not flat in $M^2_{\pi\pi}$; we have chosen three reference points to give the total systematic error, one on the ρ-peak and the other two at low and high $M^2_{\pi\pi}$ respectively.
In fig. 6.9 the pion form factor, as evaluated within this work using large angle photon events, between 0.5 and 0.85 GeV^2 is shown. The red band represents the systematic error of the scalar mesons correction. The published KLOE result obtained with the 2001 sample is superimposed (blue points). The small errors bars for the 2001 points are due to the fact that only the statistical error is considered. In fig. 6.10 the ratio between the two pion form factors is shown. The error bars represents only the statical errors; for the 2002 sample also the statistical error on the *global effective efficieny* has been considere, not being negligible.

[1] The *dressed* cross section $\sigma_{had}(s)$, as all the measured quantities, is proportional to the square of the effective running fine structure constant $\alpha(s)$. The *bare* one is indeed proportional to the square of the classical fine structure constant α determined at zero momentum transfer.

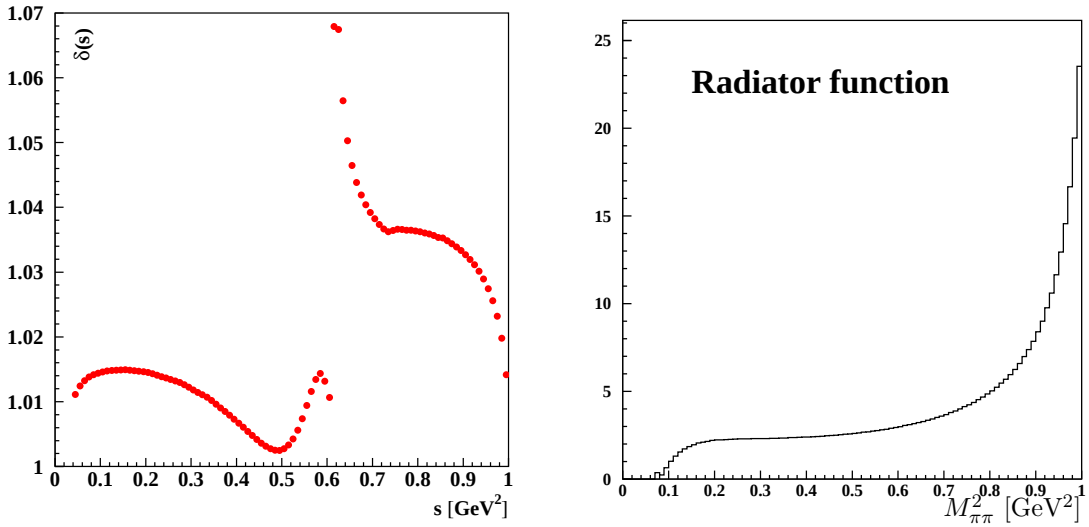

(a) (b)

Figure 6.8: (a) Correction factor taking into account vacuum polarization effects in the photon propagator: $\sigma_{\rm bare}(s) = \sigma_{\rm dressed}(s)/\delta(s)$. (b) Radiator function (from PHOKHARA)

	Flat in $M^2_{\pi\pi}$	0.4 GeV^2	0.6 GeV^2	0.85 GeV^2
Tracking	0.2%			
Vertex	0.2%			
Particle ID	0.3%			
Acceptance	0.3%			
$\mu^+\mu^-\gamma$ and $\pi^+\pi^-\pi^0$ subtraction		0.2%	<0.1%	0.3%
Kinematic fit	0.2%			
Trackmass cut	0.2%			
Ω-Angle cut	0.1%			
FSR correction		0.4%	0.2%	∼1%
Trigger	0.1%			
Filfo	0.1%			
Total		0.8%	0.6%	1.2%

Table 6.2: List of the systematic errors for the cuts of the selection of the *large angle* analysis. The systematic error of the subtraction of the scalar mesons background is not reported.

The systematic error on the scalar meson model in shown in the zoom. Considering the systematic errors of the published result we conclude that in this energy range the two measurements are compatible.
In order to check the procedure for the extraction of the pion form factor we have worked out two ways to obtain it. In one case, that we call *inclusive* approach, the FSR is kept in the sample and the correction for those events is in the *effective global efficiency* introduced at the beginning of §5. The standalone version of PHOKHARA is used for the estimate of the scalar mesons contribution. The starting point in both the approaches is the data spectrum $dN/dM^2_{\pi\pi}$ after the *reducible* background subtraction. The *inclusive* procedure to extract the pion form factor is described step by step in the following list:

- the data spectrum at this level contains still the scalar mesons and the FSR contributions. We correct it for the *effective global efficiency*:

$$\epsilon(i) = \frac{dN^{rec}(i)/dM^2_{\pi\pi}[50^o < \theta_{\gamma,\pi^\pm} < 130^o, \text{end of analysis}]}{dN^{true}(i)/ds_{\gamma^*}[0^o < \theta_{\gamma,\pi^\pm} < 180^o]} \tag{6.8}$$

  which accounts for the FSR-NLO efficiency;

- correction for the difference data-MonteCarlo $\epsilon(data)/\epsilon(MonteCarlo)$ for those cuts which need (tracking and vertex efficiencies)

- normalization to the integrated luminosity, division by the radiator function H and correction for the vacuum polarization

- correction for the $f_0(980)$ contribution by PHOKHARA (standalone version) according to the red points of fig. 6.7

- subtraction of the FSR contribution according to [92].

In the *exclusive* approach the correction for FSR and the scalar mesons is applied at the beginning. This approach is possible since the version of PHOKHARA including the scalar mesons has been implemented in the KLOE detector simulation. Therefore it is possible to simulate all the analysis cuts on a MonteCarlo sample including FSR and scalar mesons. Starting again from the data spectrum $dN/dM^2_{\pi\pi}$ after the *reducible* background subtraction, the steps for the *exclusive* approach are:

- correction for FSR and the scalar mesons by means of

$$\epsilon_{FSR+f_0(980)} = \frac{d\sigma^{MC}_{ISR+FSR+f_0}/dM^2_{\pi\pi}}{d\sigma^{MC}_{ISR}/dM^2_{\pi\pi}} \tag{6.9}$$

  This correction is applied at the end of all the analysis cuts. After the correction we remain with a sample made of ISR events only. Corrections for the efficiencies of the analysis cuts are not applied yet;

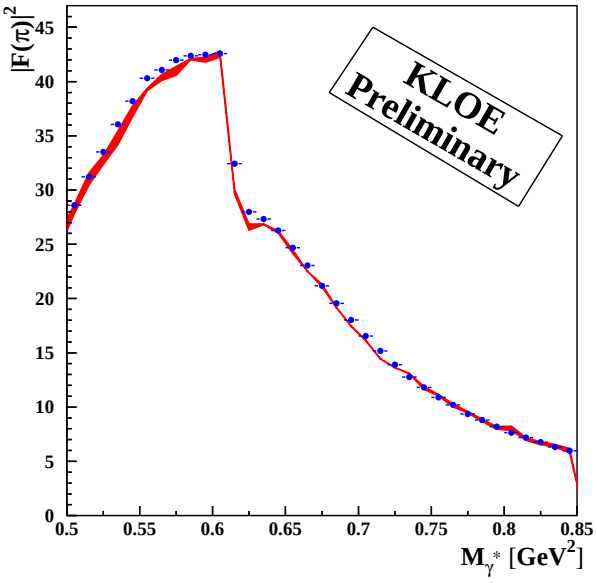

Figure 6.9: Pion form factor from 0.5 to 0.85 GeV^2 obtained at large angle (red band) compared with the one obtained al small angle with 2001 data. The red band represents the systematic error introduced by the subtraction of the scalar mesons.

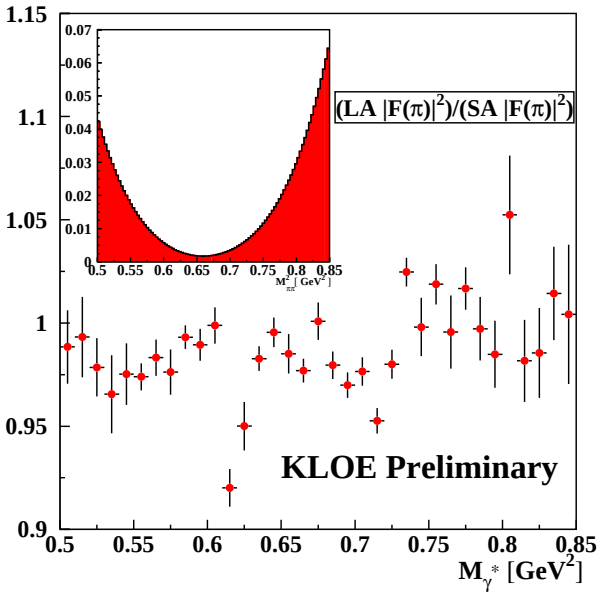

Figure 6.10: Ratio between the two measurements of the pion form factor shown in fig. 6.9. The error bars represent only the statistical error. In the 2002 sample the statistical error from the *effective global efficiency* has been also considered. In the zoom the systematic error from the model describing the scalar meson contribution is shown.

- correction for a *effective global efficiency* evaluated on a pure ISR MonteCarlo sample

$$\epsilon_{global}^{ISR} = \frac{dN_{ISR}^{MC}/dM_{\pi\pi}^2|_{after\ all\ cuts}}{N_{ISR}^{MC}/dM_{\pi\pi}^2|_{without\ all\ cuts}} \tag{6.10}$$

This correction takes into accounts the efficiencies for the analysis cuts and the reconstruction effects.

- correction for the difference data-MonteCarlo $\epsilon(data)/\epsilon(MonteCarlo)$ for those cuts which need (tracking and vertex efficiencies)
- normalization to the integrated luminosity, division by the radiator function H and correction for the vacuum polarization

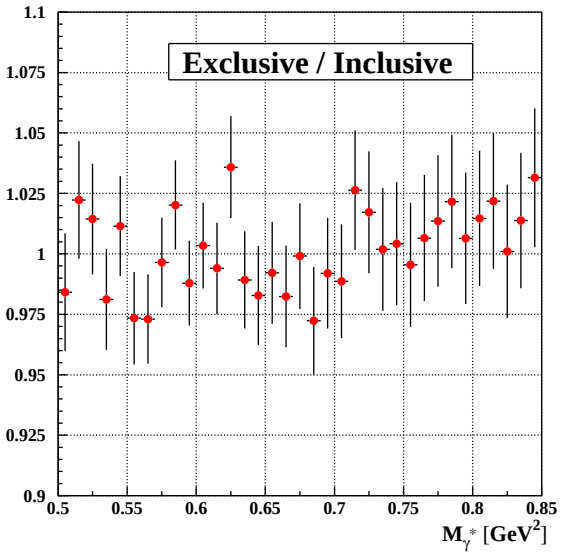

Figure 6.11: Ratio between the pion form factor obtained with the *exclusive* approach and the one obtained with the *inclusive* approach.

The pion form factor obtained with the two procedures has been finally compared: from fig. 6.11 we see that the ratio is compatible with 1. Only above 0.75 GeV^2 a small trend can be recognised. This is the region where the scalar mesons contribution is increasing; therefore the small difference is probably due to the different treatments of this background. In the *inclusive* approach this contribution is estimated from the standalone version, therefore the experimental efficiencies (which can have an effect on NLO events) are not considered. In the other case also the reconstruction effects are simulated and all the chain of cuts is applied also. Given this difference in the two treatments, we can conclude that the two approaches give the same result.
Finally the cross section $e^+e^- \rightarrow \pi^+\pi^-$ as a function of the invariant mass of the intermediate photon is presented in fig. 6.12. The error band corresponds to the systematic error of subtraction of the scalar mesons as in the plot for the pion form factor. Differently from the pion form factor, the cross section is inclusive with respect to the final state radiation and is not corrected for the vacuum polarization (*dressed* cross section).

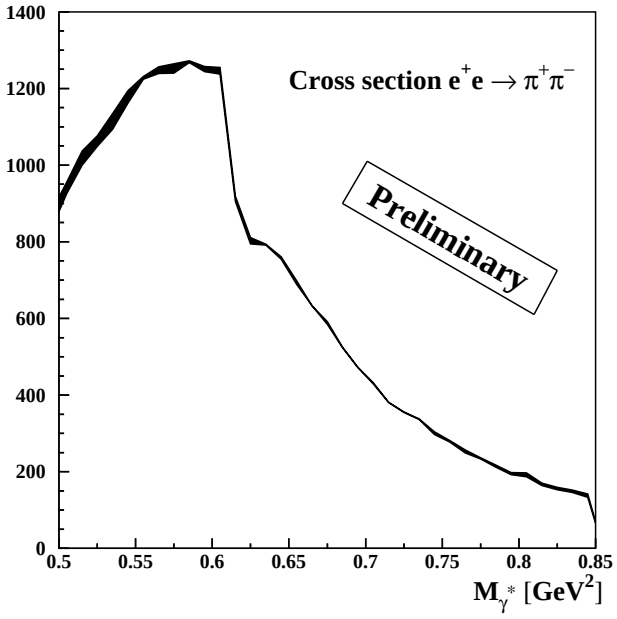

Figure 6.12: Cross section $e^+e^- \to \pi^+\pi^-$.

6.4 Systematic error of the FSR events

At the beginning of 2006 KLOE has collected a data sample at the center-of-mass energy of 1 GeV. Since it has been collected off-resonance, in this sample the contribution of scalar mesons is strongly suppressed (see §7.2 for more details). In §6.2.2 the forward-backward asymmetry has been introduced as a powerful instrument to study the models describing the scalar mesons. It allows explcitely to test the sQED model for the description of FSR, as shown in §3.4.

We remind that the forward-backward asymmetry arises from the interference of FSR and ISR events. Testing the forward-backward asymmetry corresponds then to test directly the description of FSR, which is simulated according to sQED in PHOKHARA. In fig. 6.13(a) the forward-backward asymmetry obtained from the 2002 and the 2006 samples is shown. The big effect of the scalar meson visible in the 2002 data both at high and at low masses disappears in the 2006 sample.

The forward-backward asymmetry obtained with the 2006 sample is compared fig. 6.13(b) with a pure ISR+FSR MonteCarlo: an overall agreement is found. An average difference of 5% is found when we fit the ratio between the curves with a straight line. In fig. 3.11 the amount of FSR (LO and NLO) at large photon polar angles is shown. The flat difference of 5% multiplied by the total contribution of FSR events gives us the systematic uncertainty of the correction for this process. The error is not flat in $M^2_{\pi\pi}$; on the ρ-peak it is 0.2%, as shown in tab. 6.2.

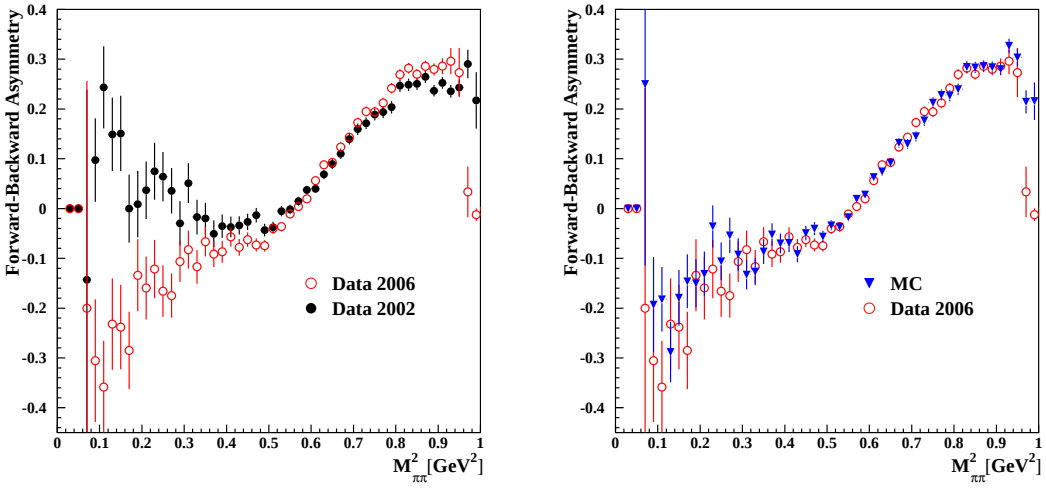

(a) (b)

Figure 6.13: (a) Forward-backward asymmetry for 2002 data (full black points) and 2006 data (open red circles). (b) Forward-backward asymmetry for 2006 data (open red circles) and MonteCarlo (blue triangles).

Chapter 7

Conclusion and possible improvements of the measurement

The *radiative return method* has been used to analyse in the *large angle* region $\sim$240 pb^{-1} collected by KLOE in 2002. The background from radiative Bhabha events, muon pairs and $\pi^+\pi^-\pi^0$ events is subtracted according to the MonteCarlo prediction. The systematic error associated to the background subtraction is in the energy squared range 0.5$\div$0.85 GeV^2 below 0.3%. The efficiencies of the analysis selection have been evaluated from data control sample in some cases, from MonteCarlo otherwise. For each analysis cut the associated systematic error has been estimated, for a total sistematic error on the ρ-peak of 0.6% if we neglect the contribution from the *irredubile* background. In order to take into account the scalar meson contribution, several models describing the decay $\phi \to (f_0(980) + f_0(600))\gamma \to \pi^+\pi^-\gamma$ have been tested and the one that best fits the data has been chosen. By means of comparison between data and MonteCarlo of the forward-backward asymmetry the parameters which enter the model for the $f_0(980)$ have been tuned. Finally the pion form factor, which has been extracted in the energy squared range 0.5$\div$0.85 GeV^2, has been corrected for the scalar meson contribution. The pion form factor has been compared with the published one (*small angle* analysis) and the two, considered the systematic error of both the measurements, are found to be compatible. Some improvements of the measurement are foreseen, mostly to reduce the systematic error associated to the subraction of the scalar meson contribution, as will be discussed.
Moreover in 2006 KLOE has collected a data sample off-peak at $\sqrt{s}$=1000 MeV, 20 MeV below the ϕ mass. We discuss the potential of this sample on the hadronic cross section measurement.
Finally, the update of the *small angle* analysis with 2002 data is forthcoming, and the motivation for it is given briefly.

7.1 Improvement of the *large angle* analysis

During the development of the analysis at large photon polar angles, the issue of *irreducible* background from scalar mesons has become more and more evident. But in the meantime also the potential of this sample has been understood to study the nature of these scalars in our data set.
The already published KLOE analysis of the decay $\phi \to f_0(980)\gamma \to \pi^+\pi^-\gamma$ [77] has been done in the following way:

1. performing a fit of the mass spectrum with (ISR+FSR+$f_0(980)$+direct decay $\phi \to \rho\pi$), obtaining the mass and the coupling of the $f_0(980)$ from the fit;
2. checking the parameters of the fit looking at the forward-backward asymmetry.

At present more is known on the scalar mesons and a new contribution by KLOE on their dynamics and their parameters is possible. Our plan is to continue the work started in §6.2.2 whose strategy is the opposite with respect to the one of [77] and described above, i.e.:

1. fixing the scalar mesons parameters by comparing the forward-backward asymmetry obtained from data and MonteCarlo
2. using the parameters obtained in step 1, looking at the mass spectrum.

This work has already been done with PHOKHARA and some conclusions about the several models describing the scalar mesons and implemented there have already been drawn in §6.2.2. The next step will be to apply the same procedure to the EVA generator. EVA includes several contributions:

- Initial + Final State Radiation;
- scalar meson contribution $f_0(980)$ and $f_0(600)$ described according to a more sophisticated version of the kaon loop model with respect to the one inserted in PHOKHARA and used to fit the KLOE data $\phi \to f_0(980)\gamma \to \pi^+\pi^-\gamma$ (see ref.[79] and references there);
- $\phi \to \rho^\pm\pi^\mp \to \pi^+\pi^-\gamma$ according to the Vector Meson Dominance;
- extension of sQED for FSR events (Resonance Perturbation Theory).

The last point of this list can become of some importance when the threshold region will be actually explored, with the off-peak data (see §7.2).
In fig. 7.1(a) the total cross section for different contributions, as obtained from EVA, is shown, normalized to the cross section for ISR only. The large angle cuts are applied ($50^o < \theta_{\pi,\gamma} < 130^o$). The lower plot is a zoom at the threshold ($M^2_{\pi\pi} < 0.35$ GeV^2). In

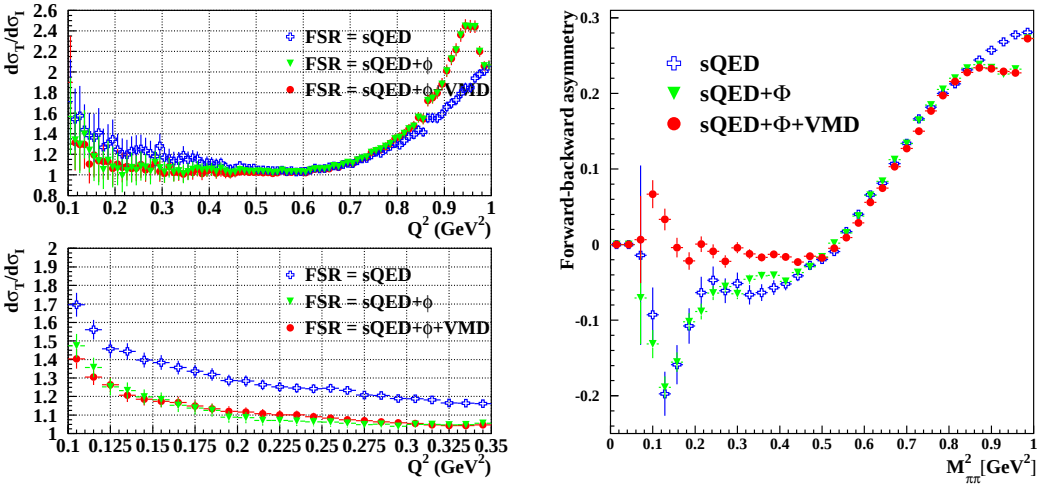

(a) (b)

Figure 7.1: (a) Ratio between the total cross section and the ISR cross section as a function of $M^2_{\pi\pi}$ for different models of FSR. (b) Forward-backward asymmetry evaluated for the same models of FSR as in (a).

fig. 7.1(b) the forward-backward asymmetry is plotted for the same three cases, i.e.
ISR+FSR, called sQED in the plot (blue crosses)
ISR+FSR+scalar mesons, called sQED+Φ in the plot (green triangles)
ISR+FSR+scalar mesons+direct $\rho\pi$, called sQED+Φ+RPT in the plot (red full points)
Within the used kaon-loop model, the peak in the cross section at about 1 GeV^2 corresponds to intermediate scalar meson states. The latter is responsible also for the bump at high masses of the forward-backward asymmetry, without indeed explaining the rise that we observe in the data below the ρ-peak. This rise can be attribute to the presence of $\rho\pi$, which seems to have a big effect on the forward-backward asymmetry (in the direction of the data), without giving indeed a big contribution to the cross section. We underline that these results are obtained with the scalar mesons parameters obtained from the analysis of the neutral channel $e^+e^- \to \pi^0\pi^0\gamma$. A tuning of the parameters is in progress and the results shown presently could change in the future. The clarification in the scalar mesons sector will allow us also to

1. improve the systematic error on the *irreducible* background, that at present is the dominant one of the present analysis;

2. look at the region below the ρ-peak, where we have limited the analysis presented in this thesis.

It is important to underline that from an experimental point of view (selection of the sample, study of the efficiencies, evaluation of the systematic errors) the present work covers a region

wider than 0.5-0.85 GeV^2, which is the range in which we have evaluated the pion form factor. Only the scalar mesons subtraction remains an open point.

7.2 Off-peak data

The hadronic cross section measurement does not require the machine to run at $\sqrt{s} = m_\phi$. As pointed out in the previous chapters, at large angles the major background contribution comes from $\phi \to \pi^+\pi^-\pi^0$ and the biggest uncertainty on the measurement from the radiative decay $\phi \to (f_0(980) + f_0(600)) + \gamma$.
Since the background from $\pi^+\pi^-\pi^0$ proceeds via the ϕ resonance and the width of the ϕ resonance is small (4.26 MeV), the cross section $\phi \to \pi^+\pi^-\pi^0$ drops rapidly if one lowers the center-of-mass energy of the collider away from m_ϕ. Fig. 7.2 shows a preliminary measurement of the $\phi \to \rho\pi \to \pi^+\pi^-\pi^0$ cross section made by KLOE. As can be seen from

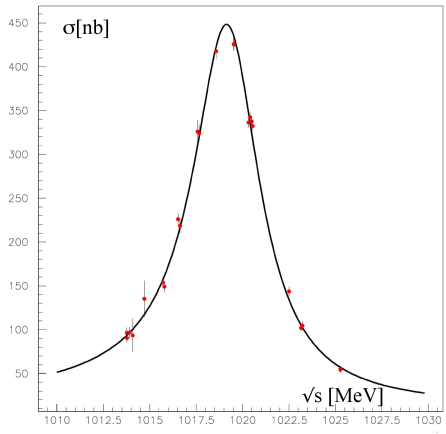

Figure 7.2: Preliminary measurement of the cross section $e^+e^- \to \phi \to \rho\pi$. The data points were obtained with the KLOE detector from an energy scan around m_ϕ performed in 2001.

the plot, the cross section for this process drops by ca. 90% when reducing the center-of-mass energy of DAϕNE by 10 MeV, while a reduction by 20 MeV to a collision energy of 1 GeV leaves us with only 5% of the $\pi^+\pi^-\pi^0$ background.
A measurement of the $\pi^+\pi^-\gamma$ cross section with data taken at 1.0 GeV, allows to check the treatment of the $\pi^+\pi^-\pi^0$ background in the large angles analysis performed with on-peak data. A measurement at 1 GeV is desirable if one considers that the $\pi^+\pi^-\pi^0$ cross section is one order of magnitude bigger than the cross section of $\pi^+\pi^-\gamma$ in the large angle region (fig. 3.7(b)).
The poor knowledge of the contribution of the scalar mesons translates in an uncertainty of the $\pi^+\pi^-\gamma$ measurement in the large angle region. The uncertainty becomes unacceptable if one wants to explore the threshold region, down to $2m_\pi$ mass.
Aso an energy scan around the ϕ mass turns out to be very useful for the study of the scalar mesons. On December 2005 a luminosity of $\sim$10 pb^{-1} has been collected in four different

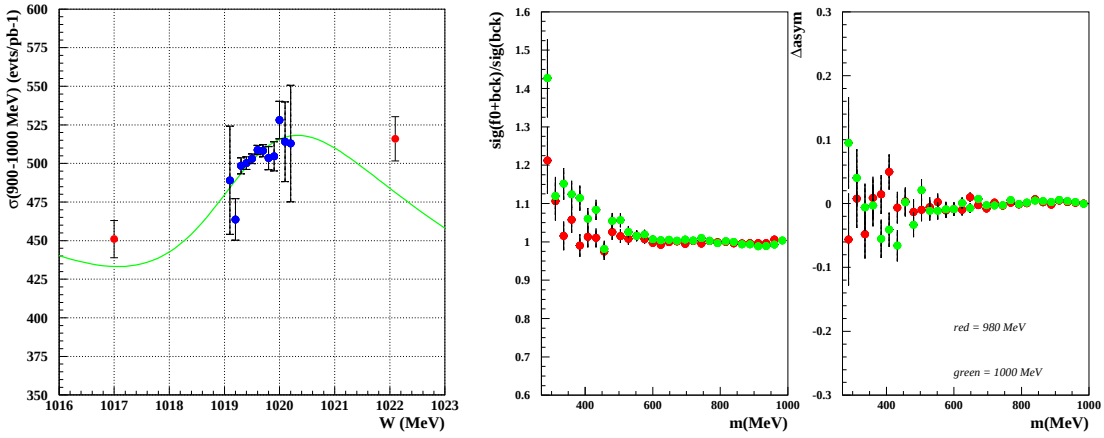

(a) (b)

Figure 7.3: (a) Center of mass energy dependence of the cross section for events in the range 900÷1000 MeV. The blue points are the on-peak data, the red points are the two off-peak samples. The curve is the prediction based on the kaon loop amplitude. (b) Effect of the scalar amplitude on the event spectrum (left plot) and on the charge asymmetry (right plot) as a function of the invariant mass $\pi\pi$ at 1000 MeV (green points) and at 980 MeV (red points).

points. The kaon loop (§6) amplitude contains explicitly the dependence on the center-of-mass energy $\sqrt{s}$. It is possible to evaluate the scalar contribution off-peak by extrapolating the amplitude found by fitting the on-peak data. In the extrapolation the three parameters are held fixed and the interference sign is taken as negative, as turned out in the fit of the KLOE data described in [77]. Fig. 7.3(a) shows the comparison between the off-peak data from 2002 scan and the extrapolated curve.

At 1.0 GeV the effect of scalar mesons is still visible, both in the mass spectrum and in the charge asymmetry. By running the event generator EVA where the scalar amplitude is added to ISR and FSR amplitudes, we get the prediction (shown in fig. 7.3(b)) for the scalar amplitude at the center of mass energy of DAΦNE of 1000 MeV and 980 MeV. As can be seen, a residual scalar contribution is still present, but strongly reduced with respect to the data collected at m_ϕ.

Between December 2005 and March 2006, DAΦNE has run at $\sqrt{s} = 1000$ MeV and KLOE has collected $\sim$225 pb^{-1}. These data are under study at present. Some preliminary checks have been already done. The two main advantages of having data at 1000 MeV are already visible in fig. 7.4. The trackmass distribution for 2002 (on peak) and for 2006 data (off peak) is shown. The plot refers to an identical selection at large photon polar angle. The disappearing of the second peak in 2006 data demonstrates the big reduction of $\pi^+\pi^-\pi^0$ events.

The comparison of the forward-backward asymmetry has been already shown in §6.4 (fig. 6.13(a)). In the 2002 sample the presence of the scalar mesons is responsible for the rise of the curve towards low values of $M^2_{\pi\pi}$. The 2006 sample, almost free from the scalar

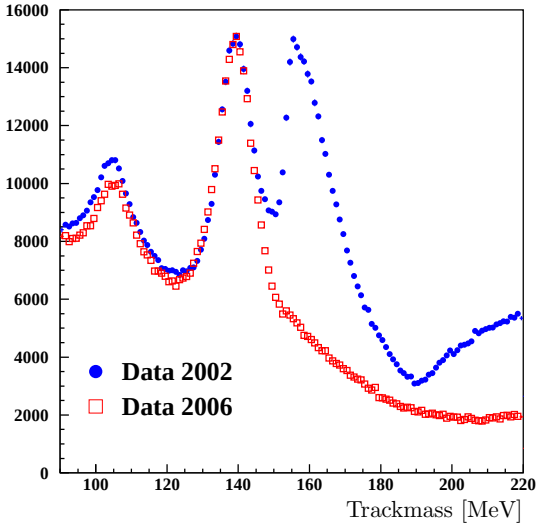

Figure 7.4: (a) Trackmass distribution for 2002 data on-peak (blue full points) and for 2006 data off-peak (empty red squares). It is evident the reduced contamination from $\pi^+\pi^-\pi^0$ events in the off-peak sample.

mesons contribution, follows the behavior of the $\pi^+\pi^-\gamma$ ISR+FSR prediction (fig. 6.13(b)). The use of a sample free from the scalar mesons at large angles will allow us to fix some parameters in the low mass region, testing for example possible extensions of sQED, that, according to [79], can play a role at low $M^2_{\pi\pi}$. Once having measured the $\pi^+\pi^-\gamma$ cross section down to the threshold with the off-peak data (without the issues of the *irreducible* background of scalar mesons and the resonant decay to $\rho^\pm\pi^\mp$) one will be able to use again the 2002 data to investigate the properties of scalar mesons.

7.3 Measuring the ratio R(s) in the *small angle* analysis

An alternative approach to our standard analysis is to normalize the $\pi^+\pi^-\gamma$ cross section with $\mu^+\mu^-\gamma$ events, i.e. measuring directly the ratio R(s) to be put into the dispersion integral (eq. 1.20).

The advantage of this approach is that in the ratio the normalization to the luminosity, the division by the radiator function as well as the correction for the vacuum polarization disappear. If one excludes the contribution of these effects to the total theoretical error in the small angle analysis, one passes from a theoretical error of 0.9% to one of 0.3%. The collected statistics is sufficient to perform this measurement but a complete understanding of the efficiency for the $\mu^+\mu^-\gamma$ events is necessary. In fact in the present analysis the muon pairs are a background and suppressed by the cut on trackmass and the obtained precision for the $\mu^+\mu^-\gamma$ identification is lower than what is needed for a measurement of the ratio R(s).

An analysis in which the R-ratio is measured, using ISR-photons at small polar angles and using 2002 data, is presently in progress. The trackmass is used to separate pions and

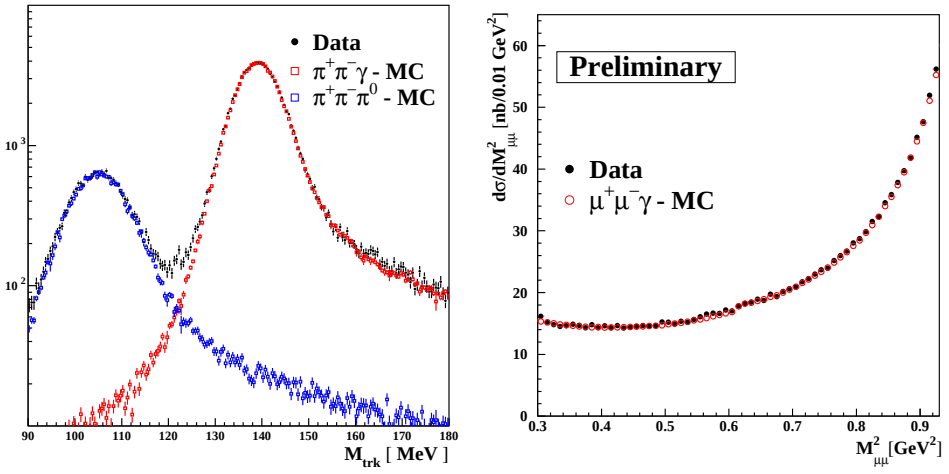

(a) (b)

Figure 7.5: (a) Trackmass distribution for $0.8 < M^2_{\pi\pi} < 0.82$ GeV^2. In full black points data are shown, in open red and blue ones are for MonteCarlo simulations, respectively $\pi^+\pi^-\gamma$ and $\mu^+\mu^-\gamma$ events. The events falling into the region between the two black lines do not enter in the analysis, since here the tails of the $\pi^+\pi^-\gamma$ and of $\mu^+\mu^-\gamma$ distribution overlap each other. (b) Comparison between data and MonteCarlo of the cross section $\mu^+\mu^-\gamma$.

muons: in fig. 7.5(a) the trackmass distribution for $0.8 < M^2_{\pi\pi} < 0.82$ GeV^2 is shown. The black data points are data, the red and the blue ones refer to two MonteCarlo simulations, for $\pi^+\pi^-\gamma$ and $\mu^+\mu^-\gamma$ respectively. The trackmass region between 115 and 130 MeV is excluded, because here the tails of the two classes of events overlap each other and it becomes difficult to distinguish them with high accuracy. The muon data sample will be useful also to check the radiator function. The strategy in this case is to select a clean data sample of muons and compare the cross section $\mu^+\mu^-\gamma$ with the one obtained from the simulation. The PHOKHARA generator uses the same ISR corrections for pions and muons. Since the radiator function regards only the initial state of the process, making a comparison between data and MonteCarlo of the $\mu^+\mu^-\gamma$ cross section means to test the simulation of the radiator function which is used to extract the pion form factor. A preliminary comparison between data and MonteCarlo of the muon cross section is shown is fig. 7.5(b). An agreement better than 1% is obtained.

Finally we mention that a new version of the BABAYAGA generator for $e^+e^- \to e^+e^-$ events is now available [75] . An error of 0.5% was claimed for the previous version, which was used in the measurement of the integrated luninosity. For this new version the uncertainty could be reduced to 0.1%. Since in the measurement of the integrated luminosity the systematic error coming from theory is larger than the experimental one (see §6.1), we expcet to overall improve the precision on this measurement.

Conclusion

KLOE has successfully used the *radiative return* method to measure the hadronic cross section $\sigma(e^+e^- \rightarrow \pi^+\pi^-)$ in an analysis of $\sim$140 pb^{-1} of data collected in 2001. Looking at small photon polar angle (*small angle analysis*), in order to reduce the background contamination, the KLOE measurement is limited to the energy squared range $0.35<M^2_{\pi\pi}<0.95$ GeV^2, being the threshold kinematically forbidden in this acceptance configuration. The obtained result confirms the observed discrepancy between e^+e^-- and τ-spectral function.

The same method has been applied to a second analysis, where 240 pb^{-1} of data collected in 2002 have been analysed, looking at the complementary acceptance region (*large angle analysis*). The three main sources of backgrounds (Bhabha, $\mu^+\mu^-\gamma$ and $\pi^+\pi^-\pi^0$ events) are rejected by means of kinematical variables and the residual contamination is subtracted according to the MonteCarlo prediction. A comparisons data-MonteCarlo on several variables assure that the background subtraction is solid: in the range $0.5\div0.85$ GeV^2 the associated systematic error is $<0.3\%$.

The efficiencies due to the analysis cuts have been measured from data control sample in most cases, otherwise they are taken from MonteCarlo. The systematic errors for each efficiency have been evaluated as well. Neglecting the error of the subtraction of the *irreducible* background, the total systematic error on the ρ-peak is estimated to be 0.6%, considerably smaller than in the *small angle analysis*.

The *irreducible* background consists of three sources: the Final State Radiaton-Leading Order events, whose contribution is taken into account by PHOKHARA using the sQED model, the resonant decay $\phi \rightarrow \rho^\pm\pi^\mp \rightarrow \pi^+\pi^-\gamma$ whose cross section is poorly known, but which is negligible above 0.5 GeV^2, and finally the scalar meson contribution from the ϕ radiative decay into $f_0(980)$ and $f_0(600)$. The dominant error of the pion form factor measurement at present comes from the scalar mesons contribution. The nature of these particles is still quite controversial and several models describing their dynamics are available. The forward-backward and the charge asymmetry, given their sensitivity to the presence of the scalar mesons, have been widely used to study these particles. Comparing the data with the MonteCarlo prediction using different models for the scalar mesons, we have been able to choose one model that fits better our data. By further comparisons between the chosen model and the data, we have tuned the parameters of the $f_0(980)$ entering the model. This procedure has not to be meant only as a method to subtract as much precisely as possible the scalar mesons contribution from the data sample; it is actually a method to extract information on these particles. A new MonteCarlo generator (EVA) taking into account both the scalar meson contribution and the direct decay $\phi \rightarrow \rho^\pm\pi^\mp$ has been recently released. The parameters of the scalar mesons have not been tuned yet in EVA.

At the moment we use the comparison between the PHOKHARA and EVA predictions to have a preliminary estimate of the systematic error on the scalar mesons correction. This systematic error is the dominant one in the pion form factor that we have extracted between 0.5 and 0.85 GeV^2.

The pion form factor measured with the *large angle analysis* has been compared with the published one (*small angle analysis*), and considering the systematic errors of the two, we conclude that they are compatible.

In the near future, the systematic error on the scalar mesons will be reduced by repeating the tuning procedure on the new EVA generator. We are confident that this method will allow a much improved determination of the background from scalar mesons.

The ultimate precision on the measurement of the pion form factor will come from the analysis of the data that has been collected in 2006, in which a sample of $\sim$225 pb^{-1} has been taken at $\sqrt{s}$=1000 MeV, i.e. 20 MeV lower than the ϕ mass. The contamination from $\pi^+\pi^-\pi^0$ events is drastically reduced, allowing to cross check the treatment of this background in the *large angle analysis*. Moreover the scalar mesons contribution is strongly suppressed in the off-peak data, reducing this important background almost to zero. Like this it will be possible to perform for the first time tests on the validity of the scalar QED model for the description of the FSR amplitude. For this test the forward-bacward and the charge asymmetry will be used. This test is under study at the moment and has been used already in the present analysis for the estimate of the systematic error of the final state radiation subtraction.

Bibliography

[1] I. B. Vasserman *et al.*, Sov.J.Nucl.Phys. **30**, 519 (1979).

[2] I. B. Vasserman *et al.*, Sov.J.Nucl.Phys. **33**, 709 (1981).

[3] S. Dolinsky *et al.*, Phys.Reports **202**, 99 (1991).

[4] L. M. Barkov *et al.*, Nucl.Phys. **B256**, 365 (1985).

[5] R. R. Akhmetshin *et al.*, Phys. Lett. **B527**, 161 (2002).

[6] R. R. Akhmetshin *et al.*, Phys. Lett. **B578**, 285 (2004).

[7] M. N. Achasov *et al.*, J.Exp.Theor.Phys. **101**, 1053 (2005).

[8] M. N. Achasov *et al.*, J.Exp.Theor.Phys. **103** (2006).

[9] A. Quenzer *et al.*, Phys.Lett. **B76**, 512 (1978).

[10] D. Bisello *et al.*, Phys.Lett. **B220**, 321 (1989).

[11] A. Aloisio *et al.*, Phys.Lett. **B606**, 12 (2005).

[12] H. Burkhardt and B. Pietrzyk, Phys. Rev **D72**, 057501 (2005).

[13] R. R. Akhmetshin *et al.*, Phys.Lett. **B642**, 203 (2006).

[14] R. R. Akhmetshin *et al.*, Phys.Lett. **B595**, 101 (2004).

[15] B. Aubert *et al.*, Phys.Rev. **D70**, 072004 (2004).

[16] B. Aubert *et al.*, Phys.Rev. **D71**, 052001 (2004).

[17] B. Aubert *et al.*, Phys.Rev. **D73**, 052003 (2006).

[18] R. Alemany, M. Davier, and A. Höcker, Eur.Phys.J **C2**, 123 (1998).

[19] V. Cirigliano, G. Ecker, and H. Neufeld, JHEP **0208**, 002 (2002).

[20] S. Ghozzi and F. Jegerlehner, Phys.Lett **B583**, 222 (2004).

[21] W. H. Louisell, R. W. Pidd, and H. R. Crane, Phys.Rev. **91**, 475 (1953).

[22] J. S. Schwinger, Phys.Rev. **73**, 1948 (1973).

[23] G. Gabrielse, D. Henneke, T. Kinoshita, M. Nio, and B. Odom, Phys.Rev.Lett. **97**, 030802 (2006).

[24] G. W. Bennet *et al.*, Phys. Rev. Lett. **92**, 161802 (2004).

[25] C. M. Sommerfield, Phys.Rev. **107**, 328 (1957).

[26] C. M. Sommerfield, Ann.Phys. (N.Y.) **5**, 26 (1958).

[27] A. Petermann, Helv. Phys. Acta **30**, 407 (1957).

[28] A. Petermann, Nucl. Phys. **5**, 677 (1958).

[29] H. H. Elend, Phys. Lett. **20**, 1966 (1966).

[30] S. Laporta and E. Remiddi, Phys. Lett.B **356**, 390 (1995).

[31] S. Laporta and E. Remiddi, Phys. Lett.B **379**, 283 (1996).

[32] S. Laporta, Nuovo Cimento A **106**, 675 (1993).

[33] S. Laporta and E. Remiddi, Phys. Lett.B **301**, 440 (1993).

[34] M. Passera, Nucl.Phys.Proc.Suppl. **162**, 242 (2006).

[35] A. Czarnecki, B. Krause, and W. Marciano, Phys. Rev. D **52**, 2619 (1995).

[36] A. Czarnecki, B. Krause, and W. Marciano, Phys. Rev. Lett. **76**, 3267 (1996).

[37] S. J. Brodsky and E. De Rafael, Phys. Rev. **168**, 1620 (1968).

[38] B. E. Lautrup and E. De Rafael, Phys. Rev. **174**, 1835 (1968).

[39] S. Eidelman, 'Status of $(g_\mu - 2)/2$ in Standard Model' talk given at the 'ICHEP 2006, XXXIII International Conference on High Energy Physics', Moscow (Russia) 2006.

[40] K. Hagiwara, A. D. Martin, D. Nomura, and R. Teubner, Phys. Rev. **D69**, 093003 (2004).

[41] K. Melnikov and A. Vainshtein, Phys.Rev. **D70**, 113006 (2004).

[42] A. Höcker, hep-ph/0410081 .

[43] M. Davier, hep-ph/0701163 .

[44] K. Hagiwara, A. D. Martin, D. Nomura, and R. Teubner, hep-ph/0611102 (2006).

[45] V. Ezhela, S. Lugovsky, and O. Zenin, hep-ph/0312114 .

[46] F. Jegerlehner, Nucl. Phys. **B164**, 325 (2004).

[47] F. Jegerlehner, Nucl. Phys. Proc. Suppl. **B131**, 213 (2004).

[48] M. Davier, S. Eidelman, A. Höcker, and Z. Zhang, Eur. Phys. J **C31**, 503 (2003).

[49] J. F. de Troconiz and F. J. Yndurain, Phys. Rev. **D71**, 073008 (2005).

[50] F. Jegerlehner, Nucl. Phys. Proc. Suppl. **162**, 22 (2006).

[51] I. Logaschenko, 'Hadronic cross section at CMD-2 and SND' talk given at the 'International workshop 'e^+e^- collision from ϕ to ψ', Novosibirsk, 2006.

[52] R. R. Akhmetshin *et al.*, hep-ex/0610021 .

[53] K. Abe *et al.*, hep-ex/0512071 .

[54] M. Steinhauser, Phys.Lett **B429**, 158 (1998).

[55] J. H. Kühn and M. Steinhauser, Phys.Lett **B437**, 425 (1998).

[56] M. Davier and A. Höcker, Phys.Lett **B435**, 427 (1998).

[57] J. F. de Troconiz and F. J. Yndurain, Phys.Rev. **D65**, 093002 (2002).

[58] F. Jegerlehner, hep-ph/0308117 .

[59] S. Eidelman and F. Jegerlehner, Z.Phys. **C67**, 585 (1995).

[60] G. J. Gounaris and J. J. Sakurai, Phys.Rev.Lett. **21**, 244 (1968).

[61] J. H. Kühn and A. Santamaria, Z. Phys. **C48**, 445 (1990).

[62] G. Rodrigo and J. Kühn, Eur.Phys.J. **C 25**, 215 (2002).

[63] H. Czyż, A. Grzenlińska, J. Kühn, and G. Rodrigo, Eur.Phys.J. **C 33**, 333 (2004).

[64] H. Czyż, A. Grzenlińska, and J. Kühn, Phys. Lett. **B611**, 116 (2005).

[65] M. Adinolfi *et al.*, Nucl. Instrum. Meth. A **488**, 51 (2002).

[66] M. Adinolfi *et al.*, Nucl. Instrum. Meth. A **482**, 364 (2002).

[67] KLOE Collaboration, LNF96/043 (IR) (1995).

[68] F. Ambrosino *et al.*, Nucl. Instrum. Meth. A **534**, 403 (2004).

[69] M. Incagli, KLOE Memo **147** (2001).

[70] S. Binner, J. Kühn, and K. Melnikov, Phys.Lett. **B459**, 279 (1999).

[71] G. Rodrigo, A. Gehrmann-De Rideer, M. Guilleaume, and J. Kühn, Eur.Phys.J. **C 24**, 71 (2002).

[72] B. Valeriani, KLOE Memo **nr. 295** (2004).

[73] B. Valeriani-Kaminski, *Messung des Pion-Formfaktors mittels Radiadive Return an dem KLOE Experiment*, PhD thesis, Universität Karlsruhe, 2005.

[74] A. Denig *et al.*, KLOE note 192, 2004
URL http://www.lnf.infn.it/kloe/pub/knote/kn192.ps.

[75] G. Balossini, C. M. Carloni Calame, G. Montagna, O. Nicrosini, and F. Piccinini, hep-ph/0607181 .

[76] A. Aloisio *et al.*, Phys. Lett. **B537**, 21 (2002).

[77] F. Ambrosino *et al.*, Phys. Lett. **B634**, 148 (2006).

[78] N. N. Achasov and V. I. Ivanchenko, Nucl.Phys. **B315**, 465 (1989).

[79] G. Pancheri, O. Shekhovtsova, and G. Venanzoni, 2006.

[80] Frodesen, Skjeggestad, and Tøfte, *Probability and statistics in particle physic* (Universitetsforlaget, 1979).

[81] M. Moulson and S. Müller, KLOE Meno n.228 .

[82] C. Gatti, M. Palutan, and T. Spadaro, KLOE note n.209 .

[83] C. M. Carloni Calame, C. Lunardini, G. Montagna, O. Nicrosini, and F. Piccinini, Nucl.Phys **B 584**, 459 (2000).

[84] F. A. Berends and F. Kleiss, Nucl.Phys **B 228**, 537 (1983).

[85] E. Drago and G. Venanzoni, INFN-AE-97-48 (1997).

[86] F. Ambrosino *et al.*, Eur.Phys. **C47**, 589 (2006).

[87] A. Bramon, G. Colangelo, P. Franzini, and M. Greco, Phys.Lett. **B287**, 263 (1992).

[88] J. Lucio Martinez and M. Napsuciale, Phys.Lett. **B331**, 418 (1994).

[89] V. Aulchenko *et al.*, Phys.Lett. **B440**, 442 (1998).

[90] F. Ambrosino *et al.*, Eur.Phys.J **C49**, 473 (2006).

[91] $\Delta\alpha_{had}(s)$ points have been provided by Fred Jegerlehner
URL http://www-zeuthen.desy.de/fjeger/alphaQEDn.uu.

[92] Schwinger, J.S., *Particles, Sources and Fields* (Addison-Wesley, Redwood City, USA, 1989).

Acknowledgements

I would like to thank:

- Dr. Achim Denig for making my work possible and for advising me constantly with productive suggestions;
- Prof. Dr. Wolgang Kluge for his guidance and for the encouragement during the progress of my work;
- Prof. Dr. Thomas Müller for taking the duty of being my co-referent;
- Dr. Stefan Müller for answering always to my infinite questions;
- Dott. Paolo Beltrame for the nice collaboration;
- the further members the $\pi\pi\gamma$ group for the collaborative attitude;
- Dr. Hans-Jürgen Simonis for having always solved my computer problems.